

Technical University of Munich
School of Natural Sciences
Department of Physics



Master's Thesis

The Pacific Ocean Neutrino Experiment: Advancements in the Optical Module Development for the First Detector Line of P-ONE

Niklas Retza

September 2023

First Examiner (Supervisor): Elisa Resconi
Second Examiner: Béla Majorovits

Advisor: Christian Spannfellner

Abstract

The Pacific Ocean Neutrino Experiment (P-ONE) is a proposed multi-cubic-kilometer neutrino observatory off the coast of Vancouver Island, Canada. At a depth of 2660 meters in the Cascadia Basin, P-ONE will be connected to the NEPTUNE observatory, a deep-sea infrastructure in the Northeast Pacific Ocean hosted by Ocean Networks Canada (ONC). A first detector line, called P-ONE-1, is planned to be deployed in 2024/2025. P-ONE-1, consisting of 20 optical and calibration instruments distributed over a total vertical length of around one kilometer, shall serve as a prototype line for the detector, and ultimately be the blueprint for the following detector lines.

In this thesis, the current development status of P-ONE-1s' Optical Module (P-OM) is presented, which will detect Cherenkov light stemming from secondary particles of neutrino interactions in water. The P-OM consists of two glass hemispheres, connected via a titanium cylinder to the detector line. Each hemisphere contains eight photomultiplier tubes (PMTs), optically coupled to the glass via transparent gel reflector pads. The multi-PMT design allows to cope with the high background rates in the depths of the Northeast Pacific Ocean, while the modular and minimal mechanical design of the P-OM makes it easily scalable in vision of the construction of the entire P-ONE detector.

The main contributions of this work are three-fold: First, a test setup for the PMTs used in P-ONE-1 has been developed to allow for a plug-and-play characterization of their properties. Second, a Monte Carlo framework for optical simulations of the P-OM has been developed, utilizing a novel approach for its geometry implementation, enabling more precise results compared to previous implementations. Last, a cleanroom production facility for the P-OM has been set up.

Acknowledgements

This thesis would not have been possible without the amazing work done by the people at the ECP group at TUM and in the P-ONE collaboration.

I want to express my gratitude to Prof. Elisa Resconi for allowing me to conduct my work at the frontier of neutrino astronomy. During my year at ECP, I experienced what I can only consider a prime example of good scientific leadership. Her support for young scientists and the trust she put in them has been a great source of inspiration for me, and it will be for many generations of students to come.

I want to thank everyone on the development team of the P-OM, with whom I have shared countless hours of discussions in and out of our (almost) weekly meetings. Without the collaborative effort of Christian Spannfellner, Vincent Gousy-Leblanc, Chiara Bellenghi, Michael Böhmer, Laszlo Papp, Martin Dinkel, Lea Ginzkey, Ben Nührenbörger and Alexandra Scholz, the development of the P-OM wouldn't be where it is today. I also would like to acknowledge the previous work on the gel pad production by Christopher Fink and on the OMCU by Laura Winter.

For offering me the unique opportunity to travel to the P-ONE collaboration meeting in Vancouver, I want to thank Prof. Matthias Danninger. In extension, I want to thank Prof. Elisa Resconi for enabling my participation in the P-ONE meeting in Krakow and the DPG spring meeting in Dresden.

For providing insightful figures to this thesis, my appreciation goes to Felix Henningsen, Lisa Schumacher, Christian Spannfellner, Lasse Halve, Lea Ginzkey and Ben Nührenbörger. In addition, I would like to thank Vincent Gousy-Leblanc for the implementation of the fitting algorithm used in figures 5.6 and A.3.

For helpful comments on drafts of this thesis to improve both language and content, I want to express my gratitude to Christian Spannfellner and Vincent Gousy-Leblanc.

Finally, I would like to thank my girlfriend for her unwavering love and support throughout the year-long journey of writing this thesis. Her continuous encouragement, necessary patience and endless supply of excellent coffee helped me tremendously through the more stressful episodes of the last twelve months.

Contents

Abstract	iii
Acknowledgements	v
1 Introduction	1
2 High Energetic Cosmic Messengers	3
2.1 Cosmic Rays	3
2.2 Gamma Rays	5
2.3 Gravitational Waves	6
2.4 Neutrinos	7
2.5 Multi-Messenger Observations	12
3 Large Scale Neutrino Telescopes	15
3.1 Detection Principle	15
3.2 IceCube	22
3.3 KM3NeT	24
3.4 Baikal-GVD	25
3.5 P-ONE	26
4 The First Line for the P-ONE Detector	29
4.1 P-ONE-1 String Design	29
4.2 The Optical Module (P-OM)	30
4.3 The Calibration Module (P-CAL)	32
5 The P-ONE Optical Module Calibration Unit	33
5.1 Photomultiplier Tubes	33
5.2 The μ Base	36
5.3 The OMCU Setup	42
5.4 Control Software	44
5.5 Verification of Hamamatsu Calibration Data	49
5.6 Upgrade Plans for the OMCU	57

6 A Geant4 Framework for the P-ONE Optical Module	61
6.1 The Geant4 Toolkit	62
6.2 Implementation of the P-OM Geometry	63
6.3 Simulation Parameters	68
6.4 Angular Acceptance Simulations for the P-OM	71
6.5 Muon Beam Simulations for the P-OM	84
6.6 Single PMT Angular Acceptance	86
6.7 Performance of the Framework	88
7 Integration of P-ONE's First Optical Modules	91
7.1 Gelpad Production and Optical Coupling	91
7.2 The Optical Tent	92
7.3 Assembly, Testing and Quality Control for the P-OM	94
8 Conclusion	97
A Additional Plots	99
A.1 μ Base Performance Plots	99
A.2 Geant4 Muon Simulations	102
B Source Code	105
Bibliography	107

Chapter 1

Introduction

With the advent of Multi-Messenger Astronomy in the early 21st century comes the desire to precisely study the cosmic neutrino flux, identify its sources, and thereby reveal hidden secrets of the most violent cosmic accelerators. To pursue this task, a multitude of neutrino telescopes have been built all around the world, from IceCube [1] at the South Pole and KM3NeT [2] in the Mediterranean Sea to Baikal-GVD in Siberia [3]. These telescopes help to probe the cosmic neutrino flux arriving on Earth, with IceCube – the longest running experiment – being able to recently identify TXS0506+056 [4] and NGC 1068 [5] as well as our own galactic plane [6] as neutrino sources.

A new neutrino telescope, the Pacific Ocean Neutrino Experiment (P-ONE) [7] will be located off the coast of Vancouver Island, in the Cascadia Basin in a depth of 2660 m, and is currently in development. P-ONE will be part of a new generation of neutrino telescopes, that together will significantly increase the detection potential of neutrino sources and thereby lead to a clearer picture of the neutrino sky [8]. While the final P-ONE detector will not be deployed before the end of this decade, the first detector line, P-ONE-1, is currently in development, with deployment targeted for 2024/2025. The line will consist of 20 Optical Modules (P-OMs), spaced evenly in the water over a height of one kilometer, detecting Cherenkov light from neutrino interaction remnants.

In this thesis, the current status of the development process of the P-OM is presented. The main contributions of this thesis are three-fold: First, a plug-and-play test setup for the P-OMs photomultiplier tubes (PMTs), called the Optical Module Calibration Unit (OMCU), has been developed, and a subset of P-OM PMTs has been subsequently characterized in this setup. Secondly, a Monte Carlo optical simulation framework for the P-OM has been designed, using a novel approach of directly importing CAD geometries, leading to highly precise results. This framework has helped to better understand the optical mechanics of the P-OM, giving valuable feedback for the development process. Lastly, the groundwork for the assembly of

the first P-OMs has been set, with the acquisition of the *Optical Tent* as a clean production environment. The outline of this thesis is thereby as follows:

Chapter 2 gives an introduction on the different kinds of cosmic messengers, their origins, respective detectors, and recent scientific discoveries. This chapter highlights the multi-messenger connection in cosmic accelerators. It helps to understand how the study of neutrino fluxes combined with observations of other messengers gives insight into the inner workings of such cosmic objects.

Chapter 3 introduces the working principle of large-scale neutrino telescopes in detail, starting with the initial neutrino interaction and ending with the detection of remnant Cherenkov light. In addition, causes for background in the detector, as well as its angular resolution, are discussed. This is followed by a technical introduction on current and future neutrino telescopes.

Chapter 4 gives an overview on the technical specifications of P-ONE's first detector line, P-ONE-1. The design of the line is presented, with a special focus on the Optical Module (P-OM) and the Calibration Module (P-CAL).

Chapter 5 presents the OMCU, the test setup for Optical Module PMTs. Insight is given on the PMT and the μ Base as the OMCUs key components, followed by an overview of the OMCUs hardware and software design. This is followed by an evaluation of PMTs to be used in the P-OM, where measured characteristics were compared to calibration data provided by the PMT's manufacturer. Lastly, a quick outlook towards future upgrades of the OMCU is given.

Chapter 6 first describes the P-OM optical simulation framework, highlighting the hybrid approach of importing most of the P-OM geometry from CAD drawings while modeling optically relevant parts through source code. Then, the results of simulations on the angular acceptance of the P-OM are presented, studying the effect of different design choices on the performance of the P-OM. After that, initial simulations with muon beams are presented. Lastly, simulation results on a single PMT are compared to measurements in the OMCU, showing good agreement between measurement and simulation.

To conclude, **Chapter 7** depicts the current status of the P-OMs integration process. Procedures for the optical coupling and integration of PMTs to the P-OM glass sphere are presented, and the *Optical Tent* as an assembly facility is introduced. Finally, a plan for integration, testing, and quality control of the P-OM is outlined.

Chapter 2

High Energetic Cosmic Messengers

For centuries, the study of astronomical objects was limited to the information these objects emitted in the visible spectrum of light. However, the 20th century marked a pivotal moment for astronomy with the emergence of radio and space-based telescopes. These advancements allowed astronomers to extend their observations beyond visible light into the range of radio waves, infrared, ultraviolet, and X-rays, unveiling previously hidden aspects of the universe. This expanded view illuminated objects such as pulsars [9], black holes [10], and active galactic nuclei [11].

In the early 21st century, another paradigm shift occurred with the emergence of gravitational wave detectors, neutrino telescopes, and cosmic ray detectors. These advancements allowed for observations using a wide range of cosmic messengers, enabling the scientific discipline of multi-messenger astronomy [12, 13].

The following chapter gives an introduction to cosmic messengers in the high-energy regime. This is followed by touching on how connecting observations from different messengers can lead to new scientific discoveries, especially regarding the origins of those messengers.

2.1 Cosmic Rays

Cosmic rays are high-energetic charged particles hitting the Earth's atmosphere from outer space. They were first discovered in 1912 by V. Hess, who observed an increased rate of radiation during balloon rides at high altitudes [14], hinting at the extraterrestrial origin of this radiation. He was subsequently awarded the 1936 Nobel Prize in Physics for his discovery.

In more modern times, cosmic ray detectors cover energy ranges from around one GeV up to above 100 EeV [13, 15]. Due to the decreased flux at high energies, detectors aiming to probe the high end of the cosmic ray energy regime must possess

a larger volume than detectors for lower energies. The largest cosmic ray detector, the Pierre-Auger-Observatory [16, 17] encompasses, among other instruments, 1600 water Cherenkov detectors spread around 3000 km² in the Mendoza province of Argentina. While observatories placed in space, such as the ISS-based Alpha Magnetic Spectrometer (AMS) [18], can detect cosmic rays directly, ground-based observatories detect remnants of atmospheric showers and consequently can only deduce information about the primary particle through model assumptions.

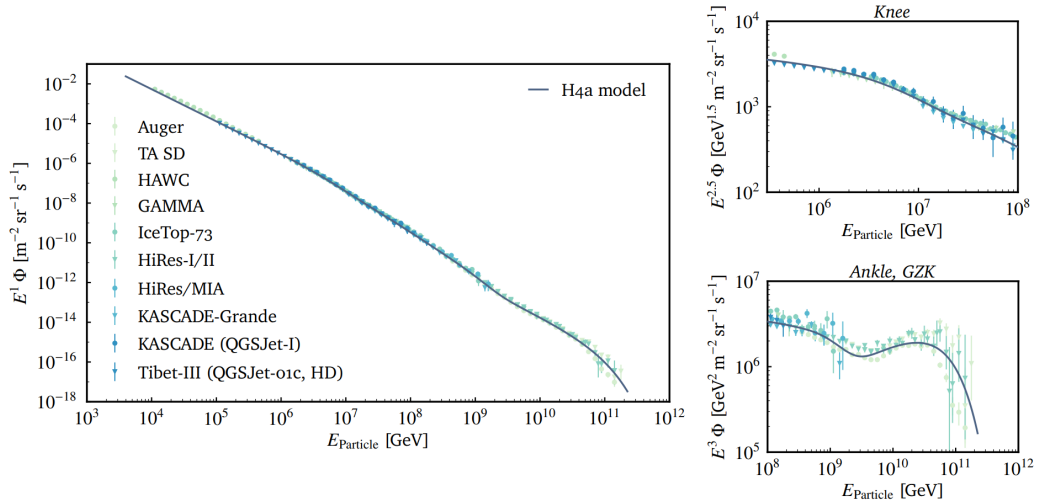


Figure 2.1: All particle energy spectrum for high energetic cosmic rays. Data combined from several measurements. To the right, the knee (top) and ankle (bottom) are enhanced through multiplication with $E^{2.5}$ and E^3 , respectively. Figure provided by F. Henningsen. Data courtesy of the authors of [15].

Figure 2.1 combines the measured flux of cosmic rays from various experiments. Remarkably, over a wide energy range, the flux can be described by an inverse power law with the spectral index γ :

$$\frac{d\Phi}{dE} \propto E^\gamma \quad (2.1)$$

This is incompatible with black body radiation and therefore leads to the conclusion that those particles' energies are not of thermal origin but stem from cosmic accelerators [15, 19]. Up to around 1 PeV, the spectral index is $\gamma \approx -2.7$. From about 10 PeV to 1 EeV, it is $\gamma \approx -3.1$. Above 10 EeV, the spectral index flattens again to $\gamma \approx -2.6$. The regions between the different spectral indices are known as the "knee" (~ 3 PeV) and the "ankle" (~ 3 EeV). A cutoff in flux occurs at around 10^{11} GeV. This cutoff can be associated with the GZK-cutoff after K. Greisen, V. Kuzmin, and

G. Zatsepin [20, 21], which is predicted as the result of protons above the cutoff energy interacting with the cosmic microwave background (CMB) to produce a Δ^+ resonance:

$$p + \gamma_{\text{CMB}} \rightarrow \Delta^+ \rightarrow \begin{cases} p + \pi^0 \\ n + \pi^+ \end{cases} \quad (2.2)$$

This process then results in secondary particle energies below the cutoff energy.

Even though the exact origins of the knee and ankle remain unknown, there is consensus that cosmic rays at energies below the knee are mostly from inner-galactic origin [19]. In fact, a simple approximation with a 3 PeV proton and a homogenous magnetic field with the strength of the Milky Way ($6\mu\text{G}$ [22]) leads to a lamor radius of

$$r_l = \frac{p}{Ze \cdot B} \approx 0.5 \text{ kpc}, \quad (2.3)$$

which is around the thickness of the galactic thin disk [23].

The exact acceleration mechanisms for cosmic rays are still subject to research. However, for inner-galactic cosmic rays, shock accelerations in supernova remnants (SNRs) are seen as viable candidates [19]. In this process, cosmic rays diffuse back and forth across the supernova shock front. At each crossing, the energy of the magnetized plasma is transferred to the charged particle through Fermi acceleration, effectively increasing its energy. This transfer occurs multiple times until the particle escapes the shock front [15, 24]. Candidates for accelerators outside our galaxy are active galactic nuclei (AGNs) and gamma-ray bursts (GRBs). The former are black holes of $10^6 - 10^{10}$ solar masses at the center of their galaxy. They feed of matter from the equatorial accretion disk surrounding them, converting around 10% of that matter into highly energetic particle rays released at the black hole's poles [13]. The latter result from core collapses of heavy neutron stars or the merger of two neutron stars [13, 15].

Due to the charged nature of cosmic rays, they are naturally deflected in magnetic fields inside our galaxy and generally do not align in direction with their origin when arriving on Earth. This circumstance and their attenuation length of only a few hundred megaparsecs in the GeV to PeV regime [25] give cosmic rays a clear disadvantage for observations compared to gamma rays and neutrinos.

2.2 Gamma Rays

Photons at energies higher than 100 keV are known as gamma rays. It is assumed that their origins are the same galactic and intergalactic sources responsible for cos-

mic rays, where they are produced as secondary particles from leptonic and hadronic processes [12]. Leptonic processes producing gamma rays include:

- Bremsstrahlung: $e + N \rightarrow e + N + \gamma$, at a nucleus N
- Synchrotron radiation in a magnetic field: $e \rightarrow e + \gamma$
- Inverse Compton scattering: $e + \gamma \rightarrow e + \gamma^*$ with $E_\gamma < E_{\gamma^*}$

In hadronic processes, pions are created through interactions between cosmic rays and the surrounding interstellar medium. Neutral pions then decay directly into photons via $\pi^0 \rightarrow \gamma + \gamma$, while charged pions decay into charged leptons (and neutrinos), producing gamma rays through the leptonic interactions above.

Similar to cosmic rays, satellite-based observatories for the direct detection of gamma rays and ground-based observatories for the detection through secondary atmospheric shower particles exist. Through the use of various trackers to obtain directional information, the Fermi satellite [26, 27] was able to identify 6658 gamma-ray sources in an energy range from 50 MeV to 1 TeV. To measure fluxes at larger energies, ground-based telescopes such as Imaging Air Cherenkov Telescopes (IACT) need to be used. Here, large arrays of optical telescopes detect Cherenkov light in the upper atmosphere, coming from electromagnetic shower interactions between the gamma rays and air molecules [28]. The energy and direction of the gamma ray can then be determined by evaluating the detection times and light intensities of the detected signals.

The main observational advantage of gamma rays compared to cosmic rays lies in the fact that gamma rays are not deflected in the presence of electromagnetic fields. Their track will thereby always point back toward their origin. However, interstellar cloud layers are – similar to the atmosphere – opaque for gamma rays, making it difficult to see what is behind such objects. Additionally, their interaction with the extra-galactic background light (ELB) becomes dominant at high energies. At 1 TeV, the observational horizon for gamma rays is limited by that interaction to $z = 0.1$ [29]. For even higher energies of a few hundred TeV, CMB interactions limit the gamma-ray horizon to a few kiloparsecs [29].

2.3 Gravitational Waves

Gravitational waves are generated when highly massive objects undergo acceleration, as predicted by A. Einstein's *Theory of General Relativity*. When such objects move or interact, the curvature of spacetime is disturbed, causing ripples to propagate

outwards as gravitational waves. The strongest sources of gravitational waves are events such as the merger of compact binary systems, supernovae explosions, and the collapse of massive stars [30].

Due to the rigidity of spacetime, gravitational waves possess an exceptionally small amplitude, magnifying in relative changes of detector lengths of only 10^{-22} to 10^{-21} , making them challenging to detect. The first detection of gravitational waves was made at the LIGO observatory in 2015 [31], identified as originating from the merger of two black holes. Other gravitational wave detectors include Virgo [32] and KAGRA [33]. In principle, gravitational wave detectors are large laser interferometers, splitting a laser beam into two perpendicular arms and reflecting them back to recombine. A passing gravitational wave causes one arm to compress and the other to expand, leading to a measurable phase shift in the combined laser light.

Even though gravitational astronomy is still in its early stages, it could be a valuable contribution to multi-messenger astronomy. As neutron star mergers or supernovae often emit both gravitational waves and other messengers, detecting a gravitational wave could trigger insightful follow-up observations with other detectors.

2.4 Neutrinos

Neutrinos are uncharged leptonic particles. Like their charged counterparts, they come in three flavors and are subsequently named ν_e , ν_μ , and ν_τ . Because their nature as uncharged leptons makes them only susceptible to the weak force, neutrinos travel the universe mostly without interacting with other matter. This makes them, on the one hand, ideal for identification of their source directions and observations over large distances. On the other hand, their detection requires large volume detectors and long run times to gather enough data [15] from neutrino interactions. Further details on neutrino detection are given in chapter 3.1.

A multitude of origins determines the neutrino flux on Earth: From the cosmic neutrino background (CNB) over solar and atmospheric neutrinos to neutrinos from supernovae and high-energy astrophysical interactions. Figure 2.2 shows flux models and experimental data for those sources.

2.4.1 The Cosmic Neutrino Background

On the low-energy end of the flux spectrum, neutrinos from the CNB are dominant. Those neutrinos decoupled from matter around one second after the big

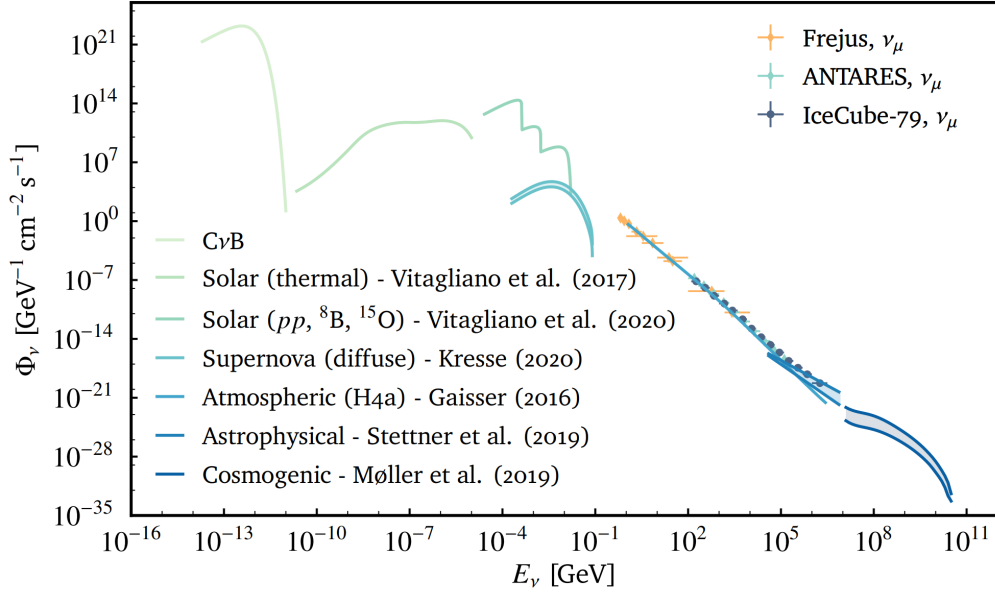


Figure 2.2: Neutrino flux models of various origins as a function of energy, including selected high-energy experimental results. If two lines are drawn for a specific contribution, they represent the upper and lower bounds of the specific model. Figure provided by F. Henningsen, based on [34–37].

bang ($k_B T \approx 1$ MeV), when the universe became too cold for $\nu_i \bar{\nu}_i \leftrightarrow e^+ e^-$ and $\nu_e e \leftrightarrow \nu_e e$ processes to ensure thermal equilibrium between neutrinos and charged leptons [38]. The then decoupled neutrinos experienced the same redshift as the remaining cosmic plasma, thereby still keeping its temperature. Later, around $k_B T \leq m_e \approx 0.5$ MeV, an electron-positron annihilation occurred by tipping over the $e^+ e^- \leftrightarrow \gamma \gamma$ equilibrium. This annihilation transferred entropy from e^+ / e^- to photons, increasing the photon background's temperature relative to the neutrinos. After this process, the ratio between the temperature of the neutrino background and the microwave background is expected to stay constant over time. It can be calculated by assuming a conserved entropy of the plasma $s \propto gT^3$ right before and right after the e^+ / e^- annihilation [38]. Here, g is the effective number of degrees of freedom, summing up 2 for each boson (here: γ) and $\frac{7}{4}$ for each fermion (here: e^+ / e^-). Performing the calculation leads to

$$\frac{T_\nu}{T_\gamma} = \left(\frac{g_{\text{after annihil.}}}{g_{\text{before annihil.}}} \right)^{1/3} = \left(\frac{2}{2 + \frac{7}{4} + \frac{7}{4}} \right)^{1/3} \approx 0.714. \quad (2.4)$$

With today's CMB temperature measured to be 2.72 K [39], this leads to an expected temperature of the cosmic neutrino background of 1.95 K. Due to this very low neutrino energy, detectors need to have exceptional resolution to distinguish signal from background. This requirement, combined with the neutrinos' generally low cross-section at low energies, makes the CNB even more challenging to detect than highly energetic neutrinos. However, should proposed detectors such as PTOLEMY [40] succeed in detecting the CNB, this could bring valuable insight into the history of the universe, allowing cosmologists to look back in time up to one second after the big bang.

2.4.2 Atmospheric Neutrinos, Solar Neutrinos, and Neutrino Oscillations

For a wide range of energies, atmospheric and solar neutrinos dominate the neutrino flux on Earth. Even though they are produced in distinctly different processes and technically do not qualify as cosmic messengers, they both give insight into a phenomenon called *neutrino oscillation*, which in turn allows for the deduction of the neutrino mass hierarchy.

As mentioned in chapter 2.1, cosmic rays hitting the Earth's atmosphere produce a shower of secondary particles. The neutrino production from those showers up to an energy of around 10^6 GeV is governed by the decay of light mesons such as kaons and pions [15, 41]. Those mesons decay via

$$\begin{aligned} \pi^+/K^+ &\rightarrow \mu^+ + \nu_\mu \\ \mu^+ &\rightarrow e^+ + \nu_e + \bar{\nu}_\mu \end{aligned} \quad \text{and} \quad \begin{aligned} \pi^-/K^- &\rightarrow \mu^- + \bar{\nu}_\mu \\ \mu^- &\rightarrow e^- + \bar{\nu}_e + \nu_\mu \end{aligned} \quad (2.5)$$

into muons, electrons and neutrinos. Assuming complete decay of the atmospheric muons, a neutrino ratio of $(1_e : 2_\mu : 0_\tau)$ would be expected on Earth from atmospheric showers. However, since for $E_\mu \geq 2.5$ GeV, the decay length for muons becomes longer than their average production height (≈ 15 km), the actual ratio is shifted towards muon neutrinos [15]. Because pions and kaons traverse the upper atmosphere, the neutrino flux from those decays heavily depends on its energy and incoming angle. Above approximately 10^6 GeV, neutrino production through baryonic decay becomes dominant. These baryons decay almost instantly, making the neutrino flux on Earth follow the power law of cosmic rays with $\gamma \approx -2.7$ [41].

Another source of the flux on Earth are solar neutrinos. Inside the sun, nuclear fusion exerts outwards pressure against the sun's own gravitational force. This fusion mechanism is described by the *p-p-chain*, fusing ^1H to ^4He through a series of different steps. The first step of the *p-p-chain*,

$$p \rightarrow n + e^+ + \nu_e \quad (2.6)$$

is the primary source of the solar neutrino flux with an additional thermal solar flux from interactions with the sun's plasma [42]. Solar neutrinos tend to possess energies in the range of tens of MeV. Their observation helps to better understand the inner working of the sun's fusion mechanisms.

A mismatch between the measured and predicted rates of different neutrino flavors from the sun became what is known as the *solar neutrino problem* [43]. Furthermore, similar mismatches have been found in the flavor rates for atmospheric neutrinos, where the measured rate of muon neutrinos was too low compared to the expected values. The solution to this problem lies in the discovery of neutrino oscillations:

The evolution of a neutrino state is determined by its Hamiltonian. While for propagation, this Hamiltonian is diagonalized by the neutrino mass basis (ν_1 ν_2 , ν_3), this basis differs slightly from the interaction basis (ν_e ν_μ , ν_τ). Both bases can be transformed into each other via the Pontecorvo-Maki-Nakagawa-Sakata (PMNS) matrix [44], which can be written as

$$U = \begin{pmatrix} 1 & 0 & 0 \\ 0 & c_{23} & s_{23} \\ 0 & -s_{23} & c_{23} \end{pmatrix} \begin{pmatrix} c_{13} & 0 & s_{13}e^{-i\delta} \\ 0 & 1 & 0 \\ -s_{13}e^{-i\delta} & 0 & c_{13} \end{pmatrix} \begin{pmatrix} c_{12} & s_{12} & 0 \\ -s_{12} & c_{12} & 0 \\ 0 & 0 & 1 \end{pmatrix} \quad (2.7)$$

with the sine and cosine of the weak mixing angle θ_{ij} denoted as s_{ij} and c_{ij} , respectively as well as a CP-violating phase δ . A neutrino initially in one of the interaction eigenstates, therefore, oscillates between interaction states during propagation as a result of phase shifts in the mass eigenstates because of differences in their mass $\Delta m_{ij}^2 = m_i^2 - m_j^2$. Assuming an ultra-relativistic approximation for the neutrinos due to their low mass, the probability for an initial neutrino of flavor α and energy E to be detected as flavor β at length $L = ct$ away from its origin is then [45]:

$$P_{\alpha \rightarrow \beta} = \delta_{\alpha\beta} - 4 \sum_{i>j} \Re (U_{\beta j}^* U_{\alpha j} U_{\beta i} U_{\alpha i}^*) \sin^2 \left(\frac{\Delta m_{ij}^2 L}{4E} \right) + 2 \sum_{i>j} \Im (U_{\beta j}^* U_{\alpha j} U_{\beta i} U_{\alpha i}^*) \sin \left(\frac{\Delta m_{ij}^2 L}{2E} \right) \quad (2.8)$$

By measuring flavor relations of neutrinos on Earth and comparing them to expected production rates at sources with known distances like the sun or Earth's atmosphere, estimates on the neutrino masses and the PMNS parameters can be made.

Notable experiments in that regard are Super-Kamiokande [46] and KamLAND [47]. Through experimental data, it could be shown that $|\Delta m_{32}^2| \simeq |\Delta m_{31}^2| \gg |\Delta m_{21}^2|$. Since the sign of Δm_{21}^2 remains unknown, the mass orders $m_1 < m_2 < m_3$ and $m_3 < m_2 < m_1$ are possible [13].

2.4.3 Neutrinos from Supernovae

In the same energy range as solar neutrinos, at a view tens of MeV, cosmic neutrinos originating from supernovae are located. Depending on its mass, a star undergoes a supernova explosion when its inner core runs out of material to keep the fusion process alive. This results in the star rapidly collapsing under its weight. During this collapse, the pressure inside the core causes protons and electrons to fuse to neutrons and neutrinos, creating a counter-pressure outwards. The resulting shock wave causes an explosion of the star [13]. Due to their low interaction cross-section, the neutrinos can escape the supernova unhindered, making them the first messenger of such an event to arrive at Earth. Even though the exact dynamics of a supernova event are still not fully understood, it is believed that neutrinos carry away the largest part of the supernova's emitted energy, with only 1% of the emitted energy stored in the expelled stellar material [12]. Because of the high number of stars in the universe, a diffuse, isotropic supernova neutrino background (DSNB) is expected, resulting from the integral of past supernova explosions [48].

2.4.4 High Energetic Cosmic Neutrinos

With the production of cosmic rays in accelerator environments comes the production of secondary neutrinos. This occurs predominantly through meson and muon decay in a process similar to what is observed in the Earth's atmosphere (equation 2.5), indicating a neutrino ratio of $(1_e : 2_\mu : 0_\tau)$. This ratio can be altered by strong magnetic fields in the source environment, removing the kinetic energy of the muon before decay and thereby suppressing the secondary muon decay, resulting in a ratio of $(0_e : 1_\mu : 0_\tau)$. An additional contribution from neutron decay in those environments contributes a flavor mix of $(1_e : 0_\mu : 0_\tau)$ [49]. Those flavor ratios change dependent on the distance between the source and the Earth as well as the energy of the neutrino. Probing the flavor ratio on Earth and accounting for oscillation can therefore lead to information about the source environment. Similar to supernova neutrinos, a distinction between point source flux and integrated diffuse flux from a multitude of sources can be made [15]. The diffuse flux has been measured by IceCube with a spectral index of $\gamma \approx 2.3\text{--}2.7$ [50]. Due to limited angular resolution, searching for point sources is more complicated. Progress has been made with the identification of TXS0506+056 [4] and NGC 1068 [5] as neutrino sources.

On the highest end of the neutrino energy spectrum of a few PeV, so-called cosmogenic neutrinos dominate, originating from GZK-pions (equation 2.2). However, due to their generally low flux, they remain challenging to detect [51].

2.5 Multi-Messenger Observations

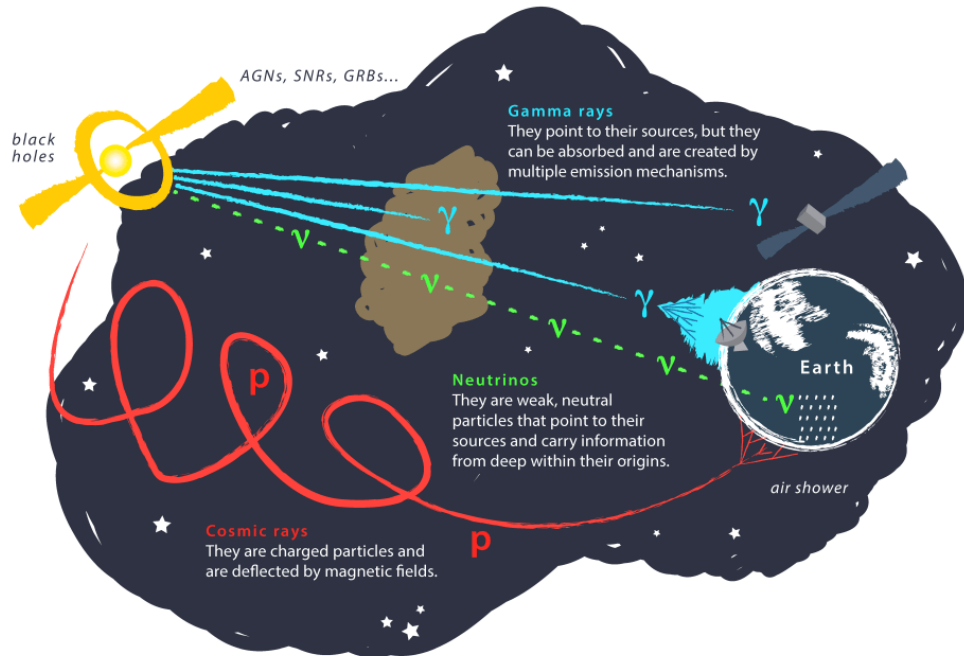


Figure 2.3: Graphical depiction of different cosmic messengers. Shown are cosmic rays (red), neutrinos (green), and gamma rays (blue) emitted from an astrophysical source. Figure from [52].

As previously discussed, cosmic accelerators such as AGNs, SNRs, or GRBs not only seem to be responsible for the production of cosmic rays but also for a flux of gamma rays and neutrinos detectable on Earth. To confirm this assumption, both neutrinos and gamma rays within an expected energy range and spectral index need to be detected from those sources. Additionally, an observation of the same cosmic event through multiple messengers helps to eliminate disadvantages that come with single messengers. That is their low interaction probability in detectors for neutrinos, the absorption in dust clouds and limited range of gamma rays, and the non-alignment with their source and limited range of cosmic rays. Throwing gravitational waves into the mix enables another, yet currently hardly detectable, messenger for the most violent cosmic events. Figure 2.3 summarizes various cosmic messengers and their observational advantages and disadvantages.

The history of multi-messenger observations began in 1987, with the supernova SN 1987A [53] when Kamikande-II, IMB, and Baksan detected an increased neutrino flux a couple of hours before the light from SN 1987A became visible. In 2017, the binary neutron star merger GW170817 [54] was detected as a gravitational wave by the LIGO and Virgo observatories. Around 1.7 seconds after the merger time, a gamma-ray burst consistent in direction with the gravitational wave was detected by the Fermi satellite. Those signals led to follow-up observations in the electromagnetic spectrum using a multitude of different telescopes. GW170817 marked the first gravitational wave detection that could be confirmed by other messengers.

With the emergence of neutrino telescopes, point source searches in the neutrino flux became viable. IceCube's discoveries of TXS0506+056 [4] and NGC 1068 [5] to be neutrino source candidates support the assumptions on messenger production in cosmic accelerators. As late as 2023, a neutrino signal could be identified consistent with a diffuse flux from the galactic plane of our own galaxy [6]. This discovery, consistent with gamma-ray observations of the galactic plane, led to the first neutrino-based map of the Milky Way. A new generation of neutrino telescopes hopes to improve these results further and get a sharper picture of the neutrino universe.

Chapter 3

Large Scale Neutrino Telescopes

As outlined in the previous chapter, large detector volumes are required to perform successful neutrino astronomy, because the generally low cross-section of highly energetic neutrinos causes them to interact only weakly with the detector. As it can be seen in this chapter, the detector medium additionally needs to possess a long attenuation length for photons in the visible spectrum. The detector must also be shielded from secondary atmospheric shower particles to suppress background signals. The subsequent search for a transparent medium deep under the Earth's surface with a size in the order of cubic-kilometers, naturally leads to the deep sea and the antarctic ice.

In the antarctic ice, located at the Amundsen-Scott South-Pole Station, sits the IceCube Neutrino Observatory [55], taking data since 2010. Complementary to IceCube in the Earth's northern hemisphere sit KM3NeT [56] and Baikal-GVD [57], both currently under construction, the former located deep in the Mediterranean Sea and the latter at the ground of lake Baikal in Russia. A new generation of neutrino telescopes is about to emerge with the development of the Pacific Ocean Neutrino Experiment (P-ONE) off the coast of Vancouver Island and upgrades to the existing telescopes.

The following chapter first gives an overview of the general detection principle for neutrino telescopes. After that, an introduction to the current and future generation of telescopes is given.

3.1 Detection Principle

The fundamental working principle of neutrino detectors lies in the detection of Cherenkov light from charged secondary particles created in neutrino interactions with the detector medium. In the following, each step of the process is described,

from the initial neutrino interaction, to the creation and propagation of light and the different signal-topologies the light leaves in the detector, depending on the interaction type. Last, background sources for detectors are discussed.

3.1.1 High Energetic Neutrino Interactions in Matter

Neutrinos in the standard model interact with other matter only through the weak force. Corresponding to the charge of the boson responsible for the interaction, high energetic neutrino interactions can be divided into neutral (NC) and charged currents (CC):

$$\nu_\alpha + N \xrightarrow{Z^0} \nu_\alpha + X \quad (\text{NC}), \quad \nu_\alpha + N \xrightarrow{W^\pm} l_\alpha + X \quad (\text{CC}) \quad (3.1)$$

During those processes, most of the energy is carried away by the secondary leptons (ν_α, l_α respectively), with the rest of the energy deposited in hadronic and electromagnetic particle showers X [15].

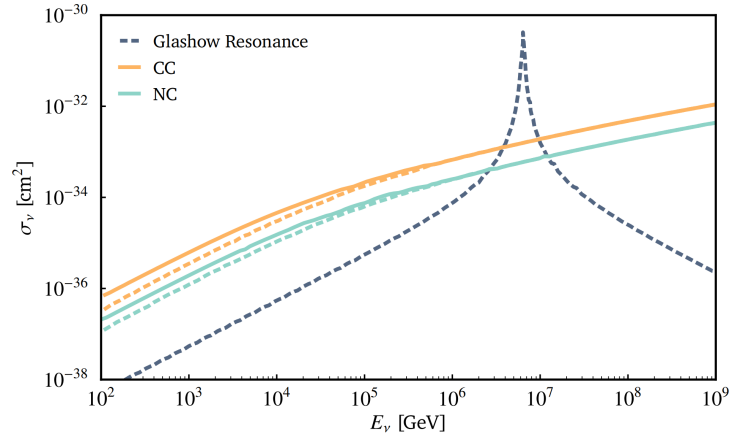


Figure 3.1: Cross-section for neutrino interactions through NC, CC, and Glashow resonance. Dashed lines represent anti-neutrino interactions, continuous lines represent neutrino interactions. Data from [58]. Figure provided by F. Henningsen.

The cross-section for those neutrino interactions is shown in figure 3.1. For energies in the GeV regime and above, the CC contribution to the neutrino interaction cross-section is significantly larger than the NC contribution [58]. At an energy of around 6.3 PeV, the cross-section peaks due to the Glashow resonance, describing the production of a W^- through an anti-electron-neutrino:

$$\bar{\nu}_e + e^- \rightarrow W^- \rightarrow X \quad (3.2)$$

For energies higher than 20 GeV, the neutrino interactions described above tend to be deeply inelastic [58]. As a result of the transferred energy from the neutrino to the scatter nucleus N , particle showers occur. Those showers, together with the charged lepton in the CC case, can produce Cherenkov light that can be detected by the neutrino telescope. A detailed discussion of the different event topologies those interactions leave in the detector can be found in chapter 3.1.4.

3.1.2 The Cherenkov Effect

If a charged particle travels through a medium, it will polarize its nearby environment. At slow speeds, this polarization travels with the particle, resulting in an approximately symmetric distribution around it. Therefore, the released electromagnetic wavefronts from the relaxation of that polarization will cancel out. That symmetry, however, is broken if the particle travels faster than the speed of light in that medium. In this case, the waveforms build a cone around the traversing particle, manifesting in the emission of light that is normal to that cone. This phenomenon is known as the Cherenkov effect [59, 60], after P. Cherenkov, who first discovered it in 1934.

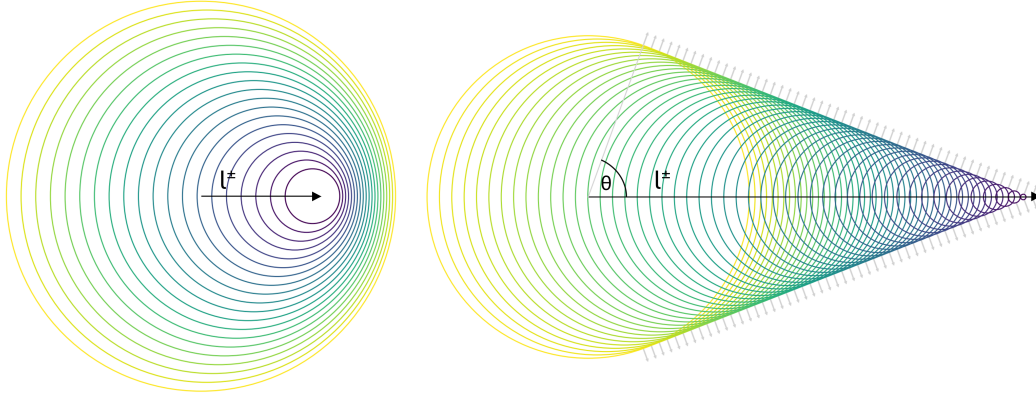


Figure 3.2: Illustration of the Cherenkov effect. A charged lepton is moving from left to right. Left: The particle is traveling slower than the local speed of light. No cone is created. Right: The particle is moving faster than the local speed of light. A Cherenkov cone is created, and light is emitted at angle θ .

Given the refractive index n of the material, the speed of light in that material is given as $c_n = c_0/n$. The angle of light emission by a particle of speed v can then be

calculated as

$$\cos(\theta) = \frac{1}{\beta \cdot n} \quad \text{with} \quad \beta = \frac{v}{c_0}. \quad (3.3)$$

Assuming water ($n \approx 1.3$) and a highly relativistic particle ($\beta \approx 1$), this leads to a Cherenkov angle of roughly 41° .

The number of emitted Cherenkov photons N per wavelength λ and distance x traveled by the particle is given by the Frank-Thamm formula [60]:

$$\frac{dN}{d\lambda dx} = \frac{2\pi\alpha z^2}{\lambda^2} \cdot \left(1 - \frac{1}{\beta^2 n^2(\lambda)}\right) = \frac{2\pi\alpha z^2}{\lambda^2} \cdot \sin^2(\theta) \quad (3.4)$$

with the fine structure constant α and the particle charge z . Since the amount of emitted photons scales with $\propto \lambda^{-2}$, the Cherenkov spectrum is dominated by smaller wavelengths. That is, until a cutoff wavelength, where due to a decreasing index of refraction, the condition $\beta > 1/n(\lambda)$ can no longer be satisfied. In water and ice, this results in a typical spectrum from 300 to 600 nm with around $3 \cdot 10^4$ photons emitted per meter, assuming $\beta \approx 1$ [61]. This spectral range coincides well with the quantum efficiency of a typical photomultiplier tube on a bialkali basis [62].

3.1.3 Attenuation of Cherenkov Light

Inside the detector medium, the emitted Cherenkov photons are subject to attenuation through absorption and scattering. These processes can be effectively described through the absorption and scattering lengths l_{abs} and l_{scat} respectively. These lengths denote the average path length, after which only a fraction $1/e$ of all initial photons remain unaffected by these processes. Both lengths can be combined to the attenuation length

$$l_{\text{att}} = \left(\frac{1}{l_{\text{abs}}} + \frac{1}{l_{\text{scat}}} \right)^{-1}. \quad (3.5)$$

While absorbed photons disappear and deposit their energy in the medium, scattered photons change direction. This scattering is described by a scattering function, that is, the probability that the photon scatters at any given angle δ . This function heavily depends on the given detector medium and the photon wavelength [63]. The scattering length can be normalized with respect to different scattering functions through the so-called effective scattering length:

$$l_{\text{scat}}^{\text{eff}} = \frac{l_{\text{scat}}}{1 - \langle \cos(\delta) \rangle} \quad (3.6)$$

utilizing the cosine of the mean deflection angle $\langle \cos(\delta) \rangle$ [63]. The length $l_{\text{scat}}^{\text{eff}}$ can thereby be understood as some form of isotropization length, at which estimation of the source direction becomes imprecise. For water and ice, scattering happens predominantly in the forward direction, with $\langle \cos(\delta) \rangle \approx 0.85 - 0.90$ [63]. Different absorption and effective scattering lengths, as well as resulting attenuation lengths for locations of neutrino telescopes, are given in table 3.1.

Site	l_{abs} (m)	$l_{\text{scat}}^{\text{eff}}$ (m)	l_{att} (m)
Lake Baikal, 1 km depth	18–22	150–250	16–20
Ocean, > 1.5 km depth	40–70	200–300	33–56
Polar ice, 1.5–2.0 km depth	~95	~20	~16
Polar ice, 2.2–2.5 km depth	> 100	30–40	> 25

Table 3.1: Approximate absorption and effective scattering lengths with resulting attenuation length for different locations of neutrino telescopes. Lengths stated in water are subject to seasonal change. Absorption and scattering lengths taken from [63].

Precise knowledge of the different attenuation lengths inside the detector is not only crucial to reconstruction efforts, it also affects the detector geometry itself. As enough light hitting the detectors’ optical modules is crucial for signal quality, their spacing should be within the absorption length. Additionally, the detector’s angular resolution can be limited if the module spacing far exceeds the scattering length, as high scattering inside the medium heavily influences the time distribution of the incoming photons.

3.1.4 Event Topologies

Depending on the interaction type described in chapter 3.1.1 and their subsequent secondary particles, different event topologies are seen inside a detector. Generally, they can be classified as so-called *cascades*, *tracks*, and *double bangs*. Exemplary events of those topologies recorded in IceCube are shown in figure 3.3.

Tracks result from CC interactions with muon neutrinos. Depending on the detector material, the secondary muon can travel unhindered for kilometers [7]. The resulting long trail in the detector can be reconstructed by detecting the Cherenkov photons emitted at $\sim 41^\circ$ relative to the muon direction. Tracks can either enter the detector after interactions in the surrounding material or start within. In the latter case, a particle shower at the track origin resulting from the initial neutrino interaction might also be detected. Because not all of the muon’s energy is deposited inside

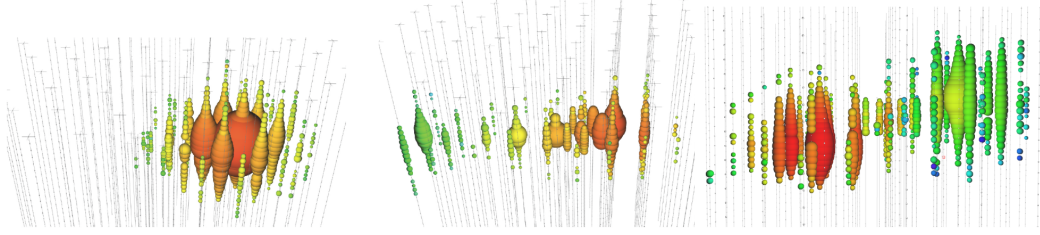


Figure 3.3: Illustration of a cascade (left), a track (middle), and a double bang (right) recorded in the IceCube Observatory. The spheres represent the optical modules with their size correlating to the detected amount of photons and their color to the photon arrival time. Figures from [64].

the detector, a reconstruction of the neutrino’s initial energy can only be done on a statistical basis. The long lever arm of the muon track makes them ideal for neutrino astronomy, as it allows for an easier angular reconstruction compared to other topologies while pointing on average only $\sim 1^\circ$ away from the initial neutrino direction at high energies [15].

Cascades are produced in all NC interactions as well as in CC interactions of the electron flavor. The resulting shower-hadrons – and, in the CC case, the secondary electron – have short interaction lengths and will therefore deposit all their energy close to the initial interaction vertex. Since in the NC case, the secondary neutrino carries most of the interaction energy, only a portion of the total energy is deposited in the detector [15]. For the CC case, however, all of the neutrino’s energy is deposited. Cascades usually have lengths of ~ 10 m in water and ice, which is less than the typical module spacing of a detector [15]. The angular resolution of cascades is, therefore, worse than the resolution for tracks. On the other hand, the energy resolution is better since most of the energy is deposited inside the detector medium.

Double bangs originate in τ -flavored CC interactions at energies in the PeV regime and above. A hadronic cascade (1st bang) is generated at the initial neutrino vertex, with the τ -lepton carrying away most of the energy. The τ then leaves a signature inside the detector similar to a muon track, until it decays after a relatively short distance (≈ 50 m at 1 PeV) [15]. The decay leaves behind either a hadronic or electromagnetic shower, depending on the decay channel (2nd bang). At energies lower than 1 PeV, the decay length of the τ becomes so short that both bangs become virtually indistinguishable, leaving a single cascade in the detector. Since high energetic atmospheric ν_τ neutrinos are rare, with less than 100 expected per

km³ of water per year [65], the occurrence of a double bang can with high certainty be contributed to an astrophysical neutrino.

3.1.5 Causes of Background Signals

Besides a background from atmospheric muons and neutrinos (discussed in chapters 2.1 and 2.4.2 respectively), background light from inside the detector volume can influence the detectors performance. One such intrinsic cause is the decay of radioactive isotopes, mainly ⁴⁰K, close to the optical modules. The β^- -decay of ⁴⁰K produces an electron of up to 1.4 MeV, which can produce Cherenkov radiation, while the electron capture of ⁴⁰K produces a photon directly, which can then generate energetic electrons through Compton scattering, producing Cherenkov photons [66]. Especially for water-based detectors, bioluminescence caused by deep-sea organisms is another major cause of background photons. This light emission, usually triggered by currents around the module and organisms coming in contact with the same, has a spectral peak in the range of 440 nm to 500 nm, and is thereby hard to distinguish from Cherenkov light [66]. Another source for background is intrinsic to the optical modules, as thermal excitations in a photodiode can cause signals similar to a single photon event [1].

Fortunately, the intrinsic backgrounds mentioned here produce light correlated on much larger timescales than a signal caused by neutrino interactions. To subsequently eliminate those backgrounds, coincidence triggers are often applied, meaning that a signal has to be detected at multiple places inside the detector, correlating in a nanosecond time window [55].

3.1.6 Angular Sensitivity for Astrophysical Neutrinos

Atmospheric muons and neutrinos pose significant background in the detector, causing the need to obtain large amounts of events to successfully identify astrophysical point sources. Roughly speaking, a $n\sigma$ detection of an event requires

$$N_{\text{events}} - N_{\text{atm}} > n \cdot \sqrt{N_{\text{atm}}} \quad (3.7)$$

within a given $\delta\theta$ around a source [15]. Here, N_{events} is the total number of events, and N_{atm} is the number of atmospherical background events in the same region. The Earth can be used as a natural shield to suppress the background from atmospheric muons and subsequently increase the detector sensitivity, limiting observations to downward directions. Neutrinos, on the other hand, are less affected while traveling through the Earth, with absorption becoming relevant only at > 100 TeV. As this

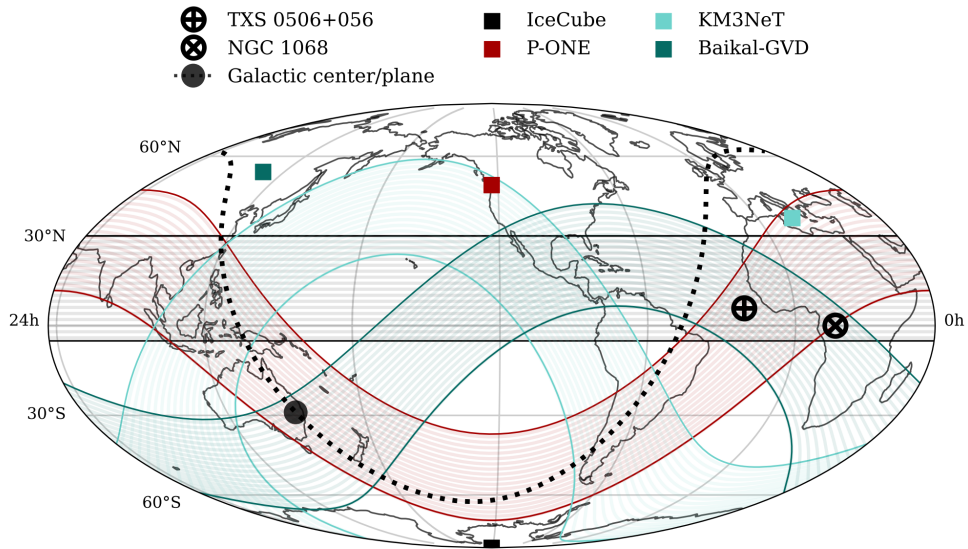


Figure 3.4: Positions of neutrino telescopes included in PLE ν M and their respective region of highest sensitivity projected on Earth. Projections of the galactic center and plane and two neutrino point sources discovered by IceCube are depicted as well. Figure provided by L. Schumacher.

absorption at high energies affects both astrophysical and atmospheric neutrinos, neutrino telescopes typically tend to be most sensitive around their respective horizon. In order to effectively identify point sources in the entire sky, the field of view of multiple neutrino telescopes need to be combined. Concepts for such a global neutrino monitoring have been put forward with PLE ν M [8], laying out how combined efforts of IceCube, KM3NeT, Baikal-GVD, and P-ONE can improve discovery potentials in the northern hemisphere by up to three orders of magnitude compared to IceCube alone.

Figure 3.4 shows the most sensitive areas of current and future neutrino telescopes projected onto the Earth, highlighting a much larger combined area of sensitivity. In the following sections, a brief introduction on each of the telescopes is given.

3.2 IceCube

After the operation of the AMANDA pathfinder [67] in the late 90s and early 2000s, the IceCube Observatory [1, 55, 68] was built as the world's first cubic-kilometer

neutrino telescope, located at the South Pole in the antarctic ice. Completed in 2010, it consists of 86 detector strings containing 60 digital optical modules (DOMs) each, in a depth of 1450 m to 2500 m. In addition to the 79 string, cubic-kilometer detector array, IceCube also contains a denser array of 7 strings in the detector core for low energy observations, called *DeepCore* as well as an air shower array on the surface called *IceTop*. The detector is schematically drawn in figure 3.5.

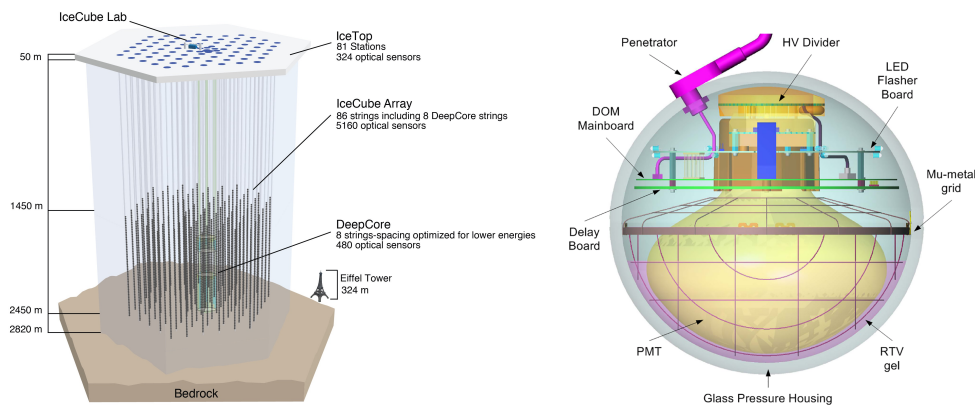


Figure 3.5: Left: Schematic drawing of the IceCube detector, featuring the detector array, DeepCore, and IceTop, with the Eiffel Tower for scale. Right: A schematic drawing of the IceCube DOM with PMT and electronics in a glass housing. For details on those drawings, refer to the text. Images courtesy of the IceCube collaboration.

The DOM, also shown in figure 3.5, centers around a downwards-facing 10-inch Hamamatsu R7081 photomultiplier tube, which is optically coupled to the glass housing. Located behind the PMT are various electronic boards, responsible for supplying the PMT with high-voltage, data acquisition, calibration, and communication with the surface [55]. Since the DOM is subject to high pressure under the ice, the housing consists of two 13-inch glass hemispheres, which serve as a pressure housing to protect the instruments on the inside. A penetrator in the upper hemisphere allows for a cable connection to the outside. For calibration purposes, twelve 405 nm LEDs inside the DOM are able to emit light into the surrounding ice. Other DOMs can, in turn, detect this light, and – together with timing information – allowing it to be used to calibrate geometric and optical properties [69, 70].

Based on a site characterization by the AMANDA pathfinder [71], the string distance in the IceCube Array has been set to 125 m, with DOMs on one string spaced 17 m apart [68]. The DeepCore array, optimized for lower energies, possesses a 42 m string

spacing with 7 m between individual DOMs. While the IceCube Array is built for energies beyond 100 GeV up to some PeV, DeepCore is optimized for events in the range from about 10 GeV to about 100 GeV and aims for the investigation of neutrinos produced from WIMP dark matter annihilations, atmospheric neutrino oscillations, and galactic supernova neutrinos [72]. On the surface above sits the aforementioned IceTop Array, consisting of 162 ice-filled tanks instrumented with PMTs. IceTop allows for a veto mechanism for events of atmospheric origin, but also for an independent study of cosmic rays within 100 TeV to 1 EeV as well as PeV gamma rays [73].

The next generation of IceCube, IceCube-Gen-2, aims to extend the current detector to about 8 km³ of probed ice with an additional 1000 optical sensors. This less dense array is hoped to significantly increase the angular resolution, and with that, the point source search capabilities of IceCube [74]. As a first step towards IceCube-Gen-2, seven new, densely populated strings are planned to be embedded near the current DeepCore Array, as part of the so-called IceCube Upgrade. In this scope, a total of 693 optical modules are planned to be deployed, 402 of them being multi-PMT modules (mDOMs) [75]. An additional 50 independent calibration devices are supposed to gather more profound insight into the characteristics of the surrounding ice. With those upgrades, a more precise sensitivity to neutrino oscillations at a few GeV, especially regarding tau-neutrino occurrence, is possible [74].

3.3 KM3NeT

KM3NeT [2, 56] is a research infrastructure currently being installed in the deep Mediterranean Sea. Locations are offshore Toulon in France and Portopalo di Capo Passero in Sicily, resulting in a network of several neutrino detectors. KM3NeT combines work from the predecessor experiments NESTOR [76], NEMO [77], and ANTARES [78] in the deep sea.

As the center-piece of the KM3NeT detector serves its digital optical module (DOM), shown in figure 3.6. In contrast to IceCubes DOM, a multi-PMT approach was selected, with 31 three-inch PMTs per module, pointing almost uniformly outwards. Each module is encompassed in a glass sphere of 0.44 m diameter with a cable break-out at the top. The PMTs are surrounded by a metallic reflector towards the side of the glass housing, the so-called *light collection rings*, to increase their respective photon capture area [79]. For calibration purposes, each module is equipped with acoustic emitters and receivers, enabling distance measurements between individual DOMs. Additionally, compasses and accelerometers are present in every DOM and serve supplementary calibration purposes regarding ocean currents [79].

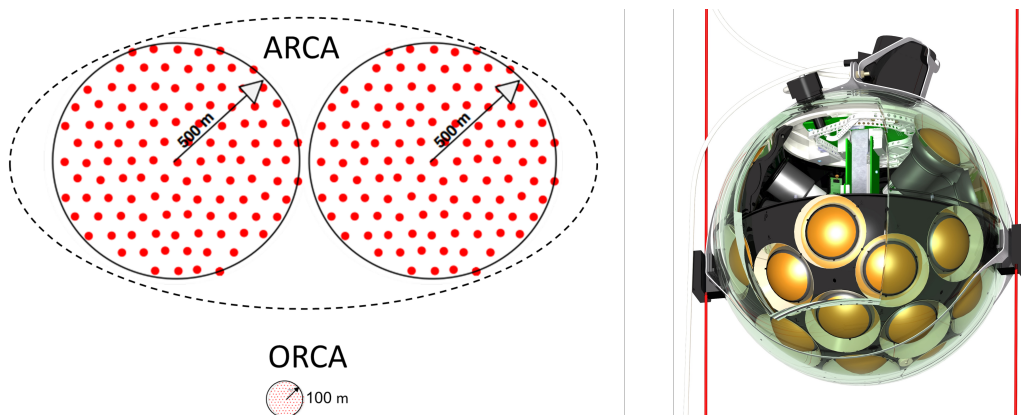


Figure 3.6: Left: Schematic drawing of the KM3NeT arrays ARCA and ORCA in their respective relative sizes. Right: A CAD drawing of the KM3NeT DOM. The DOM is cut open to reveal the inside. For details on the drawings, refer to the text. Images courtesy of the KM3NeT collaboration.

Once finished, KM3NeT will consist of two detector arrays, ARCA (Astroparticle Research with Cosmics in the Abyss) and ORCA (Oscillation Research with Cosmics in the Abyss) at its two locations respectively [80]. ARCA will feature 230 lines, so-called *detection units* with 18 DOMs per line at a length of 700 meters. As of September 2022, 21 lines were functional and transmitting data to shore [81]. The ARCA detection units will be placed sparsely in two clusters, each around 500 m in radius. This geometry optimizes the search for very highly energetic neutrinos, with a special focus on neutrinos from the galactic plane [56]. ORCA, on the other hand, will implement the same detection units as ARCA, however with 115 units spaced in a 100 m radius, optimizing the detector for energies in the GeV range. The main goal of ORCA is the study of fundamental neutrino properties, such as neutrino oscillations, and with that, the neutrino mass hierarchy. Currently, 8 ORCA detection units are operational [82]. Both the ARCA and ORCA arrays in their respective relative size are shown in figure 3.6.

3.4 Baikal-GVD

In Lake Baikal in Russia, at a depth of about 1 km, sits the Gigaton Volume Detector (Baikal-GVD). The telescope follows a clustered structure, with 8 strings per cluster and 36 optical modules per string. Strings are separated 60 m apart with 300 m cluster spacing [3, 57]. Since April 2022, ten such clusters are deployed and

operational. Plans exist for a total of 16–18 clusters deployed by 2025–2026, resulting in a total detector volume of over 1 km^3 [3]. With Western support for the project cut off in early 2022, it remains unclear to which extent Baikal-GVD will provide towards scientific findings in the foreseeable future.

3.5 P-ONE

The Pacific Ocean Neutrino Experiment (P-ONE) [7, 83] is a cubic kilometer neutrino telescope currently in its development stage. P-ONE will be connected to the NEPTUNE Observatory [84], a deep-sea research and infrastructure network off the coast of Vancouver Island, operated by Ocean Networks Canada (ONC). Following two successful pathfinder missions, STRAW [85] and STRAW-b [86] respectively, the Cascadia Basin, with a depth of around 2660 m has been chosen as the location for P-ONE. The site proves ideal with relatively weak ocean currents of 3 to 7 cm/s [83], stable temperatures around 2° Celsius [87], and five pre-existing NEPTUNE nodes, constantly powered and instrumented by ONC.

The entire envisioned P-ONE detector is shown in figure 3.7. In its complete configuration, P-ONE is planned to consist of 70 strings, each containing 20 modules, with the final geometry still subject to optimization [88]. A first prototype line, called P-ONE-1, aiming to be technologically identical to future lines, will be deployed in 2024/2025 and is currently in development. The goal of PONE-1 mainly lies in proving the design and calibration concepts and gathering as much data as possible to understand the data stream for upcoming lines. After P-ONE-1, a first cluster of several strings, called P-ONE Demonstrator, is planned as a further proof of concept and for initial neutrino observations. The entire detector is planned to be finished late in this decade. A technological overview of P-ONE-1 will be given in chapter 4.

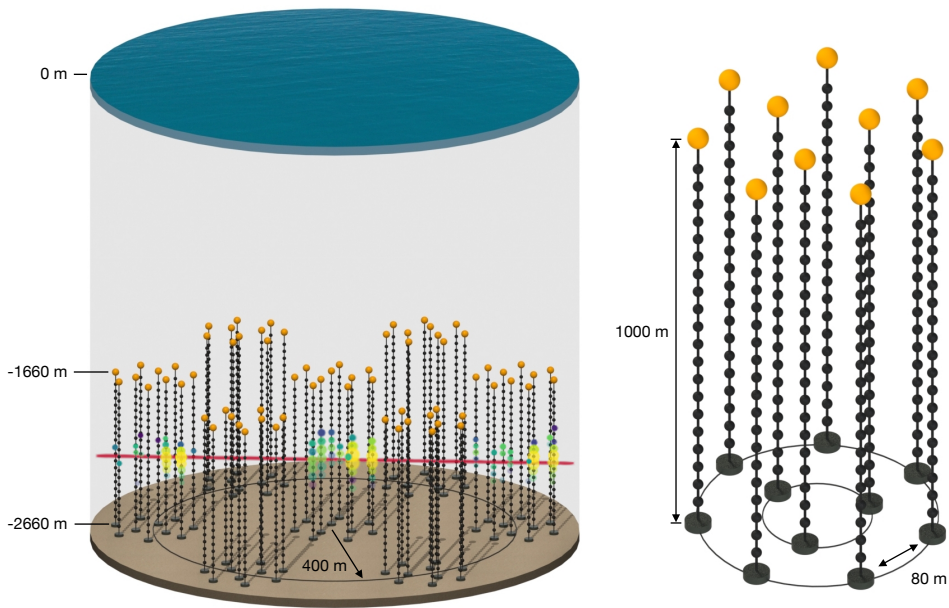


Figure 3.7: The preliminary P-ONE detector design with the full 7 clusters (left) and one individual cluster consisting of 10 strings (right). Strings will consist of 20 modules each at a total length of one kilometer. A geometry optimization for the entire detector is currently still ongoing [88]. Figure courtesy of the P-ONE collaboration.

Chapter 4

The First Line for the P-ONE Detector

P-ONE-1 depicts the first line of the full P-ONE detector [89]. As such, it is supposed to serve as a technological blueprint for future detector lines, providing a proof of concept for their design and helping to gather data valuable for the future detector development process. P-ONE-1 will consist of 20 modules distributed over one kilometer in height. Up to three of these modules will be dedicated modules for the detector calibration. In the following chapter, P-ONE-1's string design, as well as the optical and calibration modules, are presented. A schematic drawing of the line and both module types is shown in figure 4.1.

4.1 P-ONE-1 String Design

P-ONE-1's 20 modules are connected by an integrated backbone cable, which terminates at the bottom in a so-called *mooring junction box* (mJB). This mJB serves as the interface between the line and the NEPTUNE observatory and houses, among others, a central clock for time synchronization between P-ONE instruments and a trigger computer [89, 90]. Physically connected to the mJB is the deployment frame, which serves as a holding structure for the line during transportation and deployment, and as its anchor once deployed.

The backbone cable was designed by combining a load-bearing aramid braid with a hybrid electro-optical power and communication cable. The connection between the cable and individual modules sits inside the module's titanium ring, with the necessary cables spliced out and the rest of the cables fed through to the next module [89]. A novel multi-layered sealing system allows for this in-module splicing, while the load of the line is transferred through the titanium rings. This cable approach eliminates the need for in-water connectors susceptible to failure, while allowing for a more streamlined design that is less prone to entanglement during deployment and without cable shadow in the field of view of the PMTs [89].

On top of the line sits a buoy which will serve as the necessary source of buoyancy to keep the line upright in the water. During deployment, the entire frame with the rolled-up detector line will first be lowered to the sea floor. After initial inspections and connection of the mJB to the NEPTUNE node, the buoy is then released, traveling upwards and thereby unfolding the entire detector line [89]. To reduce stress on the line and deployment frame during this process, shock absorbers will be placed between the mJB and the frame.

4.2 The Optical Module (P-OM)

The optical module of P-ONE-1 (P-OM), as depicted in figure 4.1, follows a multi-PMT approach similar to the DOM of KM3Net and the mDOM of IceCube Upgrade. This approach allows for simple coincidence triggers inside each module, thereby reducing background events originating from radioactive decay or bioluminescence (ref. chapter 3.1.5). The module is split in two borosilicate glass hemispheres of 17 inches, with the cable breakout located inside the titanium ring between the hemispheres. Each hemisphere houses 8 PMTs, resulting in 16 PMTs for the entire P-OM. The PMTs are spring-mounted, pressing against the outer glass, to accommodate temperature gradients, hydro-static compression, and vibration and shock impacts during transportation and deployment [89]. Between the PMT and the outer glass sits a silicon-based gel pad to optically couple both components and minimize refraction effects. The gel pads' opening angle was optimized for photon capture towards the PMT, utilizing total internal refraction at its side to increase the effective photocathode area [91]. Unlike the KM3Net design, no solid reflector encircles the PMT. This allows for photons at high incidence angles, which initially do not get captured by a gel pad, to traverse inside the module to another pad, where they subsequently can be captured by a PMT. Monte Carlo studies conducted in the scope of this thesis (ref. chapter 6.4) confirm the effectiveness of this approach. The mounting scheme and easily removable gel pads allow for the replacement of a PMT at virtually any time during production and testing of a module.

PMTs are supplied with high voltage by the μ Base [75], a high voltage generator and divider initially developed for the IceCube Upgrade mDOM (ref. chapter 5.2). Each hemisphere is planned to contain a so-called *interposer board*, managing UART communication to the μ Bases as well as to additional calibration devices inside the respective hemisphere, including light beacons, axicons for light collimation, and acoustic receivers [92, 93]. The interposer boards of both hemispheres, in turn, connect to the mainboard, situated in one of the hemispheres. The mainboard receives the analog PMT signals directly via coax cables from the μ Bases and digitizes them

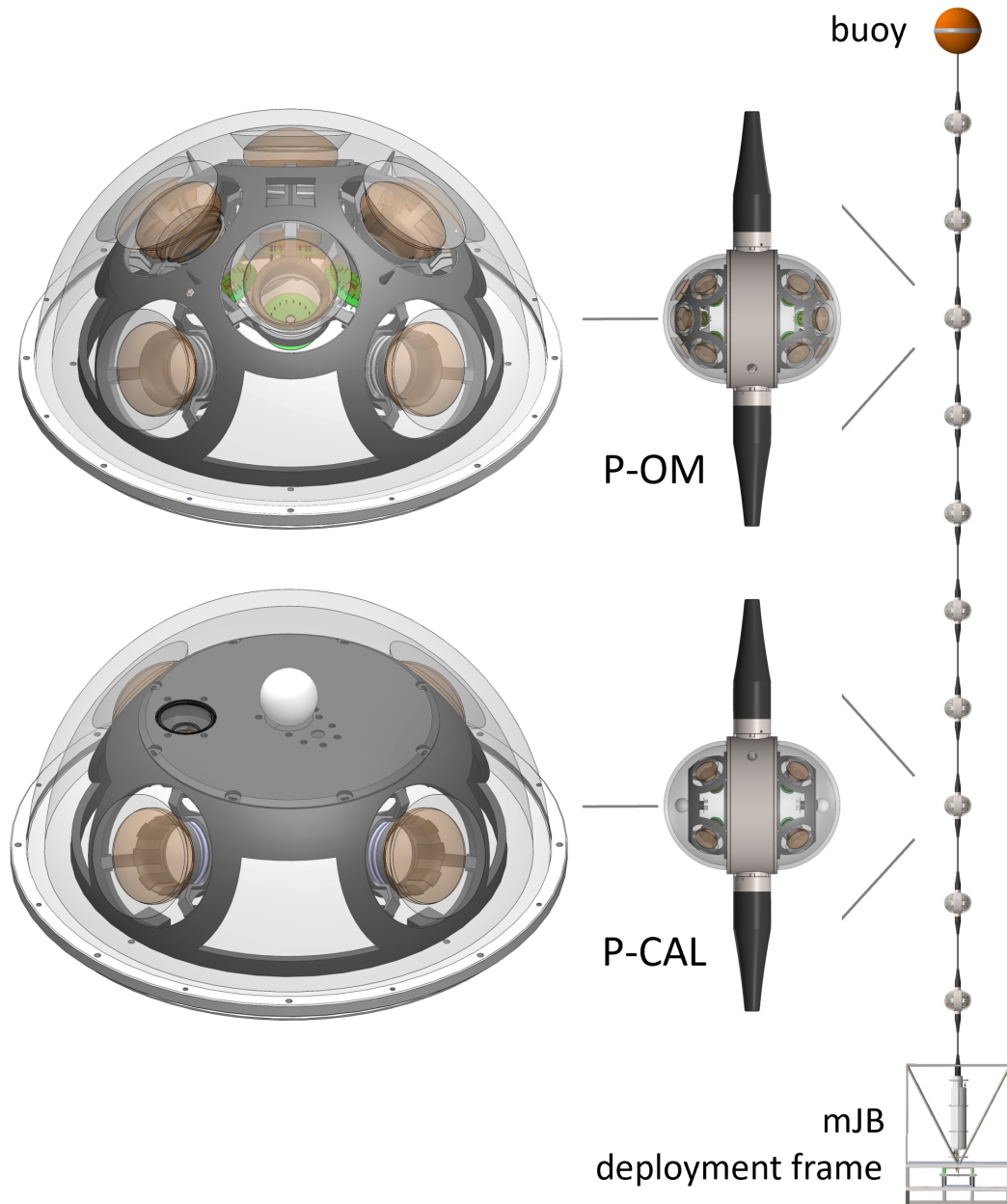


Figure 4.1: Schematic drawing of the P-ONE-1 line. The real line will consist of 20 modules over 1 kilometer in length. Drawn in detail are the P-OM and the P-CAL with a further zoom-in on the respective hemispheres. For details on line and modules, refer to the text. Images provided by C. Spannfellner, after [89].

via a built-in ADC. In addition, it centrally manages the P-OMs operating system and is responsible for communication with the mJB and neighboring P-OMs [90]. A Silicon Muon Tracker (SMUT) is planned to be integrated into the hemisphere without a mainboard.

4.3 The Calibration Module (P-CAL)

In principle, P-ONE-1s calibration is based on a hybrid acoustical and optical approach. For geometric and timing calibration, sea-floor-based hydrophones will emit signals that are captured by acoustic receivers coupled to the glass sphere of every module [93]. Additional geometrical, optical, and timing calibrations are performed by directional flasher beacons in every module, which emit light that is detected by other modules' PMTs [92].

Further, P-ONE-1s' calibration module (P-CAL), as depicted in figure 4.1, is equipped with isotropic, high-power, nanosecond light pulsers, flashing in wavelengths between 300 and 600 nm, and a self-monitoring system based on the Precision Optical Calibration Module (POCAM) [94]. The design of the P-CAL is similar to the design of the P-OM, with one of the rows of PMTs removed to make space for the aforementioned light beacon, sitting under a Teflon diffuser to ensure isotropy. The diffuser is coupled to the glass via optical gel. The P-CAL is additionally equipped with an outwards-facing camera, allowing for the study of biofouling and bioluminescence on the modules [92].

Chapter 5

The P-ONE Optical Module Calibration Unit

The Optical Module Calibration Unit (OMCU) has been developed in order to measure the characteristics of P-ONE-1s photomultiplier tubes (PMTs) and to probe their behavior under different conditions.

It was developed with the objective to automate procedures as much as possible, offering a plug-and-play solution for PMT testing and, eventually, saving valuable testing time as well as ensuring easily reproducible results. In the scope of this thesis, the entire software for the OMCU has been overhauled, together with some changes to the OMCU hardware. This chapter gives an overview of the OMCU's key components: the PMT and the μ Base. After that, the remaining setup and its control software are presented. Finally, measurement data from conducted PMT tests is compared to the data provided by the PMT manufacturer.

5.1 Photomultiplier Tubes

A photomultiplier tube (PMT) is a high-sensitivity detector for weak light signals from the near-infrared to the near-ultraviolet regime [95, 96]. PMTs can convert incoming photons to electric signals by electron excitation through the photoelectric effect and subsequent multiplication of the excited electrons. Figure 5.1 shows this process schematically.

As a first step in the PMT detection process, an incoming photon has to excite an electron from the valence band to the conduction band of the photocathode through the photoelectric effect. This electron then needs to drift toward the edge of the photocathode and overcome the vacuum level barrier to reach the PMTs vacuum chamber. Therefore, the minimal excitation energy for the electron equals the energy difference between the photocathode's Fermi level and the vacuum level, also known

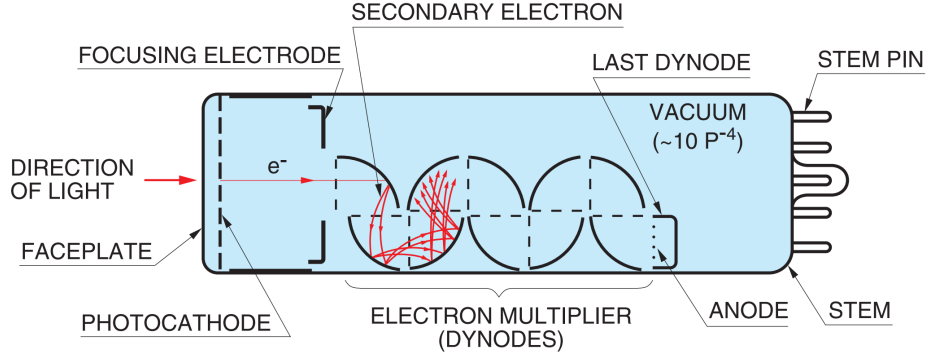


Figure 5.1: Schematic working principle of a PMT. A photon is absorbed in the photocathode, and the subsequent excited electron is multiplied in the dynode structure. Figure from [96].

as the work function Ψ . By extension, this energy difference equals the minimal energy a photon needs to possess to be detected in the PMT. The excitation of electrons into the vacuum through incoming photons can subsequently be described by the probabilistic process [96]

$$\eta(\nu) = (1 - R) \cdot \frac{P_\nu}{k} \cdot \frac{1}{1 + 1/kL} \cdot P_s \quad (5.1)$$

for the so-called quantum efficiency η . The reflection coefficient of the photocathode is given as R . P_ν denotes the probability that light absorption leads to an electron excited to a higher level than the vacuum. The total photon absorption coefficient is given as k , while the mean escape length of excited electrons is given by L , and the probability that electrons that reach the surface of the photocathode are released into the vacuum is P_s . Those parameters heavily depend on the wavelength of the incoming light ν and material parameters such as the work function. Commonly used materials for photocathodes are cesium-antimony (Cs_3Sb), bialkali (K_2CsSb), and multi-alkali ($\text{Na}_2\text{KSb:Cs}$) [96].

After excitation out of the photocathode, the electron is accelerated by an electric field towards the focusing electrode and subsequently into the dynode structure. Depending on the momentum and position of the incoming photon, the electron might have unfavorable launch angles resulting in an absorption before it can reach the first dynode. The probability that an excited photon reaches the first dynode is expressed through the collection efficiency C_e . In optimized PMT geometries, collection efficiencies between 60% and 90% can be reached [96].

In the dynode structure, the electron is then multiplied by the production of sec-

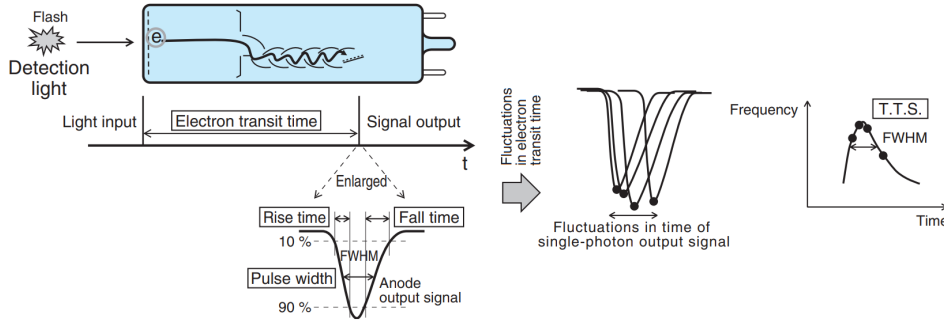


Figure 5.2: Schematic illustration of the electron transit time and the occurrence of transit time spread. Figure from [96] (modified).

ondary electrons. Dynodes are covered by a secondary emissive surface, often alkali-antimonide (Sb), beryllium-oxide (BeO), or magnesium-oxide (MgO) [96]. After the impact of an electron on those surfaces, a number of secondary electrons δ is released, which travel towards the next dynode. Depending on the number of dynodes n , the total number of electrons from a single photo-electron (s.p.e) that reaches the anode is then

$$\mu = \delta^n. \quad (5.2)$$

The number of secondary electrons itself can be expressed through the interstage voltage between the dynodes U_i and a parameter dependent on the dynode material k as $\delta \propto U_i^k$ [95]. The total number of electrons deposited at the anode from a single photo-electron, the so-called "gain" can then be described as

$$\mu = A \cdot U_s^{k \cdot n}. \quad (5.3)$$

The constant A depends on the dynode material. The total supply voltage is noted as U_s . Applying Ohms Law allows to set the gain in relation to the charge Q_A and voltage U_A at the anode output:

$$Q_A = \mu \cdot e = \frac{1}{R} \int U_A(t) dt \quad (5.4)$$

The voltage can then be measured directly by an oscilloscope connected to the PMT.

Due to fluctuations in the electron flight times, the charge is not deposited at once at the anode but spread over time, resulting in a characteristic waveform with rise and fall times defined as the times between the 10% and 90% values, respectively [95]. The transit time is defined as the time between the light input and the peak of the waveform. The so-called transit time spread is the width of the distribution of transit times. PMTs tend to respond exceptionally fast to light signals, with transit

times often in the order of dozens of nanoseconds [96] depending on the dynode geometry, type, and supply voltage. Transit time spreads usually sit below 10 ns, with some dynode geometries achieving values down to 0.3 ns.

For the P-ONE prototype line, the Hamamatsu R14374, a head-on type, bialkali photocathode [62] with a spectral response of 300 to 650 nm, was chosen amongst a list of possible candidates of 3-inch PMTs [97] and subsequently tested in the OMCU. A comparison between the data acquired in those tests and the PMT characteristics provided by Hamamatsu can be found in chapter 5.5.

5.2 The μ Base

The μ Base is a high-voltage supplier and divider designed to distribute voltage across the dynodes and to provide a connection for the anode output signal to the readout electronics. It was initially developed by C. Wendt for the Hamamatsu R15458-02 PMT in the scope of the IceCube Upgrade multi-PMT optical module (mDOM) [75]. The μ Base was considered for the use in the P-OM early in the design process due to its proven concept, low power consumption, adjustability, and small form factor. The compatibility with the P-OMs R14374 PMT was proven in the scope of this thesis. Figure 5.3 shows a block diagram of the μ Base.

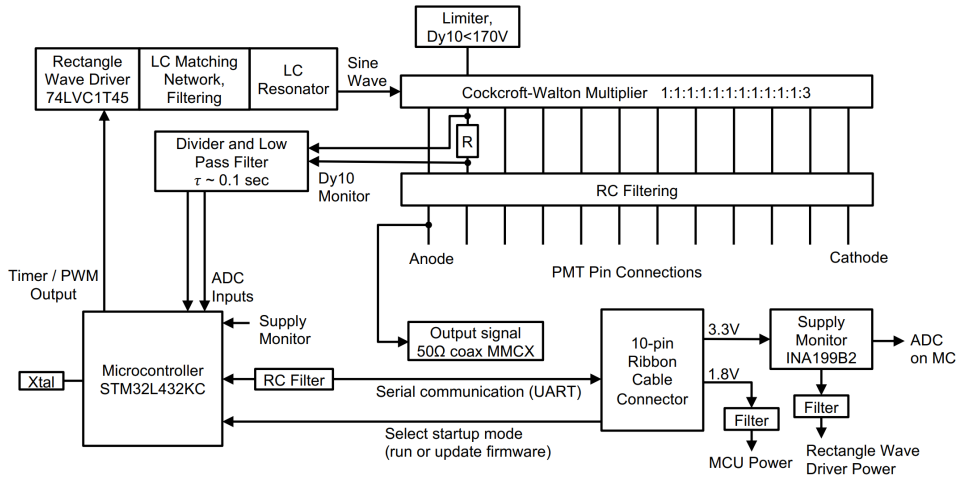


Figure 5.3: Block diagram of the μ Base. Figure from [75]. Further details on its working principles are given in the text.

To generate the high voltage and distribute it amongst the PMTs dynodes, an LC resonator is driven by a rectangular waveform with adjustable frequency and duty

cycle from the bases' micro-controller. The resulting sine wave has a peak-to-peak amplitude of 75 V to 150 V and is fed into a Cockcroft-Walton multiplier. From this multiplier, the dynode voltages are branched off in the ratio 1:1:1:1:1:1:1:1:1:3 with the cathode at negative high voltage. The μ Base is self-monitoring, measuring the voltage at the 10th dynode (Dy10) around ten times per second and adjusting the micro-controller signal in order for the voltage to reach a desired value. Due to the branching, the total voltage on the PMT equals roughly twelve times the Dy10 voltage. The micro-controller can be accessed through serial communication, allowing for monitoring and setting of desired Dy10 voltages [75]. For the μ Base in use in the P-OM, a 10-pin header is used for communication and power supply. An MMCX connector forwards the PMT's anode signal toward the data-acquisition electronics.

Because the μ Base design uses off-the-shelf components and no application-specific integrated circuits, prototype bases could be recreated for evaluating its use in the P-OM. The use of the μ Base for P-ONE is in agreement with the original designer C. Wendt. Figure 5.4 shows a μ Base from the mDOM and recreated prototypes for use in the P-OM. Six prototypes were built labeled V1, V2, and V3 in respective A and B variants.

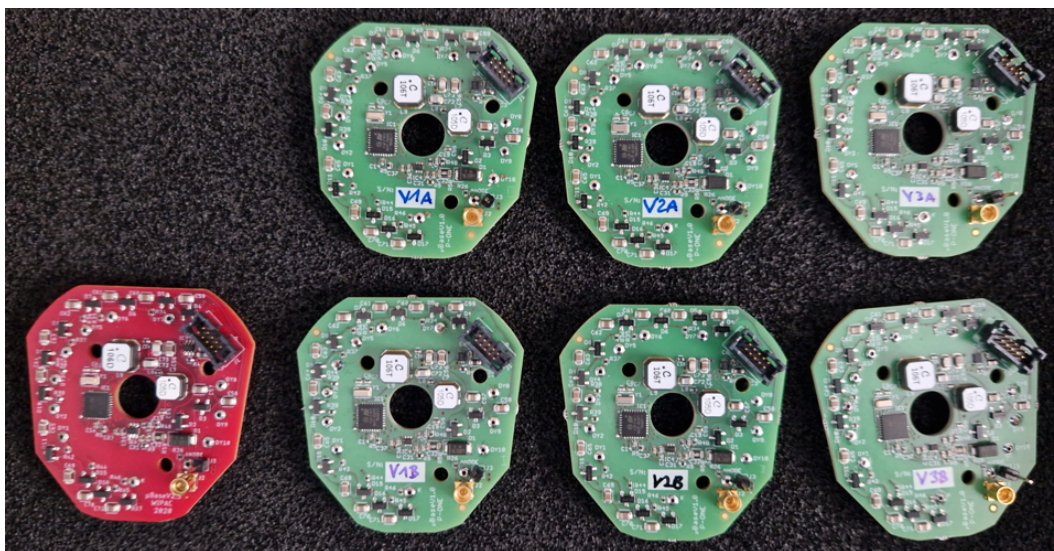


Figure 5.4: A reference μ Base for the IceCube Upgrade mDOM (red) and recreated μ Base prototypes for use in the P-OM (green).

These prototype μ Bases were tested in the OMCU with the Hamamatsu R14374 to ensure their functionality with this PMT type. Additionally, the performance between the prototype μ Bases and the mDOM reference model was investigated.

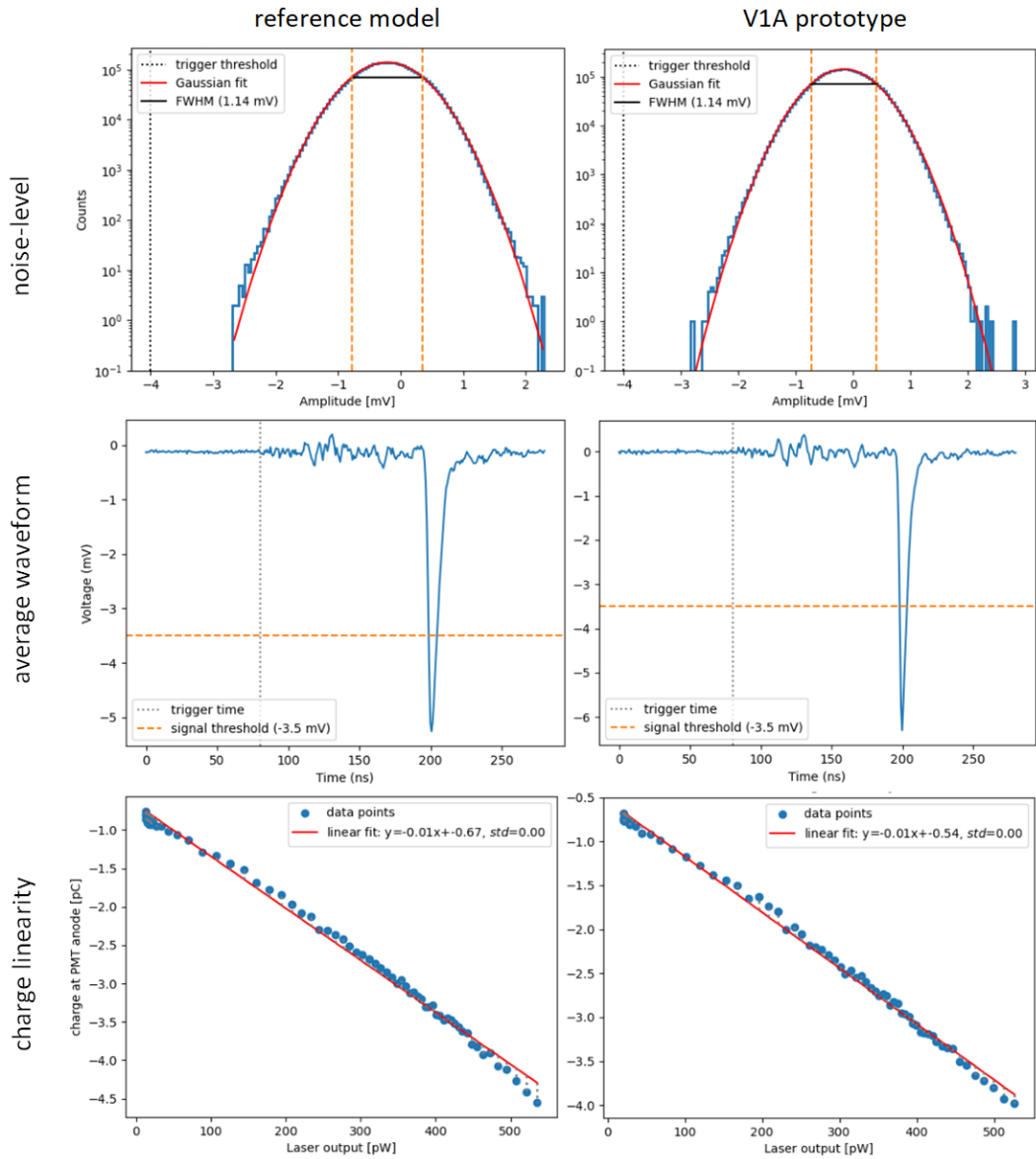


Figure 5.5: Comparison between the reference μ Base from IceCube and the V1A prototype model, measured with the OMCU. Top: the noise band on the signal without high voltage applied to the PMT. Middle: An average single-photon waveform at $Dy_{10} = 85$ V. Due to the stochastic nature of photon occupancy in the signal, only waveforms crossing a trigger threshold of -3.5 mV were considered for the average. Cross-talk between the trigger and signal channel inside the oscilloscope can be seen as jitters to the left and right of the peak. Bottom: Linear correlation between the charge deposited at the anode of the PMT and the output power of the laser.

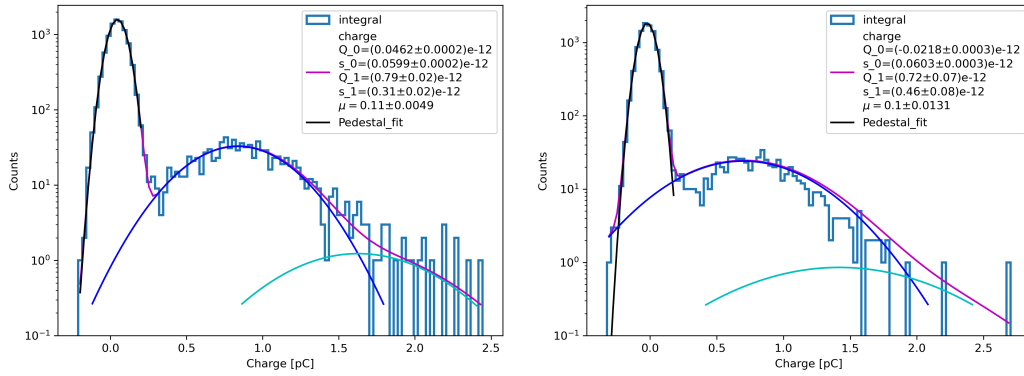


Figure 5.6: Single photon charge spectrum for the reference μ Base (left) and the V1A prototype μ Base (right). Measured with the OMCU at $Dy_{10} = 85V$. The exact gain might differ between bases due to production effects.

These tests showed similar noise levels, waveform shapes, and charge linearity curves for both models. The results also prove compatibility between the μ Base and the R14374, justifying its use in the P-OM. Figure 5.5 compares those quantities between the reference model and the prototype model V1A. While only data from the V1A prototype is shown for brevity reasons, all prototype bases show comparable performance. Additional performance plots for the other prototypes can be found in chapter A.1.

A comparison of the s.p.e charge spectrum between the μ Base models has also been conducted, showing similar results (ref. figure 5.6). The s.p.e charge spectrum was acquired by measuring a set of waveforms at an occupancy of around 10%. This means that the laser is tuned down to such a degree, so that due to the Poisson nature of photon occupation, only 10% of laser triggers result in photons being detected at the PMT. Therefore it can be assured that the "occupied" 10% of waveforms are mostly single photon signals. Correspondingly, the s.p.e spectra show a peak around zero related to unoccupied waveforms and a second peak around the s.p.e charge, containing about 10 times fewer events. A third peak can be fitted in at twice the s.p.e charge resulting from waveforms occupied by two photons. The exact position and width of the peaks are subject to the gain of the PMT, which might differ from μ Base to μ Base due to production effects. However, both models evaluated in figure 5.6 show comparable spectra with distinct and easily identifiable single-photon-peaks.

Since the results of these measurements could potentially be influenced by individual test stand performances, especially in regards to noise, the voltage at the PMT,

and light reference, a subset of the prototype μ Bases was shipped to the PMT testing facility at the RWTH Aachen [98]. This setup was built for mass-testing IceCube Upgrade PMTs and was therefore already equipped to handle the μ Bases. Compared to the OMCU, the Aachen facility uses different testing protocols specially adapted to the needs of IceCube. This includes cooling the PMTs and μ Bases to sub-zero temperatures before calibration. Results from the OMCU and the Aachen setup are, therefore, not directly comparable, especially in regard to noise and gain calibration. However, evaluating the prototype μ Base performance in two different environments puts additional confidence in their design. A comparison between the recently conducted measurements for the prototypes and pre-existing mDOM data from IceCube measurements, presented in figure 5.7, again shows good comparability between mDOM μ Bases and the prototypes developed at TUM.

The μ Base in the OMCU is powered via USB, which also serves as a communication link to the control PC. Conversion from USB to the 10-pin header of the μ Base is performed by a connector board developed at the ZTL at TUM. Because the PMT anode signal is highly susceptible to noise on the μ Base voltage supply, this connector board is additionally equipped with a series of filters, reducing noise at a rate of 1 kHz from ping-pong as part of the USB communication protocol. For additional noise reduction, a USB 2.0 cable was used between the connector board and the PC, as USB 3.0 was shown to leave more noise due to different signal rates. The connector was placed on the opposite side of the PMT in the dark box to further avoid cross-talk between the noise in the USB signal and the PMT. With those measures in place, the noise in the PMT output could be reduced to an FWHM of 1.14 mV (ref. figure 5.5), independent of which μ Base model was used.

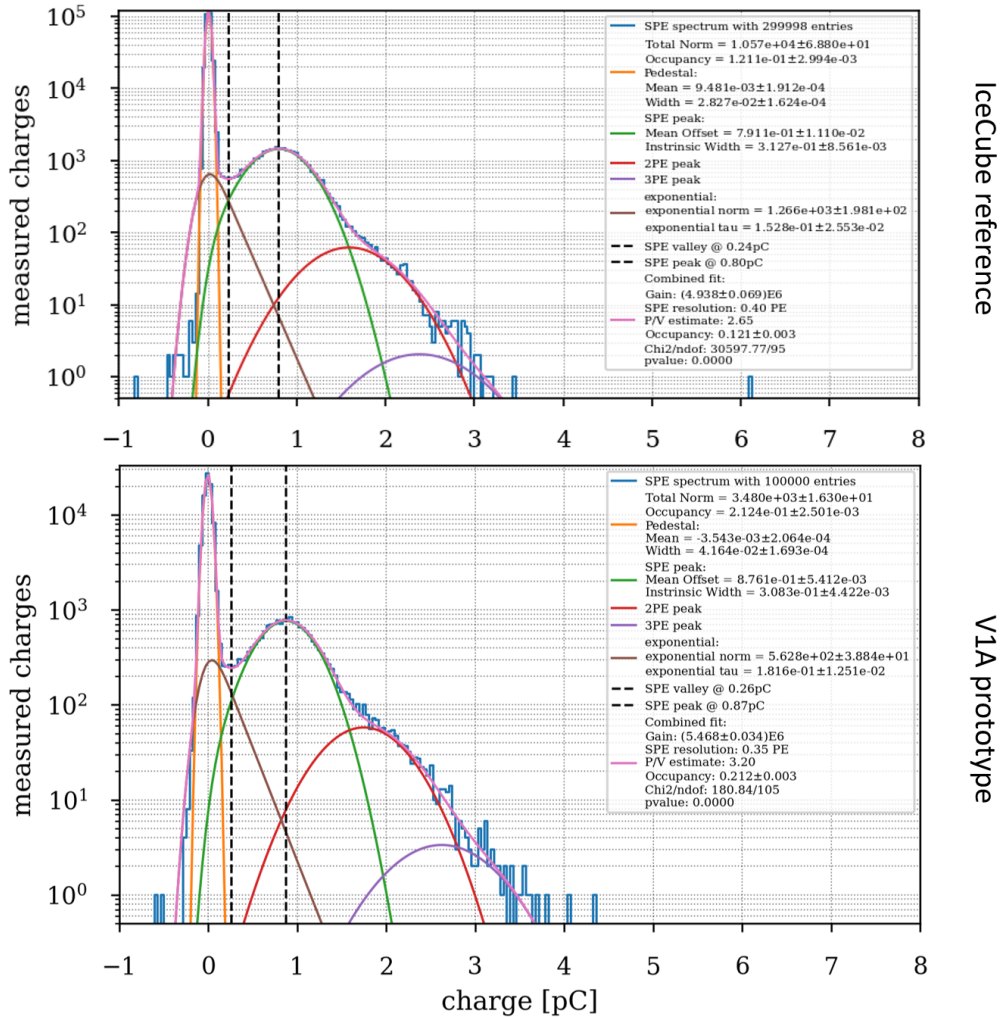


Figure 5.7: Single photon charge spectrum for a reference IceCube measurement (top) and the V1A prototype Base (bottom). Measured in the Aachen Setup. The spectrum shown here differs from figure 5.6 due to different testing protocols. Figures provided by L. Halve.

5.3 The OMCU Setup

The OMCU is centered around a light-shielded metal box that houses the current test setup, that is, PMT, μ Base, rotation stages, and optical fibers. Also present is a photodiode for reference purposes. Readout and control devices are located outside the dark box, connected to a PC that centrally runs the control software. Figures 5.8 and 5.9 show pictures and schematic drawings of the OMCU and its components, respectively. In the following, a detailed overview of each component is given.



Figure 5.8: Left: The Optical Module Calibration Unit with the dark box on the left and control and readout devices on the right. Right: The PMT, rotation stage, and photodiode together with optical fibers inside the dark box.

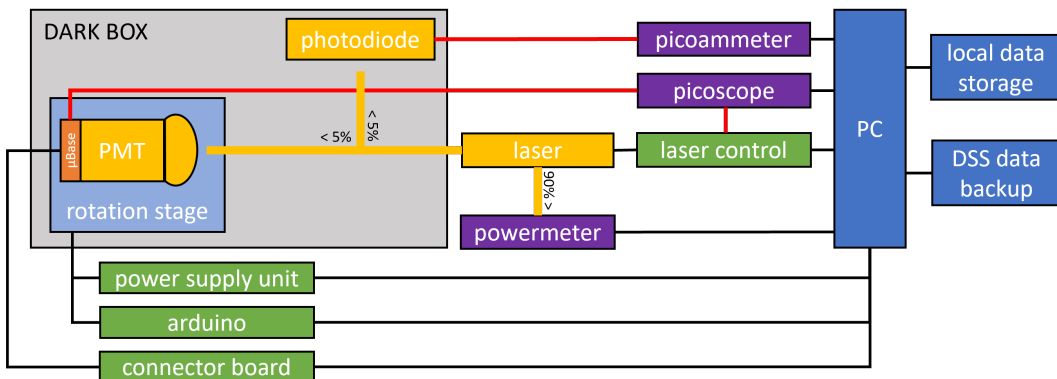


Figure 5.9: A schematic drawing of the OMCU setup components and their connections. Optical fibers are marked in yellow with the beam split indicated by percentage values. Red lines indicate coaxial cables for signal transfer, while all other cables and connections are black.

Dark Box The dark box is a galvanized and grounded steel box acting as a Faraday cage to shield the PMT from outside magnetic fields. To prevent outside light from entering the box, it has been lined with insulation and black cloth on the

interior. The holes for cables to pass through are also insulated, and the sides of the external connections and the door are covered with an additional curtain from the inside.

Rotation Stage, Power Supply and Arduino The rotation stage enables the PMT to rotate along its longitudinal axis as well as in the x-y plane of the setup. It consists of two stepper motors, one for each axis of rotation, within a 3D-printed housing. These motors are connected to the GPD-3303S Power Supply by Gwinstek. The control of the stepper motors is managed by an Arduino micro-controller board [99], which communicates with the control PC through a USB connection.

Photodiode and Picoammeter Inside the Dark Box, a photodiode as used in the POCAM [94] is connected to the laser by an optical fiber. When exposed to light, the photodiode generates a current that can be measured using the Picoammeter 6482 by Keithley. However, due to the low efficiency of the photodiode in detecting the laser wavelength and the generally low light output of the laser, no significant signals can be detected from the photodiode during the operation of the OMCU. In this context, the primary purpose of the photodiode is to monitor the effectiveness of the dark box's light seal.

Picoscope The Picoscope 6424E by Pico Technology serves the purpose of digitizing and recording the waveforms generated by the PMT. It is connected to both the signal output of the μ Base and the trigger output of the laser control unit. The Picoscope can capture waveforms with a timebase as low as 0.8 ns, utilizing an internal buffer with a capacity of 5 Gigasamples. Once a measurement is completed, the data is transferred to and stored by the control PC for further analysis.

Laser, Laser Control and Powermeter The PiL040-FC Laser by NKT Photonics is a 405 nm pulsed laser offering a maximum power output of 160 mW with a maximum pulse rate of 40 MHz. The laser can be fully controlled by the laser control unit, which is connected to the control PC. The laser output is attenuated and then split in a 90/10 ratio, with the more luminous beam being directed to the Powermeter 2936-R by Newport to monitor the laser output. The remaining fiber is then split again in a 50/50 ratio, with the fibers being directed to the PMT and photodiode, respectively.

Control PC and Data Storage The control PC running on Ubuntu 22.04 hosts a copy of the control software repository and is responsible for its execution. The PC is connected to all control and readout devices, communicating and controlling them through USB or serial ports. Connected to the PC are two 6 TB hard drives, which serve as local storage for the OMCU data. This data is synced once a day with a

Data Science Storage (DSS) Container hosted at the Leibniz-Rechenzentrum, from where it can be accessed remotely. For the data synchronization, a connection to the DSS is made through the Globus connect application which runs on the control PC.

5.4 Control Software

The Python-based control software of the OMCU underwent an overhaul for a completely object-oriented approach in the scope of this thesis. This approach resulted in a modular design that offers several advantages, including ease of maintenance and the ability to easily incorporate future upgrades to the hardware. The control software can be broadly categorized into four components: devices, data handling, testing procedures, and the main function. The following chapters provide a detailed overview of each component.

5.4.1 Devices

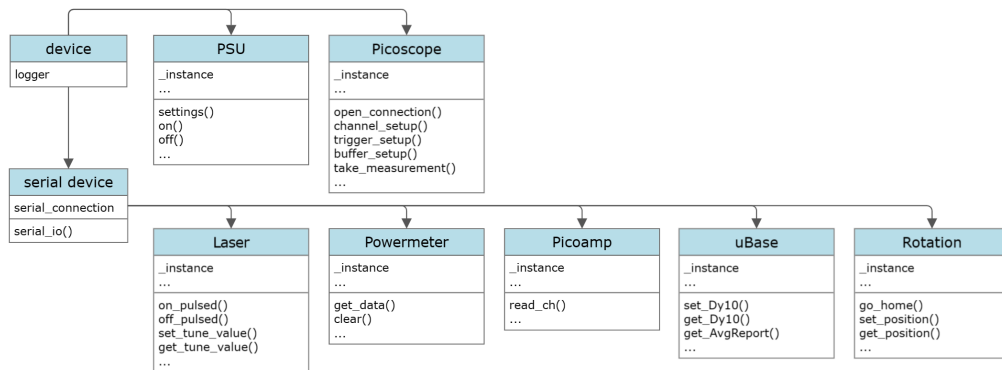


Figure 5.10: UML diagram of the device classes in the control software. For clarity, only the most relevant functions for each class are shown.

For each of the real-world devices connected to the control PC, a Python class has been implemented, offering an interface to control the respective device. A parent `device` class implements essential logging functions which all devices inherit. In principle, there are two ways of controlling remote devices through the control software: Directly on the serial level or via SDK interfaces provided by the device manufacturer. For the former, a second parent class `serial_device` was introduced, taking care of opening and handling the serial port and communicating through it.

Devices are implemented as singletons, ensuring that at any time, only one instance of the device is present in the software. Figure 5.10 shows a UML diagram of the device classes and their most important control functions.

5.4.2 Data Handling

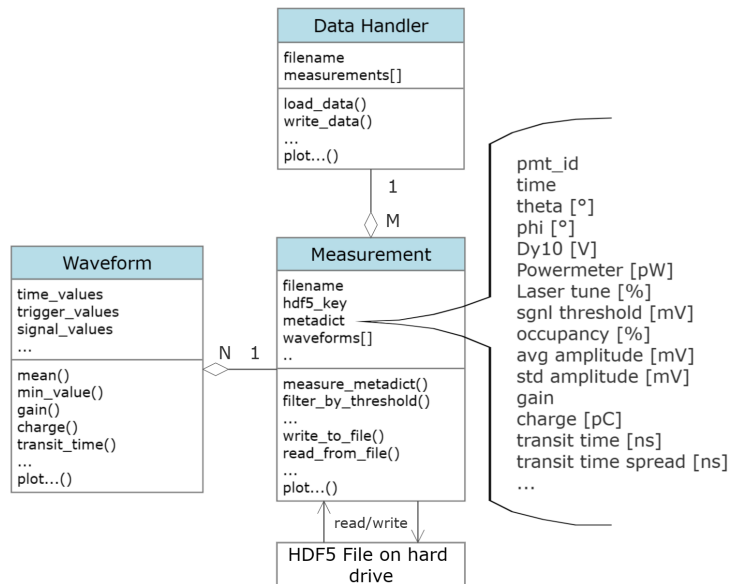


Figure 5.11: UML diagram of the classes relevant for data handling. Also shown are the contents of the **metadict** in the **Measurement** class.

The data handling was implemented in a hierarchical approach utilizing three classes: The first class, called **Waveform**, manages individual waveforms obtained from the Picoscope. It contains essential information about time, trigger, and signal and provides functions to extract waveform characteristics such as peak height, transit time, gain, or charge. Additionally, the class includes a built-in function to plot the waveform data. Next, the **Measurement** class is designed to encompass a single measurement from the Picoscope, that is, a set of waveforms that have been recorded as a block. Besides a list of waveforms, it also contains a dictionary of metadata, the **metadict**, that lists information about the measurement, such as under which angles or voltages it was recorded or which occupancy, average gain, or transit time spread was measured. These entries are either obtained from supplementary devices or calculated directly from the available waveform data. The **metadict** serves as documentation of the exact measurement circumstances and a quick reference to measured characteristics. The measurement class has read/write capabilities with

HDF5 files [100]. It is able to save or extract waveform data and `metadict`, given a filename and a key inside the file. Plotting functions are also implemented in the `Measurement` class, making it possible to directly visualize waveforms, charge spectra, or transit times. At last, the `DataHandler` class is used in the data analysis part of the main function (ref. chapter 5.4.4) to handle all measurements from a given HDF5 file, to load them correctly into the RAM and to perform desired plotting of PMT characteristics.

5.4.3 Testing Procedures

The testing procedures are the core functionality of the OMCU's control software. Here, it can be distinguished between calibration functions and actual data-taking functions.

The calibration functions determine the laser tune for a desired occupancy and the Dy10 voltage for a desired gain. This calibration is done by repeatedly measuring the calibration value and then adjusting the parameter incrementally until the desired value is reached. Several calibration modes are available. Besides modes to only calibrate one of the parameters, an iterative mode first calibrates the occupancy and then the gain. Afterward, it checks if both parameters are within a desired range and repeats the process if one of the parameters exceeds that range. Limits for ranges, step sizes, and a maximum number of repetitions can be individually set in the config file (ref. chapter 5.4.4).

The data-taking procedures are responsible for calling the calibration functions, bringing the OMCU into a desired configuration, obtaining a measurement from the Picoscope, and then writing it with its metadata on the hard drive. Schematically, those functions are structured as follows:

```
def testing_procedure():
    calibrate_setup() # arguments dependent on procedure
    for configuration in procedure:
        configure_omcu() # depending_on_procedure
        measurement = Picoscope.get_measurement()
        measurement.measure_metadict()
        measurement.filter_by_threshold(threshold)
        measurement.write_to_file(filename, key)
```

with the exact implementation depending on the procedure. So far, four procedures have been implemented in the OMCU:

- **Photocathode Scan (PCS):** calibrates occupancy and gain iteratively to de-

sired values and then takes measurements in different positions of the rotation stage.

- **HV Scan (HVS)**: calibrates the occupancy and then takes data under different Dy10 voltages.
- **Charge Linearity Scan (CLS)**: calibrates occupancy and gain iteratively, then takes measurements under different laser tunes.
- **Dark Count Scan (DCS)**: No calibration is performed for this procedure. Measurements are taken at different Dy10 values with the laser turned off.

5.4.4 Main Function

The main function combines the OMCU's functionality into one coherent system. It can be executed on the control PC through the omcu python module via `python /home/canada/munich_pmt_calibration_system/omcu`. Several command line arguments can be handed over to alter the OMCU's behavior, shown in table 5.1. Additionally, a more detailed configuration of the OMCUs behavior can be adjusted via the `config.py` file, in which parameters for data taking, waiting times, and calibration and test procedures are stored. Values in this file also control which test procedures are executed and which plotting is performed.

Executing the omcu python module first triggers some basic routines for argument parsing. Immediately after, the main function is called. It can be sequentially described as follows:

1. If not already handed over by the config file, the user has to input the PMT ID, which serves as a directory name for the data. Checks are performed that no existing data is accidentally overwritten.
2. In the newly created data directory, a logging file and a copy of the config file are placed. The config file is then checked for its validity. A warning is given if entries in the config file are missing or out of bounds.
3. Instructions on how to turn supplementary devices on and connect them correctly are given through the console. The user has to confirm that those instructions were followed and that the dark box is closed correctly.
4. Connection attempts with every device are made to verify that they are turned on and functional. If an attempt fails, an error is raised.

Short	Long	Description
-h	-help	Show a help message and exit
-o OUTPATH	-outpath OUTPATH	Path to the program output
-n PMTNAME	-pmtname PMTNAME	Name of the PMT inside the omcu
-c COOLDDOWN	-cooldown COOLDDOWN	The cooldown time in minutes to reduce noise before any measurement takes place
	-config CONFIG	Path to an alternative config file, which should be used instead of the default one
	-script SCRIPT	Executes the given script instead of the main program
	-printconfig	Prints the content of the given config file. Exits the program afterwards

Table 5.1: Command line options for the OMCU control software.

5. The setup goes into a waiting period for a specified time to reduce dark noise on the PMT.
6. If set as active by the config file, testing procedures are run in the order DCS, PCS, HVS, and CLS. Another waiting time is entered between DCS and PCS, this time with the laser turned on to give the output power time to stabilize.
7. All safety-critical devices are put into a save state. That is, the laser turned off and the voltage at the PMT turned down.
8. For each active testing procedure, a data handler loads the corresponding HDF5 file and performs the plotting as set in the config file.
9. A reminder to turn off and disconnect devices before opening the dark box is given, and the total runtime of the program is printed.

By this main function, the PMT testing process can be streamlined to a plug-and-play extent. After initial configuration, repeated tests can be performed with different PMTs, all resulting in desired waveforms and metadata saved on the hard drive. Automated plotting of PMT characteristics dependent on rotation angles, voltage, and power of the laser is performed at runtime of the main function as well.

5.5 Verification of Hamamatsu Calibration Data

As a requirement for the PMT procurement for P-ONE-1, Hamamatsu provided calibration data for all 400 delivered PMTs. These encompassed the necessary voltage for a gain of $5 \cdot 10^6$, the single photon peak-to-valley ratio at gain $5 \cdot 10^6$, the dark rate at gain $5 \cdot 10^6$, the radiant sensitivity at 1000 V and the photocathode blue sensitivity index. Additionally, for 10% of the PMTs, the transit time spread at gain $5 \cdot 10^6$ and the quantum efficiency were determined.

Out of these PMT characteristics, the voltages, s.p.e peak-to-valley-ratios, dark rates, and the transit time spreads at certain gains can be verified by the OMCU. Since only one PMT at a time can be tested in the OMCU and an entire run for a single PMT can take up to one day, the capacity for verifying the Hamamatsu data for all 400 PMTs through the OMCU was unavailable. Therefore only a randomly selected subset of 19 PMTs was tested, and the results of these measurements were compared to the data provided by Hamamatsu. Table 5.2 shows the Hamamatsu data for the subset of PMTs tested in the OMCU.

Even though only the HVS and DCS procedures described in chapter 5.4.3 were needed for verification of the Hamamatsu data, all testing procedures were run to have the data available for future analyses. For the run of measurements, the config file was set to produce the following OMCU behavior:

- The waiting period to reduce dark noise was set to 12 hours. During this period, the Dy10 voltage was set to 85 V, roughly corresponding to a gain of $5 \cdot 10^6$ for most PMTs. The time for the laser to warm up was set to 2 hours.
- The gain calibration function aimed for values between $4.95 \cdot 10^6$ and $5.05 \cdot 10^6$. The occupancy is calibrated between 9% and 10% to ensure a single photon regime. PCS and CLS calibrate iteratively, while the HVS only calibrates the occupancy.
- DCS and HVS measure the Dy10 voltages in a range from 75 V to 120 V, the limit for save PMT operation, in steps of 1 V.
- In the PCS procedure, the azimuth angle is measured in 5° steps from 0° to 100° . The polar angle is measured in 5° steps from 0° to 350° . These limits cover the full range of motion for the rotation stage.
- The CLS procedure scans the laser tune from a value of 73.0%, which is in the s.p.e regime, to 60.0% in steps of 0.2%.

Batch No.	Serial No.	Cathode Lum. Sens.	Anode Lum. Sens.	Anode Dark Current	Cathode Blue Sens.	Supply Voltage	Peak to Valley Ratio	Dark Count	TTS	QE @ 390 nm	QE @ 450 nm
		A/lm	A/lm	nA	-	V	-	1/s	ns	%	%
8	KM53552	100	367	1.9	10.9	1020	3.22	160	1.31	27.1	24.7
21	KM54349	111	302	2.0	11.2	1070	3.44	180	1.31	28.1	25.7
29	KM54415	109	184	1.0	11.2	1150	3.43	190	1.40	28.1	25.8
30	KM54710	110	368	1.2	11.4	1040	3.27	190	1.72	28.8	26.1
75	KM53548	103	367	2.3	10.8	1030	3.38	180			
104	KM54367	100	381	1.4	10.8	1020	3.76	230			
122	KM55111	113	284	1.6	11.2	1080	2.53	1560			
127	KM55116	105	249	1.3	11	1090	3.78	450			
157	KM56188	108	244	0.8	11.2	1090	3.33	300			
166	KM56208	116	231	0.7	11.4	1120	2.98	320			
188	KM56156	98	186	0.9	10.6	1110	3.18	380			
202	KM56449	115	449	3.4	11.5	1010	3.25	370			
203	KM56467	97	296	1.4	10.7	1050	2.83	350			
212	KM56478	104	267	1.1	11	1070	3.42	330			
219	KM56631	108	230	1.6	11	1100	3.34	200			
283	KM55802	109	371	1.8	11.1	1030	3.32	210			
288	KM55839	98	396	2.7	11	1000	3.77	840			
373	KM57347	114	301	1.7	11.5	1070	3.26	230			
381	KM57511	101	167	2.2	10.9	1160	2.64	750			

Table 5.2: PMT calibration data provided by Hamamatsu. Only PMTs tested in the OMCU are shown.

5.5.1 High Voltage

The voltage necessary for a gain of $5 \cdot 10^6$ was determined by fitting the voltage to gain correlation extracted from the `metadict` entries of the HVS procedure, which were calculated during testing of the respective PMT. A Polynomial fit was used as the behavior was expected to resemble equation 5.3. The gain entry of the `metadict` was calculated by first filtering the available waveforms by a threshold of -3.5 mV (around 0.6 s.p.e amplitude) to account for the stochastic occupancy of the single photon signal. In a second step, each remaining waveform was integrated with an area around its peak, and the gain per waveform was determined. The resulting gain histogram was then fitted through a Gaussian function. The Dy10 voltage was taken from the μ Base self-monitoring system and multiplied by a factor of 12 to get the full cathode-to-anode voltage. An exemplary gain fit and the voltage-to-gain correlation for the exemplary PMT KM53552 are shown in figure 5.12.

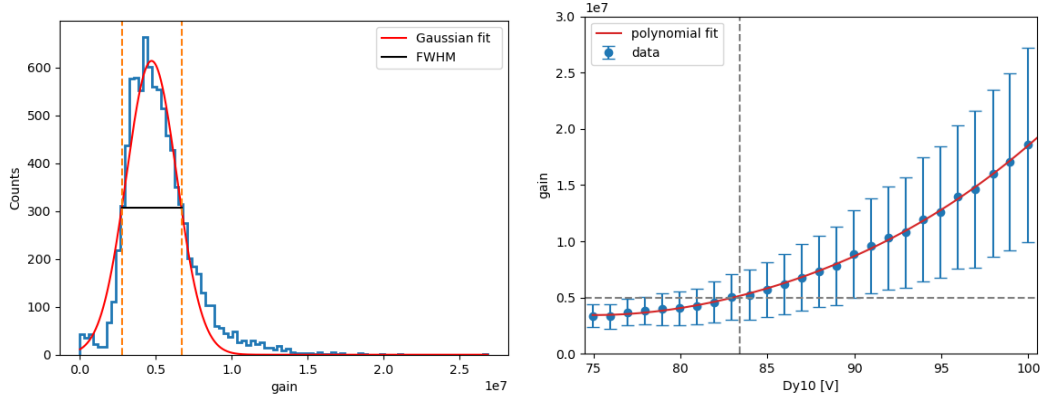


Figure 5.12: Left: Exemplary gain fit at $Dy10 = 84$ V in the KM53552 PMT. The set of waveforms was filtered by a threshold of -3.5 mV before filling the histogram. Right: The voltage to gain correlation for the KM53552 PMT.

Figure 5.13 shows the relative difference between the supply voltage stated by Hamamatsu and the supply voltage determined by the OMCU for a gain of $5 \cdot 10^6$, respectively. For the confidence interval of each PMT, a systematical error of 12 V has been assumed, given the step size of 1 V during the measurement and subsequent multiplication by 12. Additionally, an error stemming from the fit quality of the gain-to-HV curve (ref. figure 5.12) has been added.

The measurement results lie beneath the values stated by Hamamatsu, with an average offset of -28.4 V. While the exact reasons for this are still unclear, multiple sources for the offset are possible: First, the gain per measurement was obtained

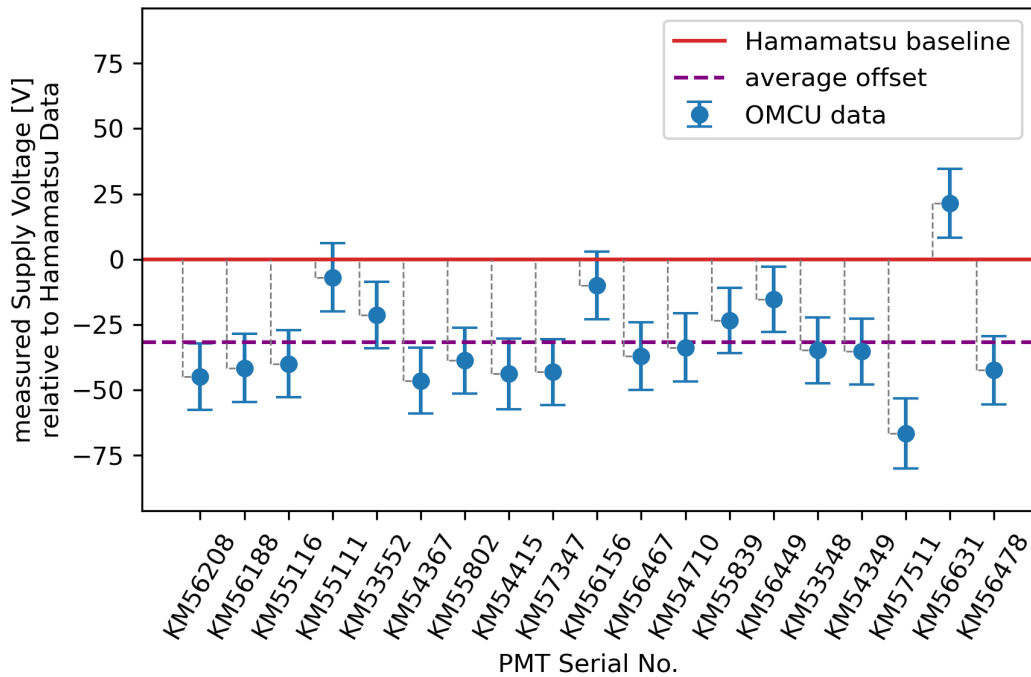


Figure 5.13: Difference in the voltage needed for a gain of $5 \cdot 10^6$ between the OMCU measurement and the data provided by Hamamatsu.

through threshold-filtering the waveforms and subsequent application of a Gaussian fit. The filtering allows for less hard drive usage by a factor of around ten by simply "throwing out" unoccupied waveforms. However, due to that cut, occupied waveforms with very low amplitude and, thereby, low gain might not be considered for the fit, so the gain-to-HV fit is shifted to lower voltages. Applying a gain fit over the entire set of waveforms could eliminate this source of error but would require a significantly higher amount of data storage space. Another source for the offset could be the different base the PMT was tested in. While Hamamatsu used a passive custom voltage divider, in the OMCU, all PMTs were tested with the reference μ Base (ref. chapter 5.2). Lastly, a heavily increased dark rate (ref. chapter 5.5.4) between Hamamatsu and OMCU data could influence the gain calibration.

5.5.2 Peak-to-Valley Ratio

For the peak-to-valley ratio, the `metadict` entry of the measurement in the HVS data, which has its `Dy10` value closest to the fitted value for a gain of $5 \cdot 10^6$, was

used. Since the peak-to-valley ratio is meant to be a metric for the "cleanness" of the signal, it was defined in the OMCU as the ratio between the peak height and the width of the noise band, both measured from the baseline of the signal. The baseline is the average signal value outside of the waveform peak, and the noise band is the standard deviation of this value. Figure 5.14 shows these values interposed on a waveform. The distribution of peak-to-valley ratios across all waveforms with a peak $\geq -3,5$ mV was then fitted with a Gaussian function.

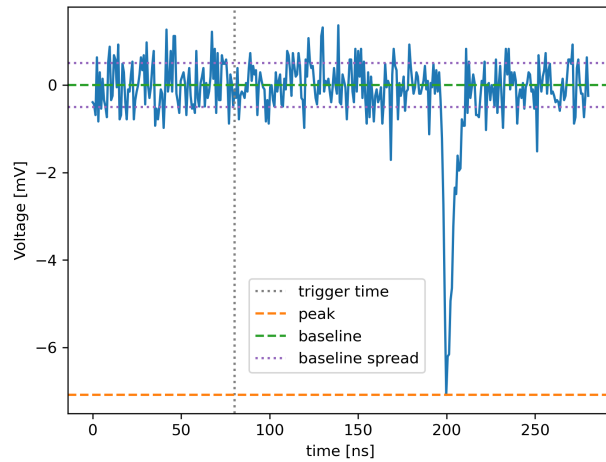


Figure 5.14: A raw waveform from the KM53552 PMT at $5 \cdot 10^6$ gain. The peak-to-valley ratio is the ratio between the height of the waveform peak and the baseline spread, both measured from the baseline.

The difference between the Hamamatsu value and the peak-to-valley ratio measured in the OMCU is shown in figure 5.15. The confidence interval originates from the standard deviation of the Gaussian fit on the peak-to-valley ratios for all waveforms.

On average, the measured peak-to-valley ratio exceeds the Hamamatsu value by more than 12. Given that the peak-to-valley ratios given by Hamamatsu are typically in the range of 2 to 4, this is a significant increase by a factor of around 3 to 6. This offset indicates either a much cleaner signal in the OMCU compared to the Hamamatsu measurement or a systematic difference in the definition of the peak-to-valley ratio. It is unclear, how exactly Hamamatsu defines the ratio, as the technical specification for the procurement process only demanded a ratio of ≥ 2 without further details, and Hamamatsu provided the data without details on their testing procedures. Should Hamamatsu have chosen a different definition, like the ratio between the waveform peak and the most significant peak besides the waveform peak, the actual values could align much closer.

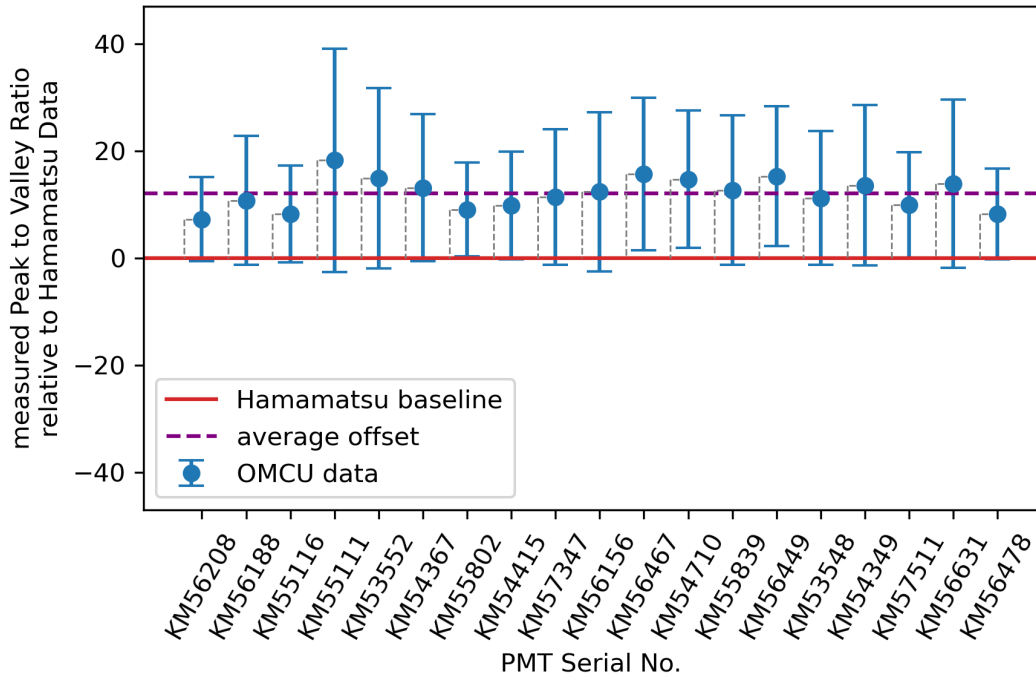


Figure 5.15: Difference in the peak to valley ratio at a gain of $5 \cdot 10^6$ between the OMCU measurement and the data provided by Hamamatsu.

5.5.3 Transit Time Spread

As described in chapter 5.1, the transit time spread is the FWHM in a transit time histogram. As transit time in the OMCU, the time between the laser trigger and the waveform peak was taken. For the comparison, the TTS of the measurement with the Dy10 voltage closest to the fitted value for a gain of $5 \cdot 10^6$ was used. Figure 5.16 shows an exemplary transit time histogram for the KM53552 PMT at this Dy10 voltage.

Figure 5.17 shows the relative differences in transit time spreads between the OMCU and Hamamatsu measurements at a $5 \cdot 10^6$ gain. Because the TTS was only evaluated by Hamamatsu for 10% of the 400 PMTs, only 4 PMTs out of the random batch of 19 had Hamamatsu data available. The TTS in the OMCU measurements lies on average 0.65 ns above the value measured by Hamamatsu, which can be attributed to the resolution of the Picoscope of 0.8 ns as well as an uncertainty in the laser time response of < 45 ps, which together build the confidence interval for the comparison. All PMTs show agreement with the Hamamatsu data within this interval.

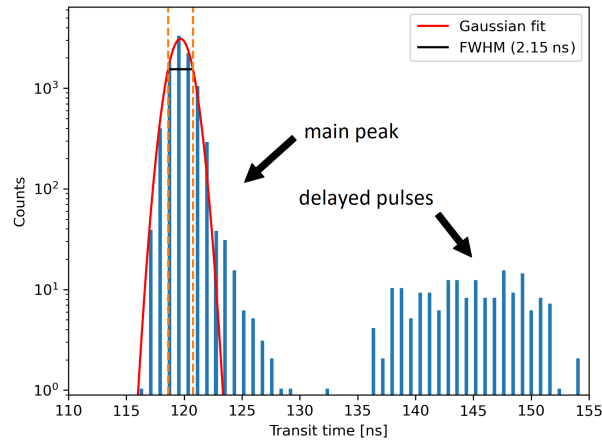


Figure 5.16: Exemplary transit time histogram for the KM53552 PMT at a $5 \cdot 10^6$ gain. Transit times are spaced in 0.8 ns intervals due to the resolution of the Pico-scope. Delayed pulses are visible at transit times between 135 ns and 155 ns. All registered pulses, delayed or not, contributed to the transit time fit.

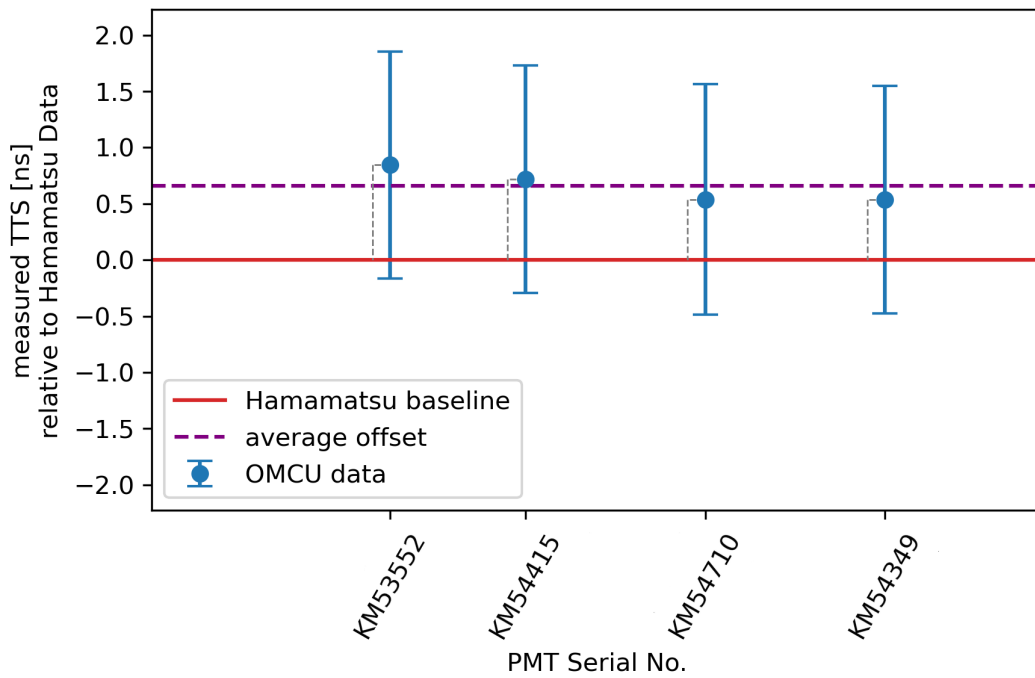


Figure 5.17: Difference in the transit time spread at a gain of $5 \cdot 10^6$ between the OMCU measurement and the data provided by Hamamatsu.

5.5.4 Dark Rate

A single dark count in the DCS procedure of the OMCU is defined as any number of consecutive waveform samples exceeding a certain threshold, in this case, -3.5 mV. While all other scans capture multiple waveforms with 350 samples each around a trigger event, the DCS procedure captures consecutive 10^8 samples at a 3.6 ns timebase, allowing to continuously count dark counts and determine the dark rate. This dark rate is written to the `metadict` during the OMCU run and saved together with the raw samples to the hard drive.

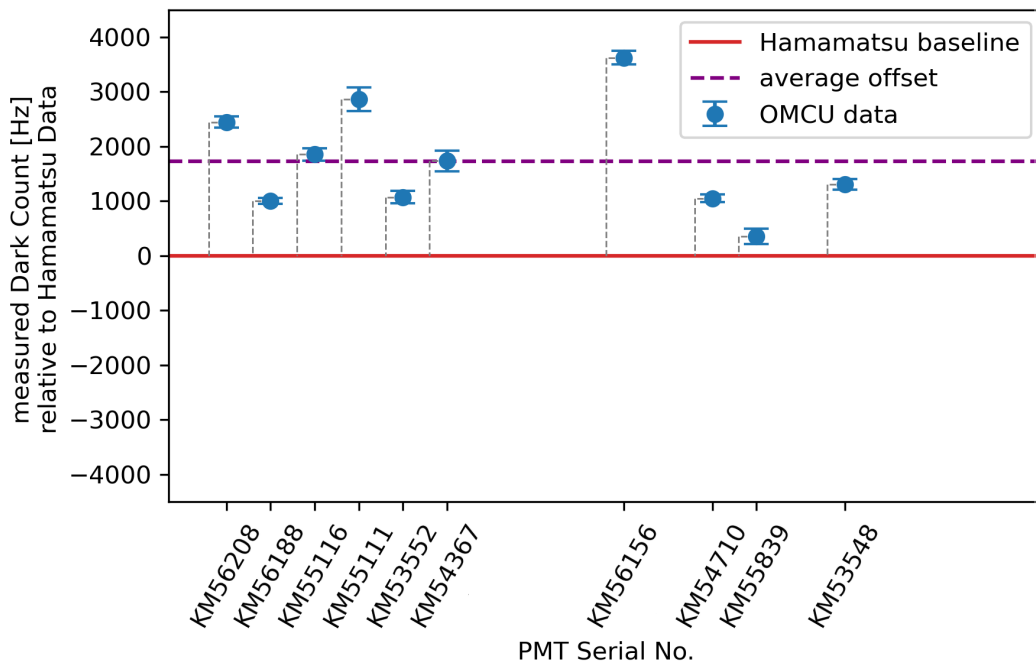


Figure 5.18: Difference in the dark rate at a gain of $5 \cdot 10^6$ between the OMCU measurement and the data provided by Hamamatsu. In both the OMCU and Hamamatsu measurements, the PMT was sitting in the dark for 12 hours before data was taken.

Figure 5.18 shows the difference between the dark rate measured by the OMCU and as provided by Hamamatsu. A bug in the software at the time of measurement rendered data for some PMTs unusable, therefore, only a subset of the PMTs tested in the OMCU could be evaluated for their dark rate. The dark rate measurements by the OMCU are visibly offset by around 1900 Hz on average compared to the Hamamatsu baseline. This results in a dark rate approximately one order of magnitude higher than the rates provided by Hamamatsu. The reasons for this can be numer-

ous. The easiest to explain is a different threshold for counts in the Hamamatsu measurement. However, it is questionable if a different threshold could explain an increase of one order of magnitude, primarily since the threshold in the OMCU of -3.5 mV has also been used to identify occupied waveforms in the first place. More likely is a contamination of the OMCU, either through light by faulty insulation or by radioactive particles which accumulated in dust, the insulation, or the black cloth inside the dark box. Against this speaks that the light level inside the dark box was constantly monitored by the reference photodiode, and all components inside the box were checked for radioactive contamination before installation. However, a similar effect of increased dark rate has been seen in different measurements in the neighboring laboratory, utilizing the same cloth as the OMCU.

5.5.5 Summary on the Data Verification

Concerning the dark rate, an investigation into the origin of the difference in rate should be performed. Currently, the Hamamatsu data does not align with the OMCU measurements, indicating a source for dark counts inside the OMCU.

While the peak-to-valley ratio stated by Hamamatsu could not be directly verified, most likely due to a different yet unknown definition of that ratio on the side of Hamamatsu, the values stated for voltage and transit time spread could be roughly confirmed by the OMCU, at least within in the range of systematic uncertainties. This puts both confidence in the validity of the Hamamatsu data and in the OMCU as a functional test setup regarding the determination of those PMT characteristics.

With the elimination of the previously discussed systematic uncertainties, namely an improved way of gain fitting, a higher time resolution of the signal, and a calibration of the laser, especially in regards to photon flight time, the accuracy of the OMCU can be further improved for future PMT and Optical Module evaluations for the P-ONE project.

5.6 Upgrade Plans for the OMCU

As the development of the Optical Module for P-ONE-1 progresses toward the first functional prototype, plans are underway to upgrade the OMCU to accommodate an entire hemisphere of the module. These upgrades are intended to enable a rapid calibration of the complete module and provide insights into its acceptance under different wavelengths and angles of incoming light. To achieve these objectives, three critical changes to the setup are being considered:

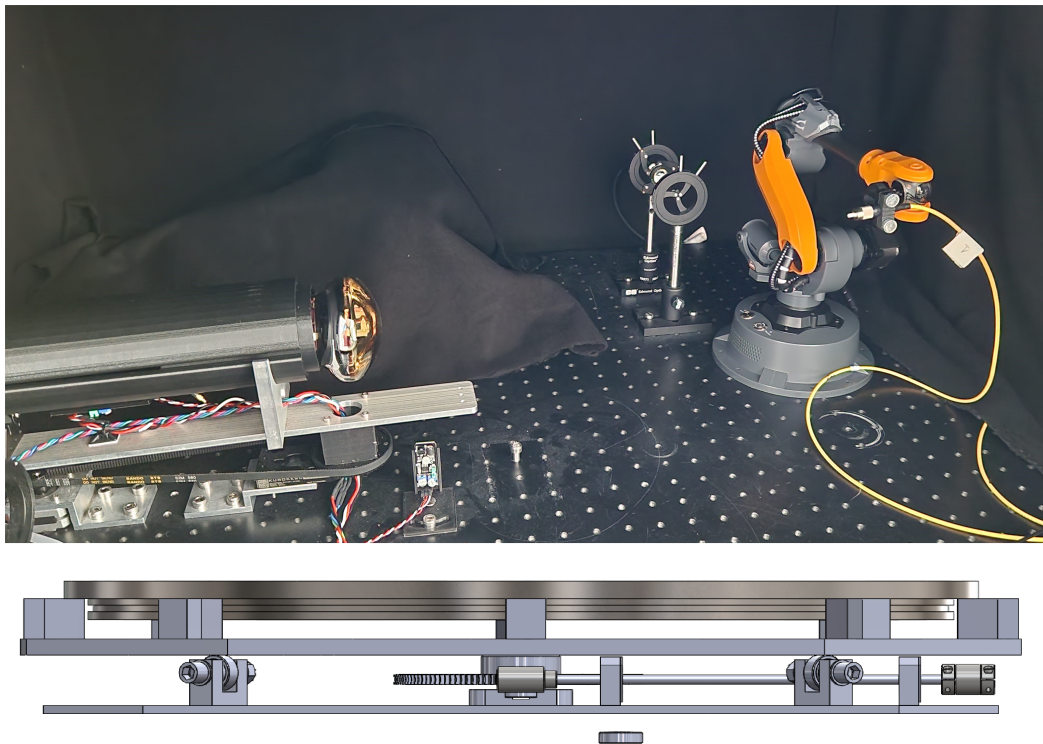


Figure 5.19: Top: The WLkata Mirobot holding the optical fiber pointed towards a PMT. Bottom: Side view CAD drawing of a rotation stage for a full P-OM hemisphere (design by L. Papp).

A **robot arm** holding the optical fiber together with a rotation stage for an entire hemisphere is planned to probe the angular acceptance of the module from various positions. The WLkata Mirobot is currently being integrated into the setup, while a rotation stage for the hemisphere has been designed and developed and will soon be integrated. Both devices are shown in figure 5.19. Those two devices are planned to fulfill a similar function as the current single-PMT rotation stage, with the option to easily switch between the current rotation stage and the new rotation stage and robot combination to allow for flexible single-PMT and hemisphere testing.

A planned **light source** together with a diffusor at the ceiling of the dark box will allow for quick calibration of all PMTs inside the hemisphere at once. As a light source, multiple LEDs at different wavelengths are planned.

A **reference instrument** with a known spectral response is planned to be placed at the other fiber output, where currently the unused photodiode sits. This instrument,

either a PMT or a calibrated, highly sensitive photodiode, can be used to determine the quantum efficiency of the test PMTs. For this, the light source must also be exchanged to allow measurements at different wavelengths.

In conclusion, the proposed upgrades for the OMCU are hoped to facilitate module testing to a similar level as the currently ongoing individual PMT tests. The integration of a robot arm with a rotation stage, a light source with a diffuser, and a reference instrument will enable comprehensive testing and efficient calibration of the complete module, providing valuable insights into its performance under various conditions.

Chapter 6

A Geant4 Framework for the P-ONE Optical Module

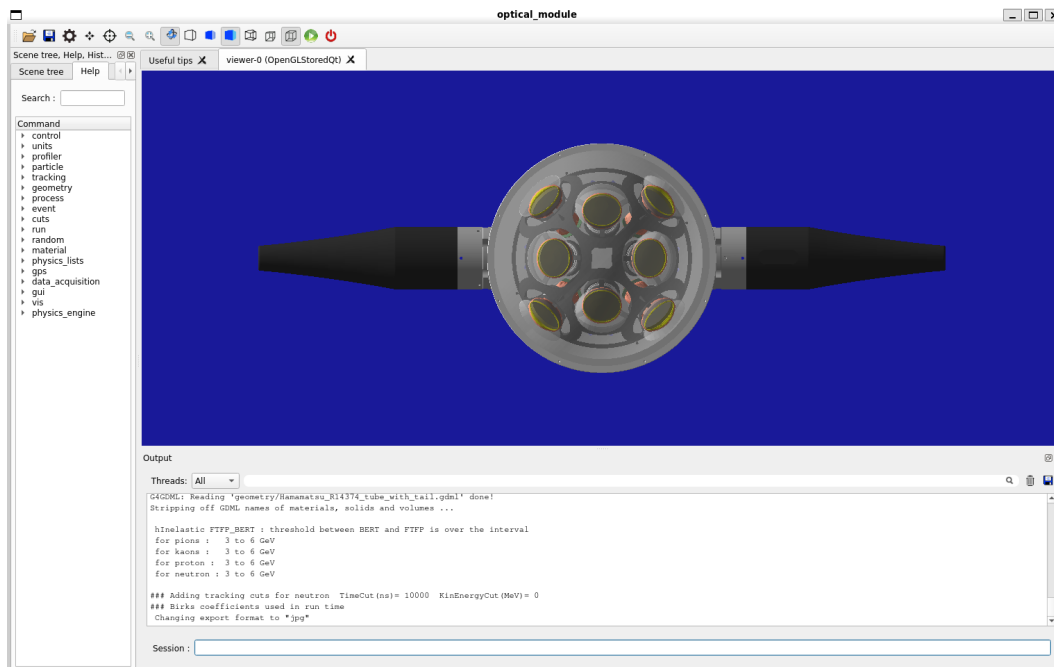


Figure 6.1: The P-OM Geant4 Framework's GUI utilizing the OGL visualizer of Geant4. From here, the simulation can be controlled via macro commands.

This chapter presents the development of a simulation framework for the Optical Module (P-OM) in conjunction with the ongoing development of the P-ONE-1 project. The framework is based on the Monte Carlo simulation toolkit Geant4 and

serves the purpose of predicting and validating the behavior of the P-OMs optical components, as well as testing and verifying design choices through a digital twin.

The framework was designed with two main objectives in mind: First, obtaining an exact representation of the P-OM geometry and optical parameters for the most accurate results. Second, ensuring modularity to facilitate easy implementation of design changes in the P-OM as well as extensions to the simulation itself. For this, the simulation control was entirely outsourced from the source code into macro files. Additionally, a novel approach was employed to construct the geometry, utilizing a hybrid process that combines manual (source code-based) construction and the import of converted CAD geometries.

This chapter provides insight into the framework's design and implementation. Furthermore, an evaluation of the obtained Monte Carlo data is presented, shedding light on the performance of the P-OM under different design alterations.

6.1 The Geant4 Toolkit

Geant4 (**G**eometry **a**nd **T**racking) [101, 102] is a C++-based toolkit for the simulation of the passage of particles through matter. It is developed and maintained by the international Geant4 collaboration. Geant4 includes a wide variety of features in geometry, tracking, detector response, visualization, and selection of the underlying physics processes. Due to its versatility and modular structure, it is used by a number of different research projects worldwide in areas like high-energy physics, nuclear experiments, medicine, and space sciences [102].

Users are able to specify their own simulation geometry, including material and surface properties. The base element of any Geant4 geometry is the `G4VSolid`, which is a purely geometrical object without other properties. These solids can be simple volumes like trapezoids, ellipsoids, general polygons, or more complex tessellated objects defined by facets. Solids can be combined using Boolean operations, allowing for the creation of new, more complex shapes. Solids are then encapsulated in a `G4LogicalVolume`, adding material and, if needed, other properties like electric fields and then placed via a `G4PhysicalVolume` inside Geant4s world environment.

Materials can be either extracted from the Geant4 material database [103] or built manually by specifying different atoms and isotopes by their atomic charge and mass and then building molecules and compounds from there. Optical and other properties of those materials can be set in a so-called `G4MaterialPropertiesTable`, which allows for energy-dependent parameter storage. To specify the optical parameters of

surfaces, either a `G4LogicalSkinSurface` is "wrapped" around a logical volume, or a `G4LogicalBorderSurface` is placed on the border of two physical volumes. These surfaces come with their own property tables.

In addition, the user has to specify the particles and physics processes that take part in the simulation as well as specify physical parameters and even custom physical processes if needed. This is done with a so-called Physics List, which registers the necessary particles and processes. For purely optical simulations, Geant4s default Physics List FTFP BERT [104] with the additional `G4OpticalPhysics` registered, provides optical photons and charged particles for production of Cherenkov light and, in addition, the pre-implemented processes of Cherenkov radiation, optical absorption, optical boundary processes, Rayleigh scattering, Mie scattering and wavelength shifting. Parameters for those processes are handed over via the material and surface properties mentioned above.

Controlling a Geant4 simulation is possible via so-called macro commands. These commands can be provided at run time either through a console or specified in a macro file which will be read in by the simulation. This allows for changes to the simulation parameters without the need to recompile between runs. Geant4 offers a wide variety of pre-implemented commands covering, among others, primary particle behavior, tracking behavior, physical parameters, active physical processes, and visualization. The user can add their own commands through a `G4UI messenger`, opening up control of user-specific areas of the simulation, such as geometry and data acquisition.

6.2 Implementation of the P-OM Geometry

In order to investigate the impact of photon scattering within the module and accurately estimate the module's angular acceptance, it is crucial to represent the complex geometry of the P-OM accurately. Because of that, constructing the P-OM geometry in source code using Geant4's basic solids was deemed impractical, as this would always lead to geometrical simplifications. Besides that, any source-code-based modeling would have to be redone for every design change that is made. Instead, an alternative approach was adopted, involving the import of the existing CAD geometry of the P-OM through conversion into the geometry description markup language (GDML) [105]. Nevertheless, optical simulations require an optically functional PMT with an accurate implementation of its photocathode and reflector, which the existing CAD drawings do not provide. Therefore, a hybrid approach to the geometry implementation was chosen. The PMT and the gel pad were

manually modeled in source code and subsequently incorporated into the imported P-OM geometry.

6.2.1 Construction of the PMT and Gel Pad Unit

Starting point for the PMT implementation into the simulation Framework is a CAD drawing of the Hamamatsu R14374, which is used in the full P-OM CAD drawing. The model's dimensions are based on the data-sheet provided by Hamamatsu [62]. As this data-sheet only provides the outside dimensions, and Hamamatsu does not disclose dimensions for components inside the PMT, a best guess estimate on the dimensions of the photocathode, vacuum chamber, and dynode structure had to be made, followed by a visual crosscheck between the frameworks visualizer and a real R14374 (ref. figure 6.2).

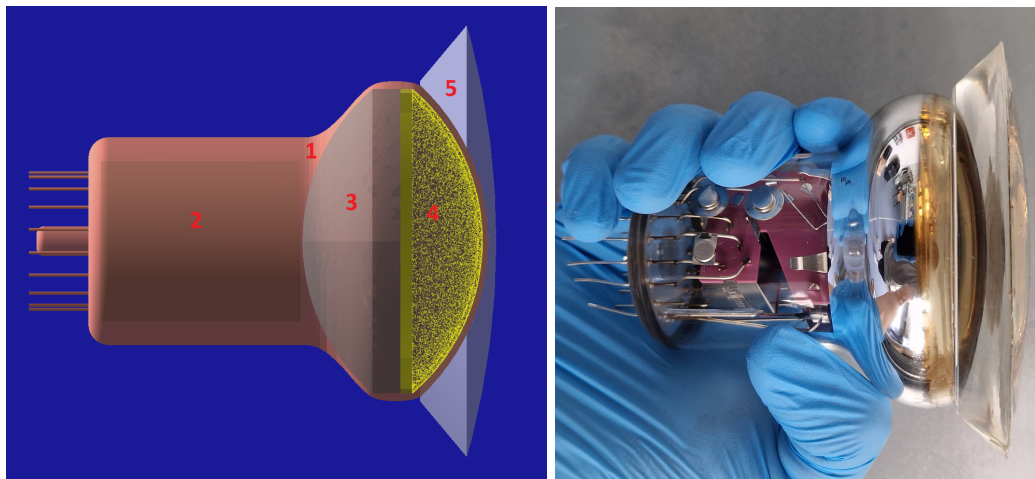


Figure 6.2: Left: The PMT and gel pad unit in Geant4. The components are the PMT glass (1), a plastic light absorber to represent the dynode structure (2), the vacuum chamber with the reflector (3) at the bottom and the photocathode (4) at the top, and the gel pad (5). Right: A picture of an R14374 with gel pad.

The R14374 CAD geometry was imported into the simulation (ref. chapter 6.2.2) and given glass properties to serve as the PMTs glass housing (1). To accurately model the vacuum chamber, it was split up into two spherical parts cut off in opposite directions, connected by a cylindrical part. A good visual fit with the real PMT geometry was found with a cylinder of radius 38 mm and height 10 mm, and spheres of radius 50 mm. The vacuum chamber was placed inside the PMT glass to allow for a 1 mm glass thickness on the photocathode side. In the top sphere of the vacuum

chamber, a photocathode of 1 mm thickness (4) was placed directly at the edge of the glass. The photocathode is extended by a 3 mm long and 1 mm thick tube down the vacuum cylinder to best resemble the real-life curvature. On the other side of the vacuum chamber, a reflective surface (3) is placed on the border between the glass and the vacuum inside the chamber. As the PMT is only modeled up to the photon absorption, an explicit implementation of the dynode structure was not needed. To still simulate the absorption of photons hitting the structure, a plastic absorber (2) of 50 mm height and 20 mm radius was placed directly behind the vacuum chamber.

Since the conversion of the P-OMs CAD geometry is based on tessellation, unwanted gaps and overlaps in the optical coupling between PMT and hemisphere glass can occur. To avoid those, the gel pad (5) was also modeled by hand to resemble the geometry used in the P-OM but larger than its real-life counterpart on the sides in contact with PMT and the hemisphere glass. During placement, these extra parts are "cut" through a Boolean operation between the gel pad solid and the PMT and glass solids in place. This assembly process is described in detail in chapter 6.2.3.

Keeping the flexibility of the framework in mind, multiple geometry parameters, such as the thickness of the photocathode and its position, can be adjusted through macro commands without the need to edit source code. A full list of macro commands as well as optical parameters for all materials and surfaces in use, can be found in chapter 6.3.

6.2.2 Conversion of CAD Geometries to GDML

Geant4 offers to import and export its simulation geometries through the GDML language [105]. GDML is an XML-based language offering a persistent format to describe detector geometries, including geometry trees, shapes, object placements, and material information. While the import of GDML files into Geant4 is a straightforward task, the conversion of the P-OMs CAD drawings into GDML requires some non-trivial extra steps.

Fundamentally, GDML uses the same structures to describe the detector geometry as the source code of a Geant4-based application. Solids can either consist of elemental shapes or more complex representations through tessellated facets. These solids are then joined together with material properties to form logical volumes, which are then placed in the simulation world as physical volumes. Although GDML converters based on assigning elemental solids to CAD volumes exist [106], the conversion method was unfeasible for the P-OM, as its complex geometry causes imprecise conversions at best and complete conversion errors at worst. Instead, an approach utilizing a tessellation of the geometry was chosen. Converters using this approach

exist as well [107–109]. However, none of them were directly usable as they were either outdated and not maintained or not freely available.

For this reason, the open source CAD to GDML converter GUIMesh [107], developed by M. Pinto, was forked and updated for the needs of converting the P-OM geometry. GUIMesh accesses the FreeCAD [110] Python API to read a CAD file in the STEP format and tessellate all objects within this file. In the second step, the tessellated objects are written in separate GDML files, which are then connected through a "mother" GDML file containing the world volume and importing objects from their respective files. Besides bug fixes, the forked version of GUIMesh implemented an update to Python 3 as well as additional features needed for the P-OM geometry conversion, such as offsetting the geometry origin and ways to automatically disable the conversion of unwanted objects in the STEP file remnant from SolidWorks, in which the CAD drawings were created in.

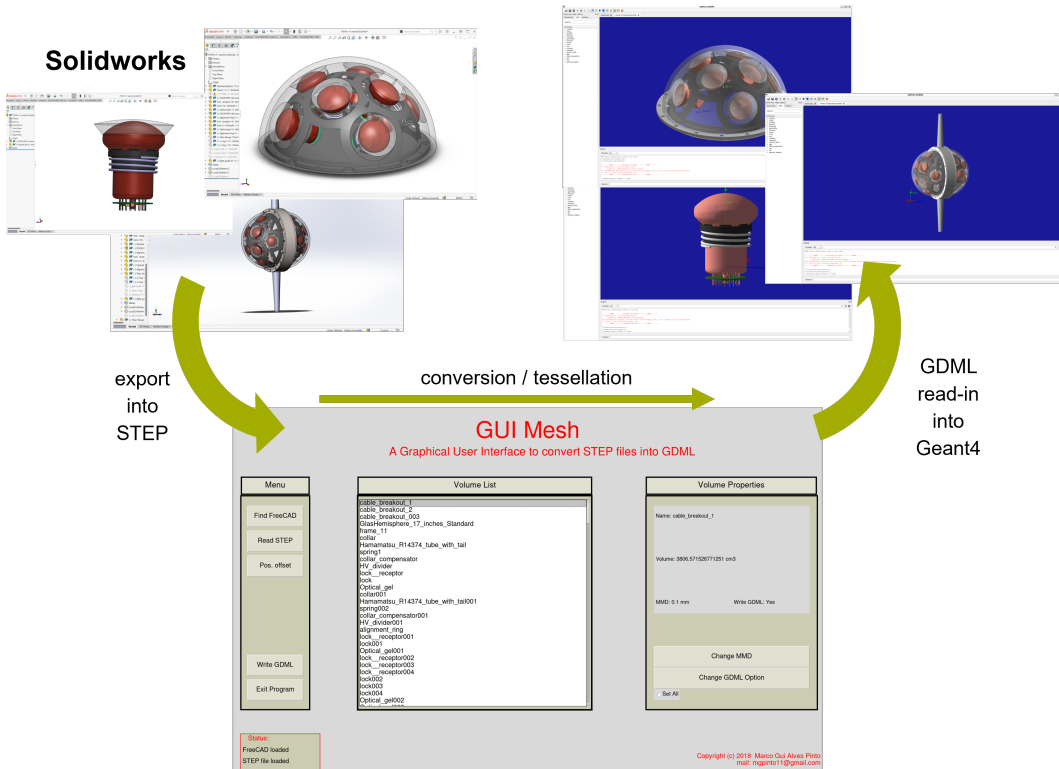


Figure 6.3: Schematic representation of the GDML conversion process. The Solidworks geometry is prepared and exported to STEP. This file is then read in and converted to GDML by GUIMesh. The GDML file can be imported into Geant4.

Starting with the CAD drawing in SolidWorks, the entire conversion process using the forked version of GUIMesh can be described as follows:

1. Dissolving of patterns and sub-assemblies in SolidWorks, as this causes unwanted double tessellation of both the part and its assembly/pattern.
2. Export of the SolidWorks geometry into the STEP format (via the SolidWorks `export` function).
3. Read in of the STEP file into GUIMesh.
4. Settings in GUIMesh (tessellation precision, which objects to tessellate, coordinate offsets, etc.).
5. Export of the geometry into GDML.
6. Read in of the "mother" geometry file into the P-OM simulation framework.

The framework repository comes with converted geometries for a hemisphere and a full Optical Module based on the Version 11 iterations of the SolidWorks CAD drawings. In these files, several smaller parts have been omitted for performance reasons, as they have little to no influence on the optical performance of the P-OM. These include o-rings, alignment rings, and lock receptors. PMTs and gel pads have been removed as well, as they are added through the process described in chapters 6.2.1 and 6.2.3. For the full P-OM geometry, the hole in the titanium ring was closed to avoid photons traversing from one hemisphere into the other, just like it will be the case in the real P-OM. The P-OM geometry also comes in an alternative version with closed holes in the mounting frame. Which geometry is imported can be selected via a macro command (ref. chapter 6.3). It was deemed the best solution to not assign material properties directly in GDML but to only import the geometry information and assign materials later at simulation run time.

6.2.3 Assembly of PMT, Gel Pad and GDML Geometry in Geant4

With the PMT, the gel pad, and the GDML geometry available, the final Optical Module needs to be constructed through the Geant4 source code. The first step after importing the GDML files via the `G4GDMLParser` is the assignment of material and surface properties to the imported geometry. These properties are stored in a separate file and read during the initialization of the program. Next, the PMTs and gel pads are placed in positions that were defined by the user via macro commands. While the PMT can be placed straightforwardly, the gel pad solid is altered before placement to cut off parts that overlap with the PMT and the

glass hemisphere. For this, the relative position between those parts is calculated, and a `G4SubtractionSolid` is created, handing over the respective solids and their relative positions.

Depending on the user settings, additional steps take place during this assembly process. If the user sets the `/geometry/gdml/submerge` command, the air volume outside of the Optical Module is replaced with water. While the rest of the assembly process is completely independent of the exact geometry definitions in GDML, this step requires some custom code for each geometry to correctly distinguish between the inside and outside of the P-OM. This is especially critical in the case of the open hemisphere provided with the framework. For all geometries that come with the framework repository, this code is implemented.

6.3 Simulation Parameters

Besides the geometry information via GDML, a variety of additional parameters are set in the simulation. In this section, the optical parameters used in the simulation are presented, followed by a description of the macro commands used to alter additional simulation parameters.

6.3.1 Optical Parameters

The optical parameters for every material and surface in use are stored in the `optical_properties.cfg` file and read in and assigned during initialization of the simulation.

material	refraction index	absorption length	source
vacuum	1.0	1000 km	- / -
air	1.0	1000 km	- / -
water	1.345 – 1.370	5 – 27 m	[111] / [66]
glass	1.472	74.867 – 131.456 mm	[112] / [113]
gel	1.404	1000 mm	[114] / -
plastic	1.0	0.01 mm	- / -
titanium	1.0	0.01 mm	- / -
photocathode	1.4	3.47 mm	- / [62]

Table 6.1: Optical parameters for materials as used in the P-OM framework.

The parameters for materials are given in table 6.1 and figure 6.4. Literature values

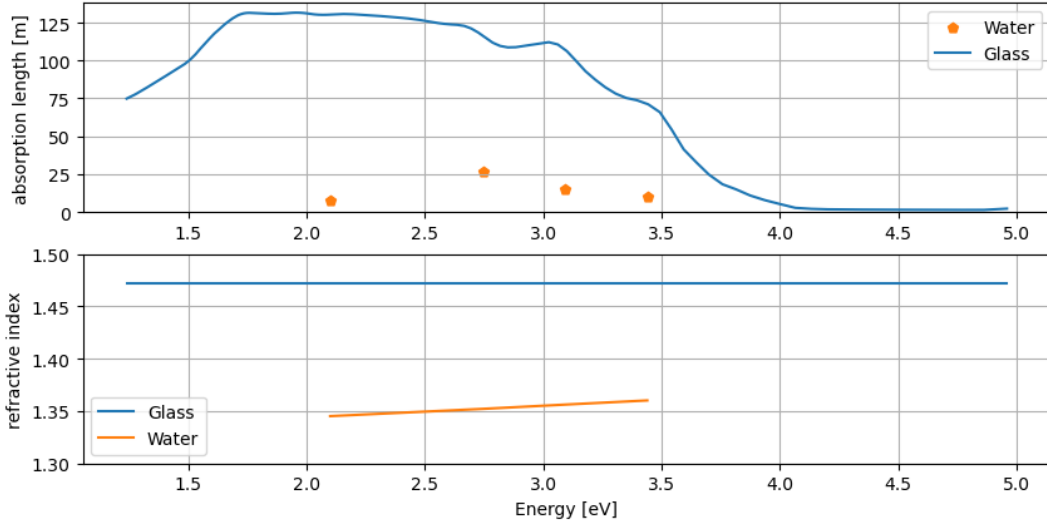


Figure 6.4: Optical properties for saltwater and borosilicate glass dependent on energy, as used in the P-OM framework.

for the refraction index of highly pressurized salt water [111] were available. For the absorption length of water, STRAW data [66] was interpolated. The refraction indices for borosilicate glass [112] and gel [114] were provided by their respective manufacturers, while for the absorption length of borosilicate glass, a manufacturer for a similar glass provided data [113]. The properties of plastic and titanium were deemed unimportant since these materials are covered by the corresponding material surfaces. As the surface is responsible for handling reflective properties and no photon propagation is expected through these materials, the optical properties were arbitrarily assigned with arbitrarily low absorption lengths. The photocathode absorption length was calculated from the R14374 data-sheet [62]. Hamamatsu states a quantum efficiency of around 27% for a photon going through the photocathode. As the thickness of the photocathode is not publicly disclosed, a 1 mm thickness was assumed, resulting in a 3.47 mm absorption length. The refraction index for the photocathode was placed as a best guess estimate to closely align with the values for glass and gel, as no public data is available.

surface	reflection	absorption	sigma_alpha
plastic	0.1	0.9	0.7
titanium	0.5	0.5	0.2
reflector	0.9	0.1	-

Table 6.2: Optical parameters for surfaces as used in the P-OM framework.

Table 6.2 lists the surface parameters used in the simulation. Geant4s simulation of an optical boundary process requires parameters based on the reflective model in use. In general, values for reflectivity and absorption probabilities need to be provided, from which the transmission probability is calculated via

$$\text{transmission} = 1 - \text{reflection} + \text{absorption}.$$

In case an unpolished surface is simulated, an additional parameter for the surface roughness needs to be provided so that the reflection angle of the light can be sampled correctly. This is the so-called "sigma_alpha" parameter [115]. This parameter was set to make the plastic surface slightly rougher than the titanium. It is not provided for the reflector, since here, a model for polished surfaces is used, which always reflects with the original incoming angle. The optical properties of these surfaces were oriented on experience made with the materials in the lab, while keeping the reflector reflectivity high, as the exact determination of those values was considered secondary to the accuracy of the simulation.

6.3.2 Available Macros for the Simulation

Additional parameters for the simulation are provided via macro commands. These are either pre-implemented in Geant4 or implemented directly into the P-OM framework. An overview of all of Geant4s macro commands can be found in its manual [116], so only the commands implemented within the P-OM framework are presented. Since the values for these parameters partially depend on the exact scenario that is simulated, only the commands and their function are given here. For the following analysis of obtained Monte Carlo Data, cases where a parameter deviates from its default value will be explicitly mentioned.

macro	function
<code>/geometry/gdml/file</code>	Selects the correct "mother" GDML file to import. If no file is given, an empty world is loaded.
<code>/geometry/gdml/submerge</code>	If set to true, the world material is set to be water. If false, it is set to air. Default is false.
<code>/geometry/PMT/PCTubeSize</code>	Sets the length of the photocathode tube (see chapter 6.2). Default is 3 mm.
<code>/geometry/PMT/PCThickness</code>	Sets the thickness of the photocathode (see chapter 6.2). Default is 1 mm.

macro	function
/geometry/PMT/GelRingOffset	Sets the overflow of interface gel relative to the tip of the PMT. Default is 0 mm.
/geometry/PMT/setOrigin	Sets the origin of the coordinate system the PMTs will be placed in terms of the global coordinate system.
/geometry/PMT/setRefX	Sets the x-axis of the coordinate system the PMTs will be placed in terms of the global coordinate system.
/geometry/PMT/setRefY	Sets the y-axis of the coordinate system the PMTs will be placed in terms of the global coordinate system.
/geometry/PMT/place	Places a PMT and gel pad unit on specified (r, θ, ϕ) in the previously defined PMT coordinate system.
/geometry/PMT/solidReflector	If true, a solid reflector is placed around the gel pad. Default is false.
/daq/output_file	Sets the path for the output data.
/daq/outProcess_filter	Filterers the output data to only include photons stopped by the given processes.
/daq/outVolume_filter	Filterers the output data to only include photons stopped in the given volumes.
/daq/glass_filter	Filterers the output data to only include photons that reach the P-OMs glass.

6.4 Angular Acceptance Simulations for the P-OM

One of the primary objectives of the Geant4 framework for the P-OM was to derive an angular acceptance function and investigate how this function changes when different modifications are made to the geometry. To achieve this, a light source of 30 cm radius was introduced via the `G4GeneralParticleSource` and its corresponding macros. The P-OM was placed in the center of this light source. Photons were directed inwards with an isotropic sampling in their inclination angle between 0° and 90° offering a homogeneous illumination of the P-OM. As a wavelength, 400 nm was chosen as this corresponds to the most sensitive wavelength for the PMTs as well as close to the wavelength of the laser used in the OMCU test setup of 405 nm.

Assuming radial symmetry around the PMTs and treating each PMT as equal, the

parameter space for an angular acceptance function can be reduced down to three dimensions (see figure 6.5):

- The angular distance δ between the glass-contact-point of the photon and the PMT position the photon was detected in.
- The inclination θ of the photon relative to the glass surface at glass contact.
- The direction ϕ between the photon momentum at glass contact and the direction from the glass contact point of the photon to the PMT, with both vectors being projected onto the plane tangential to the glass at the glass contact point.

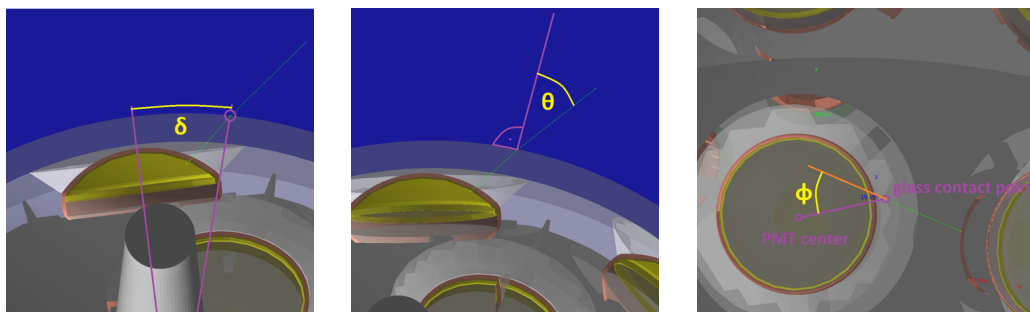


Figure 6.5: The three parameters (δ, θ, ϕ) in which the angular acceptance function is determined. The photon path is displayed in green.

For each of the geometries under investigation, datasets containing 5 million photons were generated. These datasets were then filtered to include only photons that made contact with the glass surface. The angular acceptance function was determined for photons that were absorbed by the PMT's photocathode, and global acceptance metrics were extracted from the data.

6.4.1 Regular Geometry

For the angular acceptance function of the unaltered P-OM geometry, the unmodified CAD drawing in its version 11 was used and converted to GDML as described in chapter 6.2.2. PMTs and gel pads were placed to reflect their positions in the real P-OM, and the entire module was placed in water via the `/geometry/gdml/submerge` command. The P-OM was placed in a way so that one hemisphere points upwards in positive z (azimuth = 90°) and one downwards in negative z (azimuth = -90°). The cable mounting is oriented along the y -axis (polar = $\pm 90^\circ$).

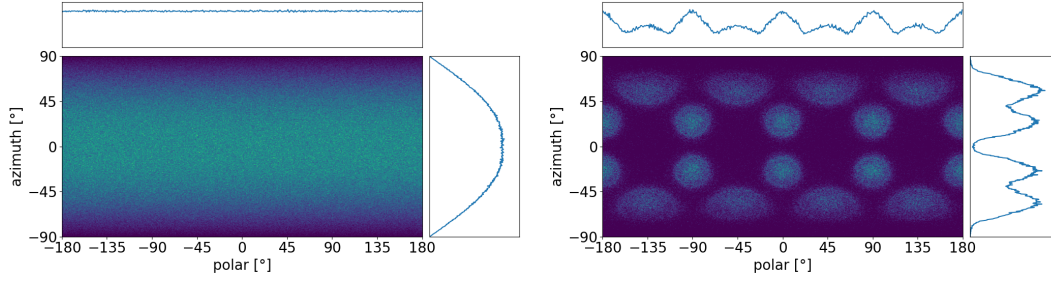


Figure 6.6: Left: Heat-map on the P-OM glass sphere of all photons hitting the glass. Right: The same heat-map filtered to only include detected photons. The P-OM is oriented, with one hemisphere pointing up and one pointing down. On the sides of the plots are projections of the histogram on the azimuth and polar directions.

By generating a heat map on the P-OM glass surface (6.6), first counting the total number of photons registered on the glass and then counting the number of detected photons on the glass, the "capture areas" for each PMT and through that their respective positions within the module are revealed. It is evident that the acceptance oscillates across the surface, exhibiting peaks at the positions of the PMTs. A noticeable drop in acceptance occurs at a 0° azimuth angle between the two hemispheres, together with smaller drops in azimuth between the different rows of PMTs in one hemisphere, as there is still some overlap of the capture areas. In terms of the polar angle, the acceptance peaks are much sharper for the PMTs in the row closer to the "equator" compared to the peaks corresponding to the PMTs near the "poles." While each PMT registers approximately the same number of hits due to the homogeneous illumination, these hits are more widely spread for the PMTs covering a wider range in the polar angle due to the higher angle in azimuth.

The angular acceptance functions in terms of the parameter space (δ, θ, ϕ) are given in figure 6.7. Of special interest here is the relation between δ and θ , as this plot reveals insight into the optical mechanics of the module with regards to collecting photons and directing them toward the PMTs. Multiple clusters can be identified in the δ/θ plot:

- **Cluster A:** This cluster forms a half-moon shape on the left side, with its right boundary aligned with the edge of the gel pad at $\theta = 0^\circ$. It extends up to $\delta = 20^\circ$ for higher values of θ .
- **Cluster B:** Another curved cluster emerges from Cluster A on its right side, extending up to approximately $\delta \approx 55^\circ$. The maximum angle in δ for this cluster lies slightly below the minimum angle required for total internal reflection at the glass/air interface.

- **Cluster C:** This cluster is separate from the rest and of much lower population, located between $30^\circ < \delta < 50^\circ$ and $50^\circ < \theta < 65^\circ$.

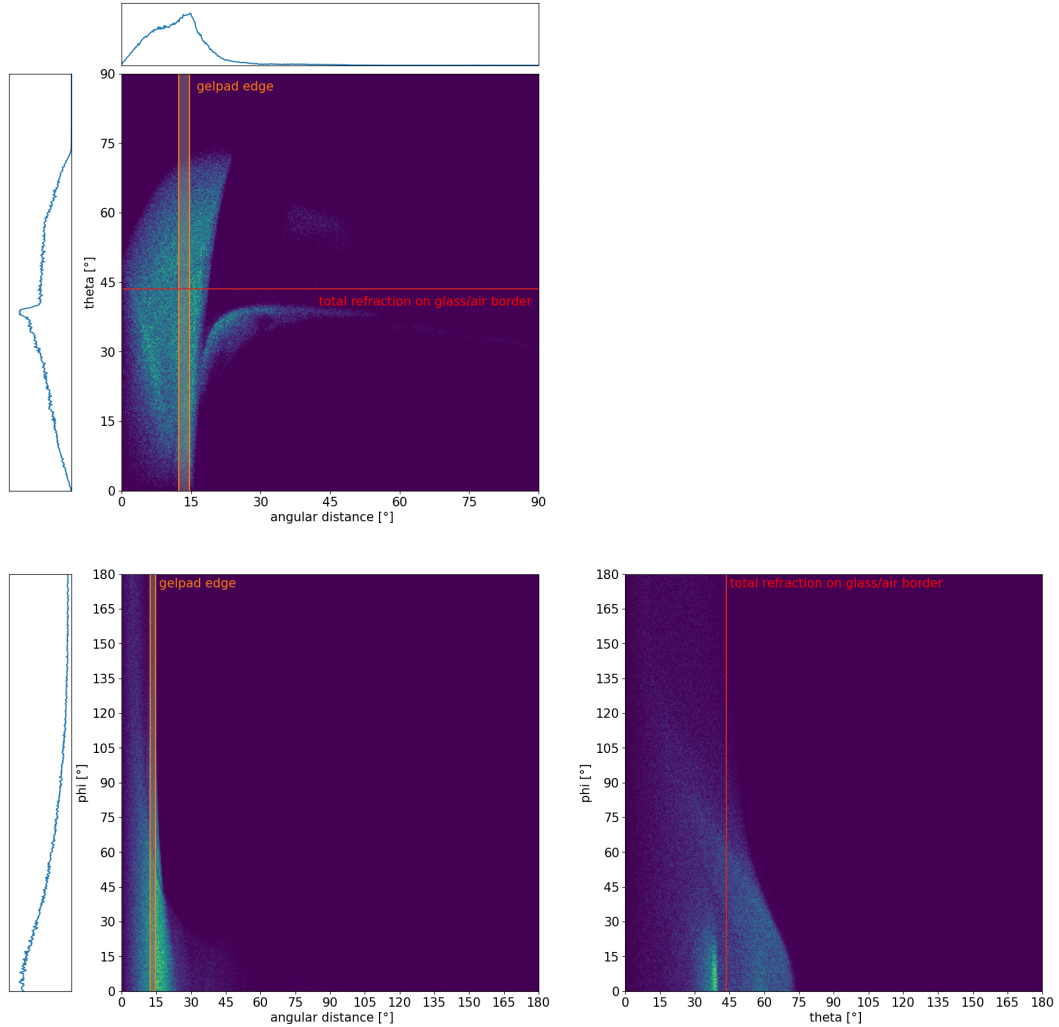


Figure 6.7: The angular acceptance of the Optical Module in terms of (δ, θ, ϕ) . The angular distance in which the edge between the gel pad and air lies, as well as the θ -value under which total internal reflection between glass and air occurs, are marked in the figure. Projections of the histograms onto one-dimensional parameter spaces are given on their respective axes.

Each of those clusters represents a different path the light takes toward the PMT. The θ -angle under which total internal reflection at the glass/air interface occurs, can

be calculated from the refraction indices of water, glass, and air as well as through some trigonometric calculations accounting for the glass curvature along the photon path. It is shown in red in the plot. It can be deduced that photons above this critical angle must pass through a gel pad because they cannot enter the Optical Module solely through the glass. Considering the unique position in angular distance of cluster C, which is approximately equal to the distance between two PMTs, it can be associated with photons that travel through one gel pad towards its edge but do not reach the angle of total reflection at the gel pad edge. These photons are then refracted towards another gel pad, where they are subsequently refracted towards a PMT and detected. Similarly, cluster B extends over a high angular range but remains below the threshold for total internal reflection in the glass. This cluster can be associated with photons that are refracted at the glass/air interface, either towards the exterior of a gel pad or directly towards the photocathode sticking out of the gel pad. Cluster A represents direct photon capture through the gel pad attached to the PMT the photon was detected in. On the right, this cluster is limited by the edge of the gel pad, while for higher angles in θ , higher angular acceptances than the edge of the gel pad can be achieved, since the additional distance towards the gel pad is covered by the photon traveling through the glass. On the top left, cluster A is limited by photons unable to reach the PMT and exiting the gel pad / glass due to their high θ -angle, while on the bottom left, the cluster is unbound but suppressed due to the smaller phase space at lower values of δ and θ . A reconstruction of the events in each cluster through the simulation framework (figure 6.8) confirms the photon paths per cluster.

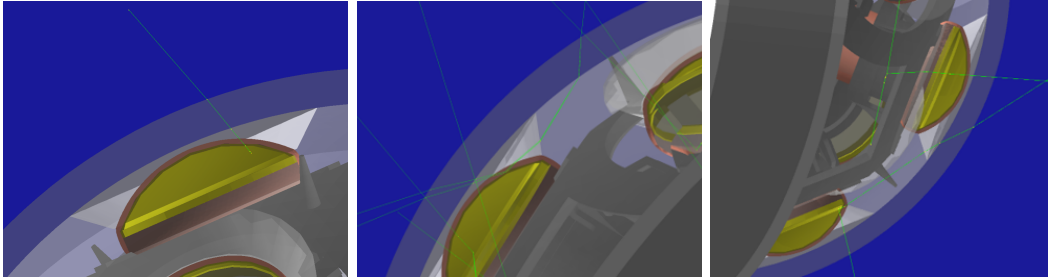


Figure 6.8: Left: Photons of cluster A. Direct capture through the gel pad. Middle: Photons of cluster B. Refraction on the glass/air interface and capture through a gel pad. Right: Photons of cluster C. Refraction through one gel pad and capture by another one.

The relations between ϕ and the other parameters on the angular acceptance as seen in figure 6.7 seem to reflect the purely geometric conditions: For angular distances smaller than a PMT or gel pad edge, photons with ϕ values of up to 180° can reach the PMTs as they can traverse away from the PMT center line and still hit it in its

far edge, while for higher angular distances the photon needs to be directed far more directly towards the PMT to still hit it. Similarly, high values of ϕ are geometrically only possible under almost no inclination of the photon on the glass; in other words, small values of θ . The ϕ/θ projection of the acceptance function also reveals an upper bound for ϕ in terms of θ , best explained through the upper bound on θ in terms of δ and the correlation between δ and ϕ mentioned above.

The vast majority of detected photons are captured directly through the gel pad, with cluster A accounting for approximately 91.0% of all photons. Approximately 7.5% of the detected photons are refracted at the glass-air boundary towards the PMT and gel pad, falling within cluster B. Cluster C contains approximately 0.8% of all detected photons, those being refracted from gel pad to gel pad. The remaining $\sim 0.6\%$ of photons can not be attributed to any cluster and are the result of hardly predictable photon scattering inside the modules' glass as well as in the air volume of the P-OM itself.

The total acceptance of the P-OM, that is, the ratio of detected photons to all photons that make contact with the glass sphere, is 7.09%, while the average angular distance between PMT and glass-contact-point of a detected photon is 12.87° . Viewed from the glass sphere above, this is inside the area covered by the PMT, approximately 1° far from its edge.

The angular acceptance function obtained here through the means of the P-OM simulation framework can be used for further simulations as well as analysis in the context of P-ONE software. A global P-ONE simulation toolkit could therefore propagate photons through water towards the positions of the P-OMs, and then sample from this acceptance function to directly determine if the propagated photon will be detected in a PMT or not. A sampling of the P-OM acceptance based on this acceptance function could greatly increase computational speed while still keeping a high accuracy due to the high degree of realism in the underlying acceptance simulation.

6.4.2 Overflow of Interface Gel

During the process of optically coupling the gel pad to the glass hemisphere, a layer of interface gel is placed in between the two components to avoid capturing air bubbles in between. As "overflows" in this interface gel often occur during integration, a ring of interface gel can remain around the gel pad. The effect of this overflow ring on the acceptance function has been investigated.

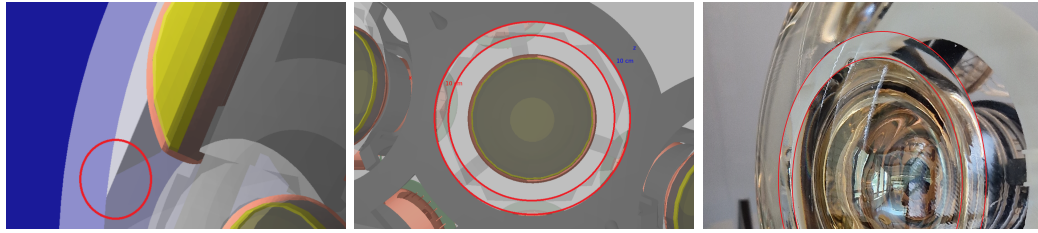


Figure 6.9: Left and Middle: Visualisation of the used geometry with the gel ring marked in red. The ring has a width of approximately 1 cm. Right: Image of a gel ring occurring during assembly of a prototype module.

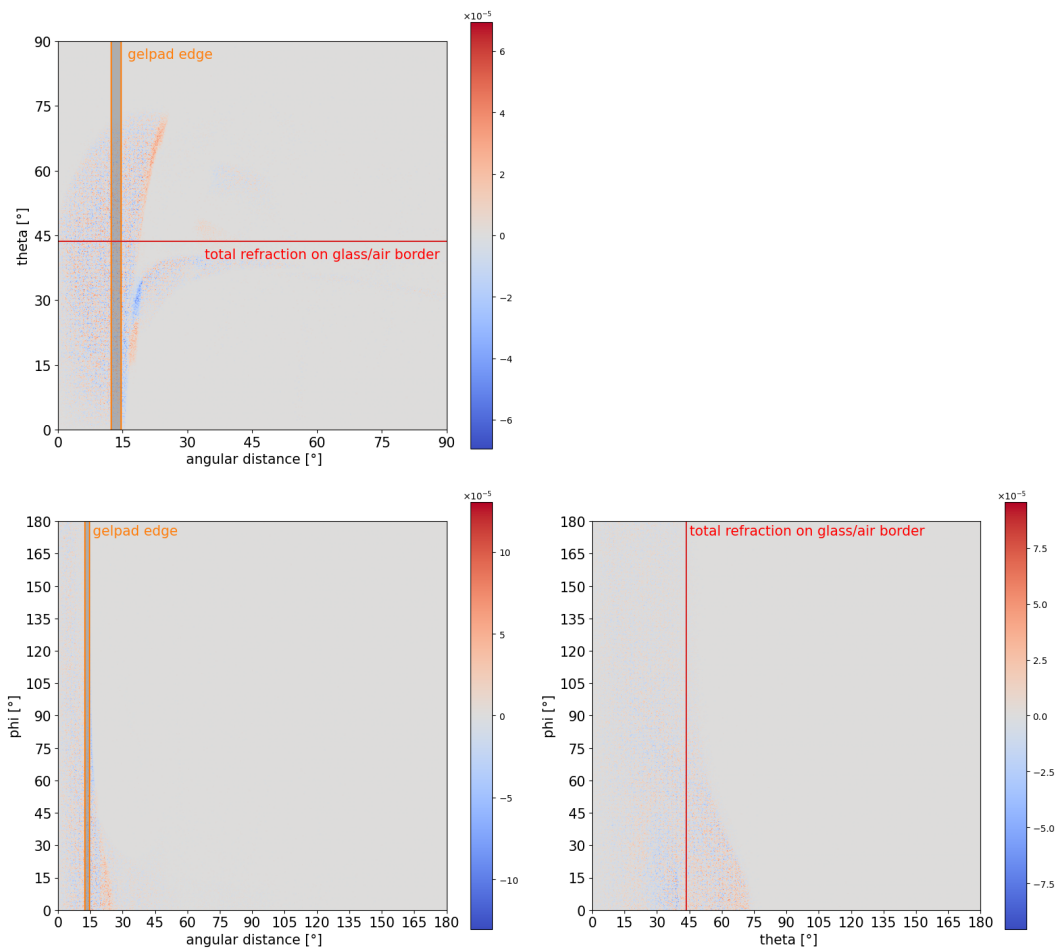


Figure 6.10: Relative difference in the normalized acceptance functions of the modified geometry with gel ring and the unmodified geometry. Red indicates a higher acceptance for the geometry with the gel ring. Blue indicates a higher acceptance for the unmodified geometry.

A rendering of the gel ring using the framework visualizer is shown in figure 6.9. The ring width was set to about 1 cm, which is the upper limit for the ring size in what has been achieved in prototype assemblies of the P-OM. The gel ring was set using the `/geometry/PMT/GelRingOffset` command while the geometry otherwise resembles the geometry in chapter 6.4.1.

Normalizing the acceptance functions of both the geometry with gel ring and the unmodified geometry to an integral of 1 and plotting the relative difference leads to figure 6.10. Significant changes in the angular acceptance are observed within clusters A and B as mentioned in chapter 6.4.1. On the right edge of cluster A, a decrease in acceptance towards smaller values of θ ($< 30^\circ$) can be observed in the geometry with the gel ring. In this region, total internal reflection typically occurs on the inside of the gel pad in the unmodified geometry, redirecting photons toward the PMT. However, with the gel ring, this reflection is suppressed due to the matching refractive index between the ring and the gel pad, resulting in a different direction for the photons. Towards higher values of θ ($> 50^\circ$), an increase in acceptance is observed at the right edge of cluster A, as the increased amount of gel allows for the capture of additional photons at higher angles of δ and θ . Cluster B shows a non-continuous jump in its acceptance function at the angular distance of the outer end of the gel ring ($\approx 18^\circ$), as a consequence of the kink in the surface in contact with the air at this location. Compared to the unaltered geometry, the part of cluster B where photons traverse through the gel ring instead of directly entering the air through the glass is shifted towards lower values of θ , as the gel ring refracts light in different angles compared to the glass due to their different surface normals. While the change in the acceptance function in δ and θ offers insight into the altered optical mechanics due to the gel ring, no significant changes in the ϕ projections of the function could be observed.

Calculating the total acceptance resulted in around 7.10% compared to the unmodified geometry with 7.09%. The total average angular distance increases from 12.87% for the unmodified case to 12.94% with the gel ring. It seems that the various decreases and increases in the acceptance due to the gel ring cancel out to the degree that no significant impact on the total acceptance can be observed. As especially the decreases in cluster A are placed at smaller angular distances than the increases, a slight increase in the average angular acceptance can be observed.

Overall, the simulation results suggest that a gel ring with a width of around 1 cm has no significant effect on the optical performance of the P-OM. For the assembly and resulting quality control, such an overflow ring can be seen as acceptable.

6.4.3 Lower gel pad

Due to specifications about the photocathode size in the R14374 data-sheet, the gel pad was designed to encompass only the part of the PMT's photocathode, where Hamamatsu guarantees a high collection efficiency for photo-electrons. Because of this design choice, the lower edge of the gel pad does not perfectly align with the lower edge of the photocathode. This placement has been considered in the simulation framework's geometry implementation and was modeled according to the real-life counterpart. However, an investigation into the effects of placing the gel pad lower, to encompass all of the photocathode was performed. The investigation happened under the assumption of the same collection efficiency inside and outside of the range guaranteed by Hamamatsu.

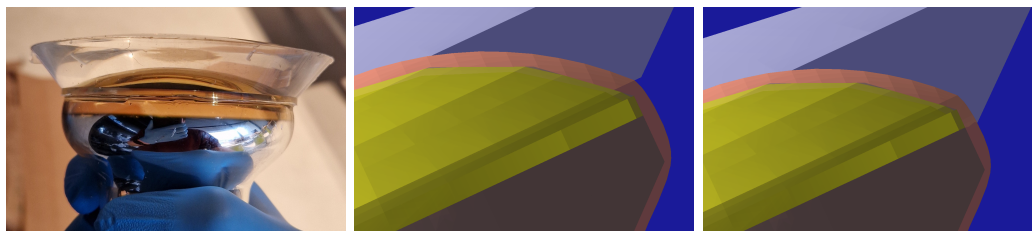


Figure 6.11: Left: A real-life gel pad not covering the entire photocathode of a PMT. Middle: The default geometry implementation in the framework implementing that misalignment. Right: The investigated case of the gel pad fully covering the photocathode.

The gel pad was slightly lowered towards the PMT by about 5 mm during the geometry construction described in chapter 6.2.1 to cover the photocathode fully. The gel pads' opening angle remained the same. As the simulation-gel pad is modeled larger on the sides of PMT and glass hemisphere than its real-life counterpart, with the additional parts being "cut" away during assembly, no further modifications on the gel pad geometry needed to be performed. A visual comparison between a real gel pad, the default gel pad in the simulation framework, and the lowered gel pad is given in figure 6.11. Besides the lowered gel pad, the geometry equals the reference geometry from chapter 6.4.1.

Once again, obtaining the relative difference in the angular acceptance function (figure 6.12) and observing changes in the correlation between θ and δ , an extension of cluster A towards higher angular acceptances can be observed. This extension results as a direct consequence of the lowered gel pad, increasing the angular distance of the gel pad edge while keeping the opening angle of the pad the same and subsequently allowing more photons to be captured and directed toward the pho-

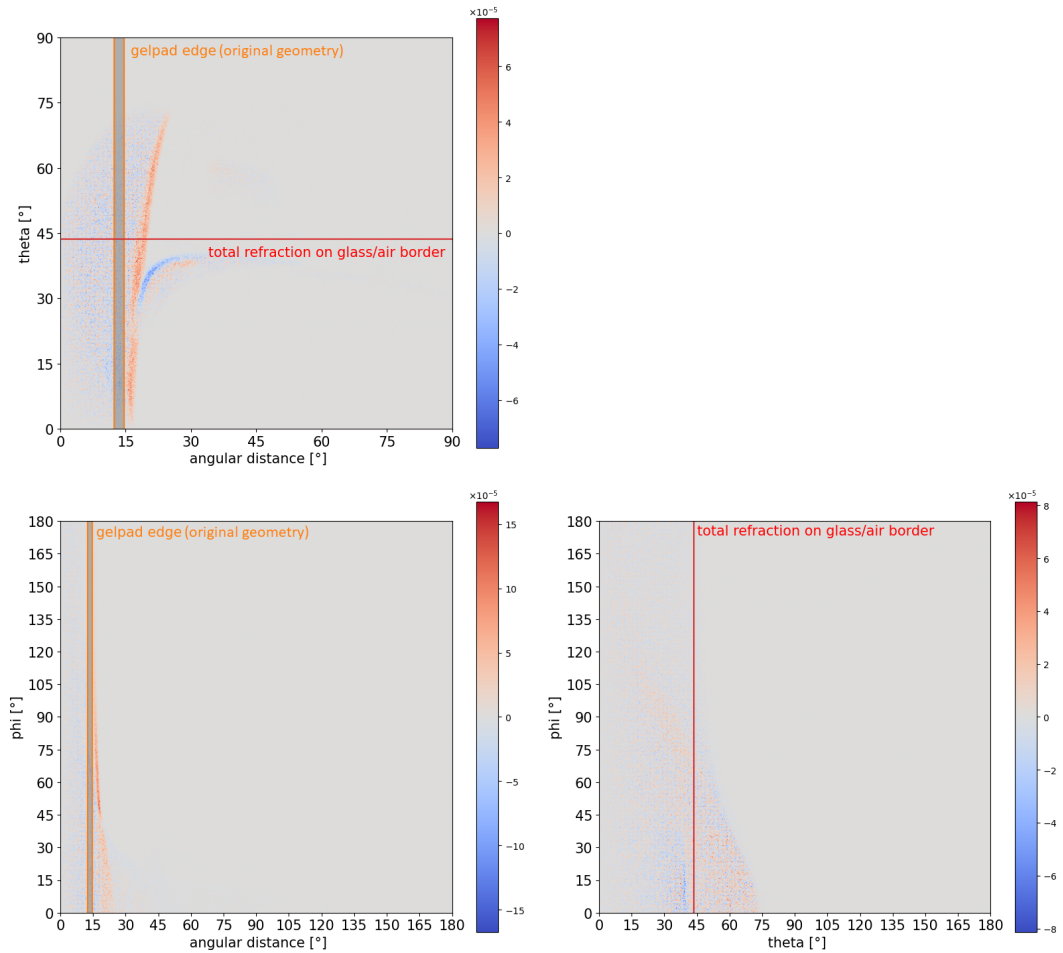


Figure 6.12: Relative difference in the normalized acceptance functions of the modified geometry with a lowered gel pad and the unmodified geometry. Red indicates a higher acceptance for the geometry with the lowered gel pad. Blue indicates a higher acceptance for the unmodified geometry.

tocathode. Due to the same effect, cluster B also experiences a slight shift towards higher angular distances. The shift, in pair with a slight change in the relative amount of photons from cluster B towards cluster A, manifests as a decrease in acceptance at the top-left edge of cluster B.

With the lowered gel pad, the total acceptance could be improved to 7.54 % compared to 7.09 % for the default placement. The mean angular distance also increased to 13.19° compared to 12.87° in the default case. Under the assumption that the collection efficiency does not drop drastically in the newly covered areas, it is suggested to alter future gel pad designs in a way so that the entire photocathode area of the PMT will be covered.

6.4.4 Closed Frame

As mentioned in chapter 6.4.1, around 0.6% of all photons under homogeneous illumination can not be associated with one of the clusters describing a capture path but behave in unpredictable ways, often getting detected in a PMT far away from their original contact point with the glass. While those photons seem to be rare, if one is captured within a generally low-light event, they could significantly decrease the angular resolution of that event. Here it is investigated, if closing the holes in the mounting frame could suppress the detection of these photons to a sufficient degree.

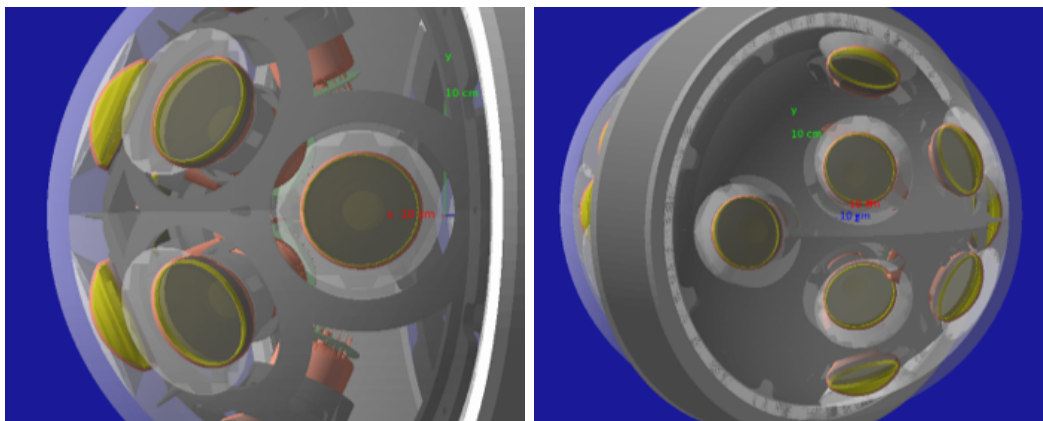


Figure 6.13: Left: The default geometry with holes in the mounting frame. Right: The mounting frame with closed holes.

Figure 6.13 shows a rendering of the default frame as well as the frame with the holes between the PMTs closed. Repeating the analysis from chapter 6.4.1 for the

closed frame reveals a decrease in "non-clustered" photons of around one half from 0.6% to 0.3%. While photons that would have otherwise entered the inside of the module through those holes were absorbed in the frame, photons scattering inside the glass or entering the inside of the frame through the holes for the PMTs seem to be still causing around half of the "non-clustered" events.

Given only a reduction in half can be achieved of an already rarely occurring event type, it should be carefully evaluated if a further investigation into the preference of closed holes is feasible at all, since for this, a most likely time-consuming estimate on how those photons influence the angular resolution of an entire P-ONE event reconstruction needs to be completed. It shall further be noted, that most of the holes will be at least partially covered by devices inside the P-OM anyways.

6.4.5 Solid Reflector

One of the key design innovations of the P-OM is the use of transparent gel pads instead of solid reflectors to capture light toward the PMTs. While a solid reflector is able to direct more photons to the PMT that fall inside its cone, a transparent gel pad can additionally capture light from the side while still providing some of the reflectors' capabilities through total internal reflection at the border between gel and air. To crosscheck this design choice, the P-OM acceptance with a solid reflector around the gel pad was evaluated.

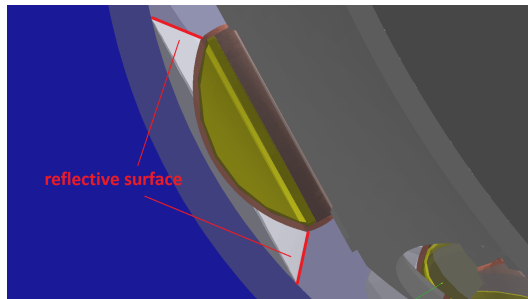


Figure 6.14: Rendering of a PMT, gel pad, and glass with the solid reflector surface drawn in.

Using the `/geometry/PMT/solidReflector` macro command, a solid reflector surface was placed around the border between the gel pad and air as shown in figure 6.14. The reflective surface has the same optical properties as the reflector inside the PMT, thereby reflecting the light with its incoming angle.

Figure 6.15 shows the difference in normalized acceptance functions between the

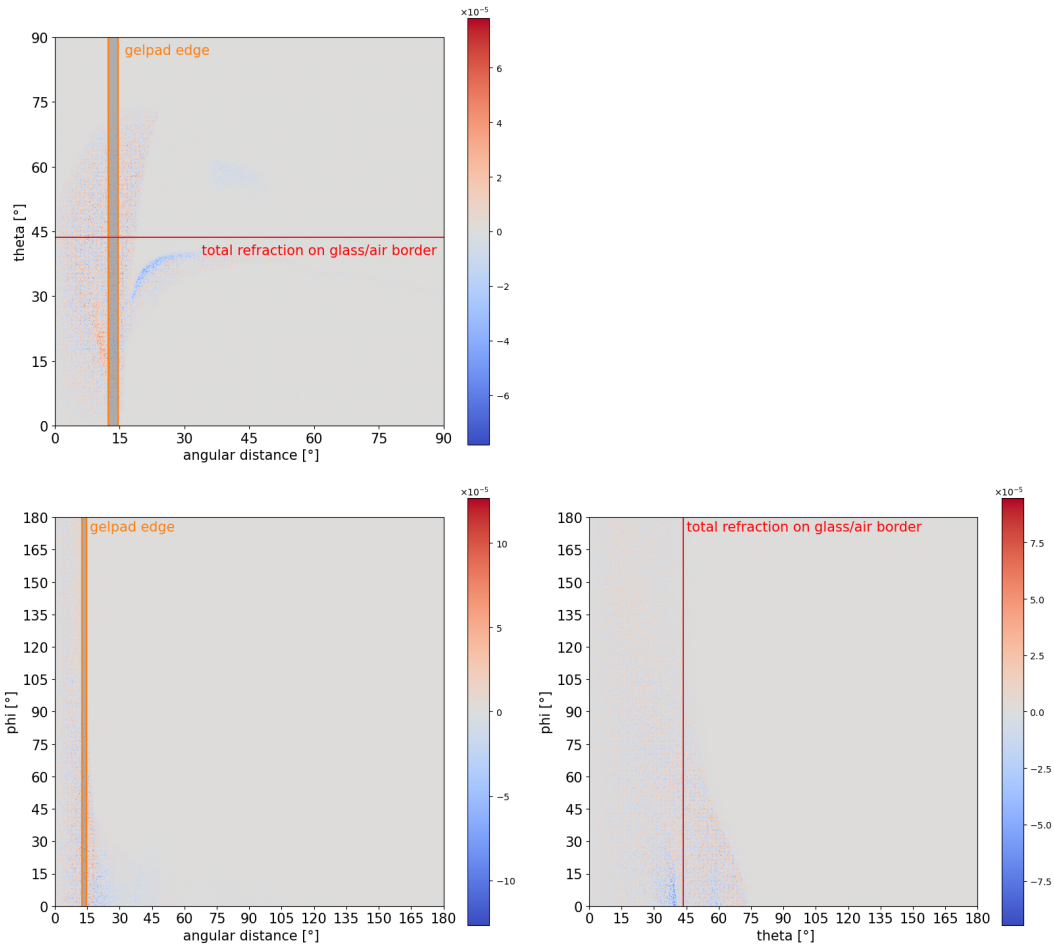


Figure 6.15: Relative difference in the normalized acceptance functions of the modified geometry with a solid reflector and the unmodified geometry. Red indicates a higher acceptance for the geometry with the solid reflector. Blue indicates a higher acceptance for the unmodified geometry.

geometry with the solid reflector and the default geometry. Once again, looking into the dependency of δ and θ , a decrease in acceptance at the upper edge of cluster B is visible. Here, the solid reflector blocks light from entering the gel pad and reflects it back into the inside of the module. On the contrary, an increase in cluster A can be seen at $\theta < 30^\circ$, covering an angular distance from around 10° up to the gel pad edge. Here, the reflector is able to capture photons that would otherwise hit the gel pad edge at an angle not high enough for total internal reflection, thereby leaving the gel pad towards the air. Noticeably, cluster C disappears completely, since the reflector blocks any path that would lead in and out of the gel pad on its side.

The total acceptance decreased from 7.09% for the default geometry to 6.91% for the solid reflector, thereby supporting the design choice of a transparent gel pad that is able to capture photons through its side. Because the solid reflector is unable to do this but has the ability to capture more photons in the area above the PMT, the average angular distance for all detected photons decreased from 12.87° for the default geometry to 12.39° for the solid reflector.

6.5 Muon Beam Simulations for the P-OM

While simulations under homogeneous illumination reveal insight into the optical mechanics of the P-OM and help to obtain general acceptance functions, they do not resemble what the Optical Module would see in a real-world event. For this reason, muon events with an energy of 1 TeV were simulated in the framework resulting in detected Cherenkov photons in the P-OM.

The muons were simulated to traverse in parallel with the detector line (y-axis), at a distance of 5 meters each in the x and z direction. The beam was pointed upwards, starting from 50 meters below the P-OM. To aggregate data and allow for a better visualization of the signal, a total of one hundred muons were simulated. Figure 6.16 shows the photon impact that the muons left on the P-OM. Here, the P-OM is located sideways, with one hemisphere pointing upwards and one pointing down. The cable goes along $\pm 90^\circ$ in the polar angle.

Given that the P-OM simulation framework does not include an implementation of photon scattering in water, the results presented here should be understood as a first-order estimate on the photon impact of a muon event on the P-OM to aid the development process of the first detector line for P-ONE. From the viewpoint of the P-OM, the muon track lies in one of the two hemispheres, traversing along the cable from -90° to 90° . Most detected photons originate from the muon position where the forward-facing Cherenkov cone intersects the P-OMs position. However, some

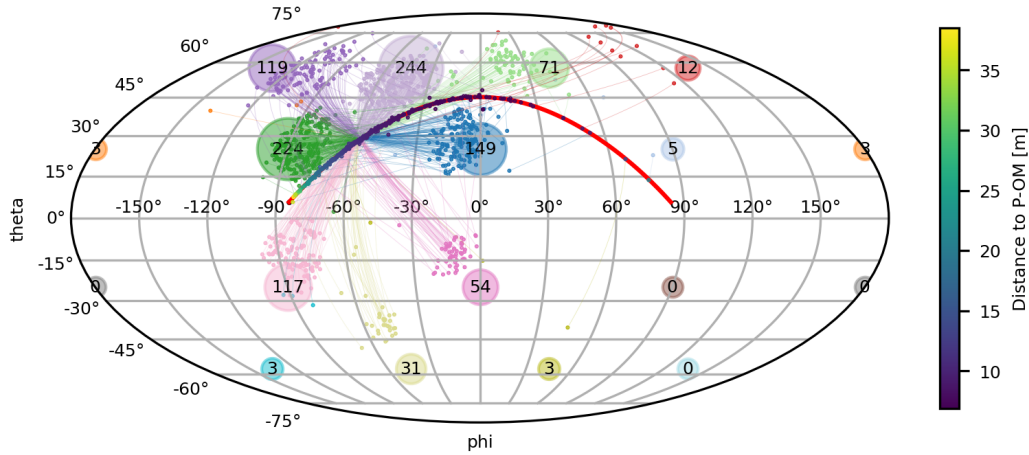


Figure 6.16: Simulated signal accumulated from one hundred muon events traveling upwards along the cable as seen from the P-OM. The muon track is shown in red. On top of the red line, the initial positions of all Cherenkov photons that get detected by the Optical Module are shown as small dots, their color representing their distance to the P-OM. The PMT positions are shown as big dots together with the number of detected photons per PMT. The glass-contact-points of detected photons are shown as small color-coded dots resembling the corresponding PMT color. Initial position and glass-contact-point of each photon are connected by a color-coded line.

photons originate from later positions where the muon already went past the module. As backward scattering of photons is not implemented in the simulation, these most likely originate from Cherenkov light of secondary particles, such as electrons, that were ionized by the muon.

From one hundred muon events, roughly 1000 photons were absorbed in the photocathode. Most of those photons got absorbed in PMTs facing the muon track, with a low two-digit number of photons being detected in opposite-facing PMTs. Even though the track is only traversing one of the hemispheres, two PMTs in the other hemisphere seem to have collected a significant amount of photons (light and dark pink in figure 6.16). Since the track starts at 50 meters away from the P-OM, photons are able to travel to the other hemisphere due to the Cherenkov opening angle resulting in those PMTs being illuminated.

Additional plots for different muon directions and energies can be found in appendix A.2.

6.6 Single PMT Angular Acceptance

With angular acceptance functions of the full P-OM obtained, the question remains on how well they compare to lab measurements. As both a functioning P-OM prototype and OMCU upgrades to facilitate the P-OM are currently still in development, a comparison in angular acceptance could only be made with a single PMT.

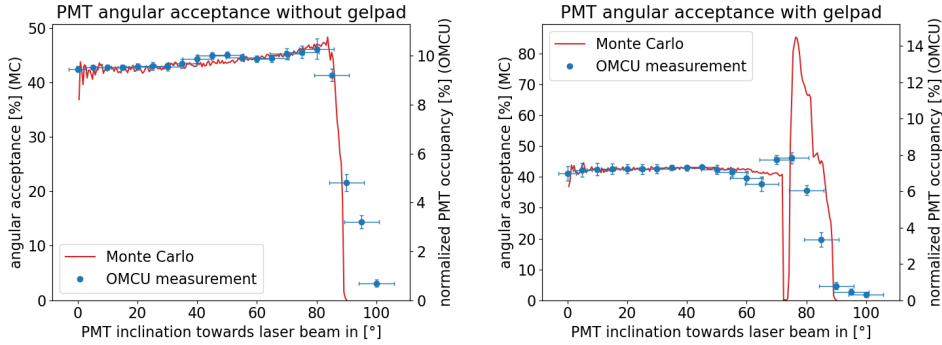


Figure 6.17: Monte Carlo and OMCU data for the angular acceptance of a PMT without (left) and with (right) gel pad.

Following the rotation stage setup in the OMCU, a digital PMT was placed so that the coordinate origin aligns with the intersection between the photocathode and reflector (visible in figure 6.18). Five million Photons at 405 nm were then targeted towards the coordinate origin from a 20 cm sphere around it. The photons were then binned in 0.1° intervals in the angle relative to the PMT's axis of rotation, and for each bin, the ratio of photons detected in the PMT to the total number of photons in that bin was calculated. Simulations were repeated for a PMT with and without a gel pad.

Data from the OMCU results from the `photocathode_scan` testing procedure (ref. chapter 5.4) of a Hamamatsu R14374, scanning in theta from 0° to 100° and in phi from 0° to 350° , in 5° steps respectively. The PMT was positioned in the rotation stage so that the center of rotation was directly aligned with the interface between the photocathode and reflector. For the evaluation, the angular acceptance was determined through the single photon occupancy in the resulting signal. Since the laser output was subject to temperature fluctuations over multiple hours of measurement, the occupancy noticeably shifted by a few percentages over time. To account for this, the obtained data for every scan in theta (at a given angle in phi) was renormalized so that the plateau in occupancy for low values in theta was identical in height over all theta scans. For the OMCU measurement, the error in occupancy results from averaging over the normalized data of different theta-scans.

The error in the inclination angle has been conservatively approximated with a 5° contribution from possible misalignment of the laser's optical fiber and an additional angular-dependent contribution resulting from misalignment of the PMT in the rotation stage, estimated conservatively to be about 5 mm. Measurements were repeated for a PMT with and without a gel pad. The resulting angular acceptance functions in terms of the PMT inclination towards the light beam are given in figure 6.17, together with the simulation results.

Overall, a good agreement between simulation and OMCU data can be seen in the case without a gel pad. Both acceptance functions plateau for low angles with a slight increase visible towards 80° , possibly due to a longer distance photons travel inside the photocathode due to the higher incident angle. Since the photocathode rotates out of the laser beam above 90° , the acceptance drops to zero. This drop happens faster for the Monte Carlo data, while for 95° and 100° , the occupancy is still non-zero in the OMCU. A possible explanation could be a non-zero opening angle of the laser beam when exiting the optical fiber, which was not accounted for in the evaluation.

The case with a gel pad first shows the same plateau as the case without a gel pad, again with simulation and experiment in good agreement. At around 72° , the simulated acceptance drops to zero, only to reach its global maximum right after, at around 76° . The drop can be attributed to photons being refracted inside the gel pad in a way so they never reach the photocathode, while the maximum is the result of a significantly longer photon path through the photocathode at high angles, due

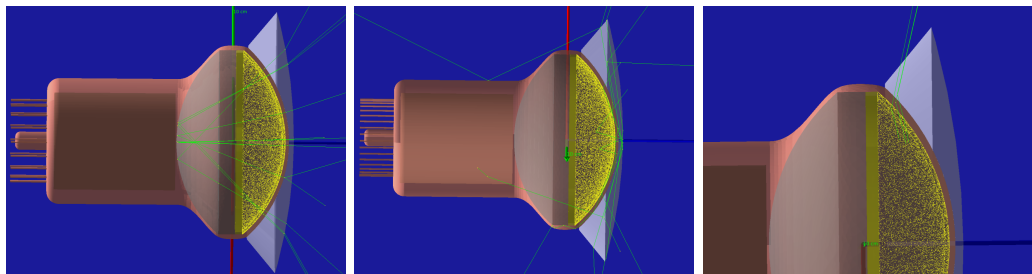


Figure 6.18: Left: At angles below 72° , photons hit the photocathode through the gel pad relatively perpendicular. The angular acceptance plateaus. Middle: At around 72° , photons hit right behind the edge of the gel pad. They are subsequently refracted away from the photocathode, causing the angular acceptance to drop to zero. Right: Above 72° , photons hit the side of the gel pad and get refracted towards the photocathode at much higher angles of incidence than before. This causes a longer path inside the photocathode and, subsequently, a higher acceptance.

to an increased angle of incidence. Both effects are displayed in figure 6.18. While still visible, the drop and the following maximum are much less pronounced in the OMCU data. Reasons could be, on the one hand, defects on the gel pad, like unclear and rough edges or dirt on the surface, which smear out the drop and peak. On the other hand, the implementation of the photocathode in the P-OM framework could be subject to imprecisions in regards to thickness and absorption length, as little to no direct information was provided by Hamamatsu. However, the otherwise good agreement between Simulation and experiment still puts confidence in the simulation framework. A future, more precise fitting of the photocathode thickness for the simulation could, in theory, be done by adjusting for the peak-to-plateau ratio to be in better alignment with the experiment. Before, however, the OMCUs' and PMTs' systematical uncertainties with regard to the angular acceptance need to be better understood.

On a last note, it should be mentioned that the occupancy measured in the OMCU and the angular acceptance of the simulation might only be proportional to each other up to some degree. As the simulation only treats the detection process up to the photon absorption in the photocathode, the angular-dependent effect of the collection efficiency is not respected. While the collection efficiency should be rather constant around the center of the PMT, this is expected to break down at the edges of the photocathode. The resulting additional angular dependent factor present in the OMCU data and lacking in the simulation could be an additional source of discrepancies between the simulation and experiment.

6.7 Performance of the Framework

The use of a detailed set of facets in the geometry implementation raises the question of whether this approach has an impact on the simulation run time compared to a simpler implementation using basic geometric shapes. Figure 6.19 shows the CPU times required for simulating different numbers of photons. These CPU times were measured for various geometries: an empty world with no solids, a single PMT and gel pad constructed as described in section 6.2.1, a tessellated hemisphere of the P-OM, and a complete P-OM with two hemispheres. In order to get comparable results and make sure all simulated photons interact with the simulation geometry, photons were launched from a 30 cm sphere around the origin and directed straight inwards. The measurements were conducted on an Intel Core i5-12400F processor, with Geant4 running in single-threaded mode on a Windows subsystem for Linux.

Here, the measured CPU time refers only to the time for the pure run, which is in the order $\mathcal{O}(n)$. Initialization time for Geant4 and time to load in the geometry,

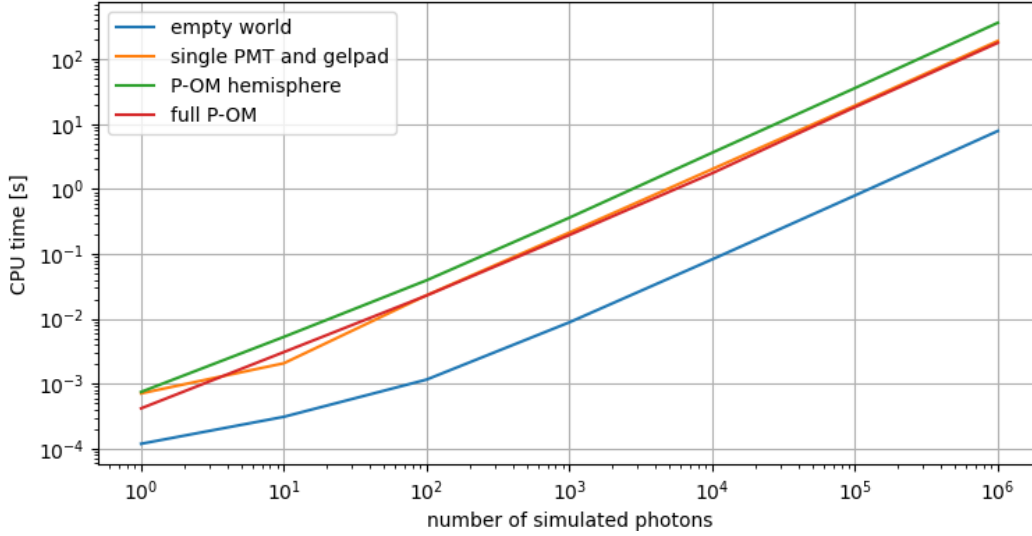


Figure 6.19: CPU times under different geometries for a given number of simulated photons on an Intel Core i5-12400F. The simulation framework was run in single-thread mode in a WSL shell.

which are $\mathcal{O}(1)$ and in the order of around one minute for the full P-OM, are not included. Interestingly, the performance seems to not greatly depend on the complexity of the geometry but more on the possibility of photons to interact with the geometry, in other words, on how many steps a photon is able to perform in the simulation. This is evident in the drastic performance difference between the empty world and the single PMT, as the PMT offers high interaction opportunities with a relatively simple geometry, while little to no photon scattering can occur in the empty world. Additional evidence is the similar performance for the single PMT and the full P-OM with lower performance for the single hemisphere, even though it uses only around half the facets of the full P-OM. As the hemisphere is modeled open on the lower side, photons coming from the bottom will enter freely and scatter inside the module, requiring Geant4 to simulate more steps than if the photons might get absorbed faster.

The reason for this seems to be optimizations in the Geant4 geometry navigator, which indexes parts of the world in terms of which solids are present [117]. If a particle is present in one of those parts, only solids in this part will be evaluated for the particle simulation. This greatly increases performance for complex geometries like the P-OM to the degree where a similar performance as in the case of the simulation of a single PMT is achieved.

Chapter 7

Integration of P-ONE's First Optical Modules

In parallel to the development of the OMCU as a testing facility for PMTs and the simulation framework as a digital twin for the P-OM, the preparation for integration of the P-OM itself was undergoing. This includes the development of integration procedures for the gel pads and PMTs as well as testing and quality control procedures for the μ Base, the PMT, and the assembled P-OM hemisphere. In order to facilitate the assembly of all 40 hemispheres for P-ONE-1 at the TUM lab, a clean room called *The Optical Tent* was constructed to allow for a dust-free operation environment. In the following chapter, an overview of gel pad integration, the Optical Tent, and the integration and testing procedures for the P-OM are presented.

7.1 Gelpad Production and Optical Coupling

The P-OM's gel pads provide optical coupling between the PMT and the glass hemisphere. They consist, for the most part, of Wacker Silgel 612 [114] with an additional interface gel consisting of Wacker Elastosil RT 601 [118]. Their exact molding and integration procedure has been subject to investigation [91], with a finalized manual for the P-ONE-1 production provided in [119].

After evaluating multiple molding options for the gel pad production, curing them with the PMT already in place was found to be the most suitable. This approach reduces alignment errors while offering a more streamlined integration compared to separate curing with a subsequent connection to the PMT. For this approach, the gel is mixed and then stirred in a vacuum environment to reduce bubbles inside. The gel is then poured into a custom-made mold with a hole at the top, into which the PMT is placed (ref. figure 7.1). This mold is coated with interface gel before

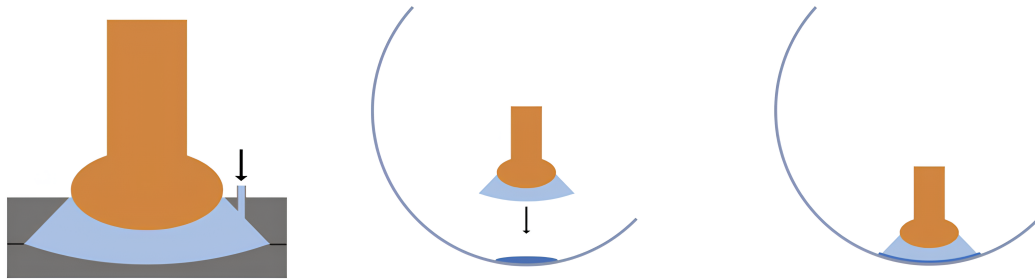


Figure 7.1: Schematic drawing of the gel pad integration procedure. The gel pad is cured in a mold with the PMT in place (left). After curing the gel pad, a layer of interface gel is placed in the hemisphere (middle), and the PMT and gel pad are placed on top (right). Images courtesy of L. Ginzkey.

filling in the main gel, to easily remove the resulting gel pad later on. The curing process for the gel pad then lasts up to 24 hours.

For the PMT integration, the hemisphere is rotated so that the PMT to be integrated will point downwards. To avoid incomplete coupling of the gel pad to the glass by leaving air gaps, interface gel is placed on the glass before lowering the PMT (ref. figure 7.1). A sweet spot between air gaps and overflow of interface gel has been found at 7 g of gel [119]. The PMT is then held in place by a temporary holding mechanism for 24 hours until the interface gel is fully cured. Afterwards, the spring-loaded holding structure is placed to further keep the PMT in place. This process is repeated for all 8 PMTs of the hemisphere.

7.2 The Optical Tent

In order to ensure a clean optical coupling between PMT and the glass housing, it is essential to maintain a dust-free integration environment. Particular attention should additionally be given to the air quality at the planned integration facility, because the proximity to a nearby construction site has resulted in the influx of fine-grained dust into the P-ONE labs at TUM. The solution involves the construction of a clean room at the TUM lab, offering space for integration and storage of the P-OM hemispheres.

The resulting *Optical Tent* is a 3.8 x 3.5 m clean room with an inside height of around 2 m. The inside is closed off by four solid all-plastic walls, the upper half consisting of transparent acrylic glass. On one side, a 2 m wide entry area is covered by a

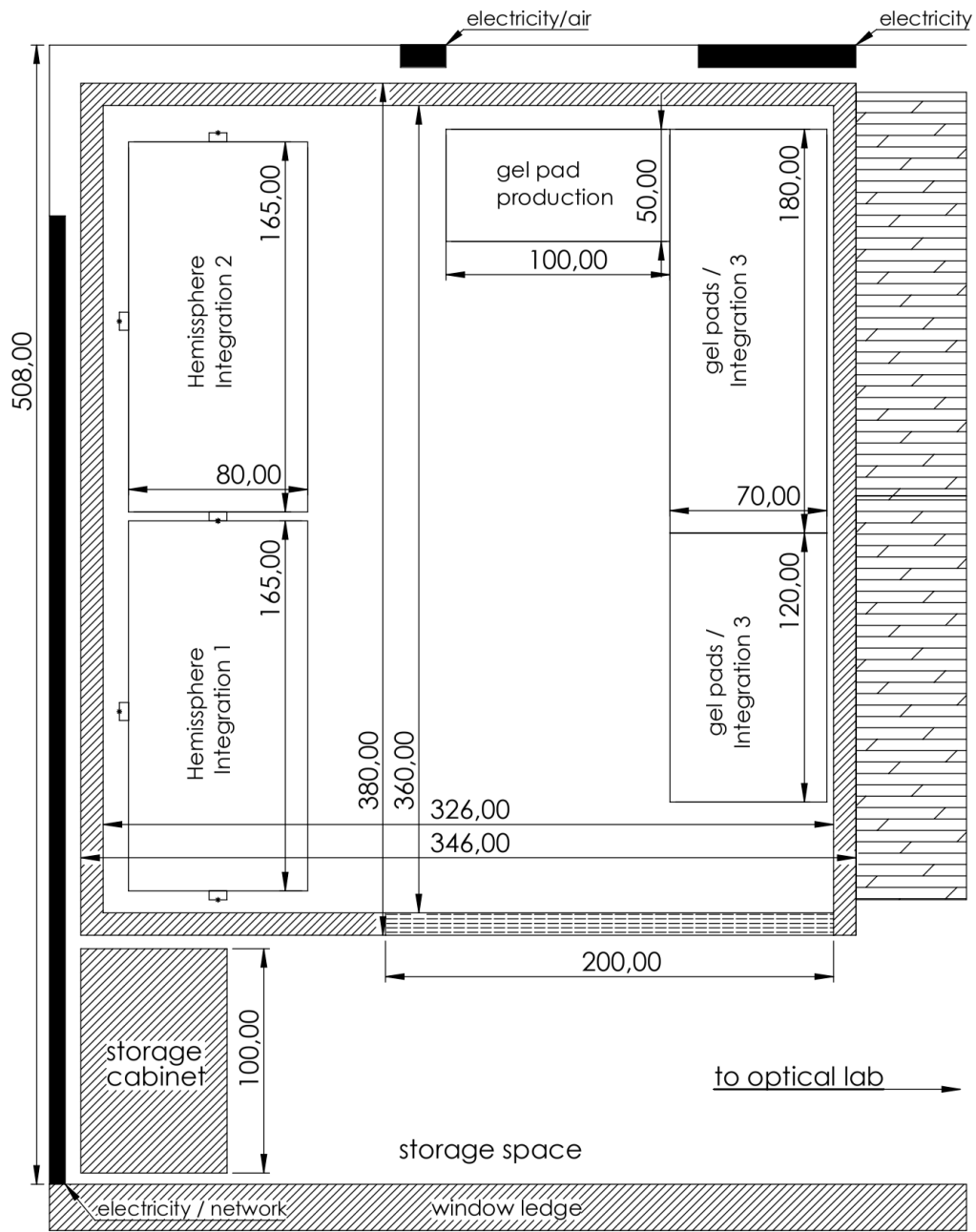


Figure 7.2: CAD drawing of the Optical Tent's dimensions together with dedicated working areas on the inside and storage areas on the outside. All lengths are given in cm. Figure created in collaboration with B. Nührenbörger.



Figure 7.3: The Optical Tent from the outside (left) and inside (right). On the outside table on the left, an integrated P-OM prototype is visible.

striped PVC curtain. On the roof, two Fan-Filter-Units (FFU) with HEPA filters blow air inside the tent while eliminating 99.95% of all particles larger than $1\mu\text{m}$ in the air flow. On the bottom, an approximately 5 cm gap between the floor and wall allows for air to exit the tent again, causing a laminar flow from top to bottom inside the tent. Light inside is provided by LED strips mounted to the ceiling and on the upper sides of storage shelves.

Once fully equipped, the Optical Tent will house two two-level heavy-load shelves for the integration of the PMTs in the hemispheres. The available space allows for approximately eight hemispheres to be integrated in parallel, with one hemisphere taking about two weeks for complete PMT integration, due to gel curing times. Next to those shelves are tables for the gel pad curing. Storage space is available either under tables or inside airtight boxes outside the clean room.

7.3 Assembly, Testing and Quality Control for the P-OM

While the complete assembly, testing, and quality control plan for the P-OM is not yet fully fixed at the time of writing, a few key points and procedures are already agreed upon or seem indispensable to produce P-OMs of sufficient quality:

Before soldering the externally assembled μBases onto the 400 P-ONE-1 PMTs, they need to be tested at least for connectivity to the micro-controller and generation of the correct Dy10 voltage. A test setup to streamline this process is in development, with an expected testing time per μBase in the order of under one minute. As the soldered connection will be difficult to separate again, this will be the last chance

to eliminate faulty μ Bases without also losing the attached PMT. Each μ Base has a unique ID encoded in its micro-controller, which can be read out digitally. This ID needs to be read out and saved together with the serial number of the attached PMT inside a P-OM database. Alternatively, the μ Base board can be marked by a serial number or QR code to replace the micro-controller ID.

Next, all 400 PMTs – a subset was already tested in the OMCU – need to be individually calibrated as a unit together with their attached μ Base. As the OMCU can not reasonably facilitate this task, PMTs will be shipped to the testing facility in Aachen [98], where already the prototype μ Bases were evaluated (ref. chapter 5.2). Here, they can be tested in bulk, with a testing protocol that suits the needs for P-ONE, regarding temperature, gain, and light exposure. The calibration data for each PMT again needs to be stored in the P-OM database. As 400 PMTs are available but only a maximum of $16 \cdot 20 = 320$ PMTs will be placed inside modules, extra margins in the case of PMT failure are available. This margin can also be used to filter by PMT quality by marking the 80 "worst-performing" PMTs from the Aachen calibration and integrating them only if other PMTs break or otherwise under-perform.

The optical coupling and integration of the PMTs into the hemispheres is then conducted in the Optical Tent as described in chapter 7.1. The exact position of each PMT in the hemisphere needs to be stored together with an ID for the hemisphere in the P-OM database. Because of the use of interface gel, PMTs will be easily removable without causing too much damage to the gel pad or leaving gel remnants inside the hemisphere. Even though detailed manuals for the gel pad production and PMT integration exist, the resulting quality of each optical coupling should be inspected and approved by at least two people. In case the quality is deemed insufficient, the PMT needs to be removed and the process repeated.

After the integration of all eight PMTs into a hemisphere, necessary electronics and cabling need to be installed. A mechanism like color coding to avoid wrong cable connections is seen as beneficial. The hemisphere can then be tested inside the upgraded OMCU, utilizing the robot-mounted optical fiber and a flasher mounted at the ceiling (ref. chapter 5.6). Results again need to be stored in the P-OM database. Additional tests besides optical characterization, like vibration and shock tests and temperature cycling, need to be performed as well.

While many details in this procedure still need to be planned out, specifically regarding how μ Bases are tested, how exactly the P-OM database is realized, and how the hemisphere procedures inside the OMCU are defined, confidence exists that the commencing production of the P-OM will lead to 40 finalized hemispheres by late 2023 or early 2024, paving the way for a P-ONE-1 deployment in 2024/2025.

Chapter 8

Conclusion

In this thesis, studies and developments regarding P-ONEs Optical Module, the P-OM, were presented. To motivate the development of the P-OM, and on a larger scope, the development of P-ONE as a novel neutrino telescope in the Pacific Ocean, an introduction to cosmic messengers and neutrino telescopes in general, was given. This introduction highlights the role of observing the cosmic neutrino flux on Earth in enhancing our understanding of the cosmos within the framework of Multi-Messenger Astronomy. To set the development of P-ONE and the P-OM in particular into context, a brief technical introduction of different currently existing neutrino telescopes was presented. This was followed by a technical overview of P-ONE-1, P-ONE's planned first detector line.

In order to properly characterize the photomultiplier tubes (PMTs) that will be deployed in the P-OM, the Optical Module Calibration Unit (OMCU), was designed as a plug-and-play testing facility, allowing for PMT scans in supply voltage, laser tune, and rotation angle of the PMT. The OMCU design, both in regards to hardware and software, was presented. In the scope of the work on the OMCU, the μ Base, a high voltage divider initially developed for the IceCube Upgrade, was integrated within the setup, and the compatibility with the P-OM PMTs was proven. A comparison between PMT characteristics obtained in the OMCU and calibration data provided by the PMT manufacturer was performed, showing good agreement in some quantities while revealing systematic uncertainties of the OMCU regarding others. Future upgrades and improvements to the OMCU will both eliminate these systematical uncertainties and allow for the characterization of an entire P-OM hemisphere as opposed to only a single PMT.

To further understand and improve the optical properties of the P-OM, a highly modular Monte Carlo framework for optical simulations on the P-OM has been developed. The framework utilizes a novel approach of directly importing the P-OMs CAD files, thereby offering a highly precise geometric implementation of the Optical Module. With this approach, the angular acceptance of the P-OM could easily be

evaluated under different design modifications, allowing to study which changes lead to better and worse results. The obtained angular acceptance functions can further be used in other simulation frameworks for P-ONE, allowing for a parameterization of the P-OMs behavior and resulting in faster run times. Comparisons between single-PMT Monte Carlo simulations in the framework and measured angular acceptances in the OMCU show good agreement, putting trust in the accuracy of the simulation framework.

Lastly, the current status of the P-OM production was presented. A quick insight into the procedures for optically coupling the PMTs to the P-OMs glass hemisphere was given. After that, the *Optical Tent* was presented as the clean-room production environment for the integration of the P-OMs for P-ONE-1. A plan for the integration and testing of the P-OM was outlined.

The work presented in this thesis marks an essential step toward the realization of the fully assembled P-OMs for P-ONE-1. However, it does not exist in a vacuum. The development of the P-OM and the entire P-ONE-1 line is an effort put forward by a multitude of highly motivated scientists in the international P-ONE collaboration. Together, they target 2024/2025 for the deployment of P-ONE-1. Until then, however, a lot of work still needs to be done. The P-OMs need to be assembled and tested, the design of the line needs to be finalized and approved, and P-ONE-1 needs to be fully integrated before it can be shipped off-shore and deployed. Many smaller and larger tasks still wait to be completed, but the collective dedication, commitment, and shared vision of the people involved will provide a strong foundation for achieving this goal.

Appendix A

Additional Plots

A.1 μ Base Performance Plots

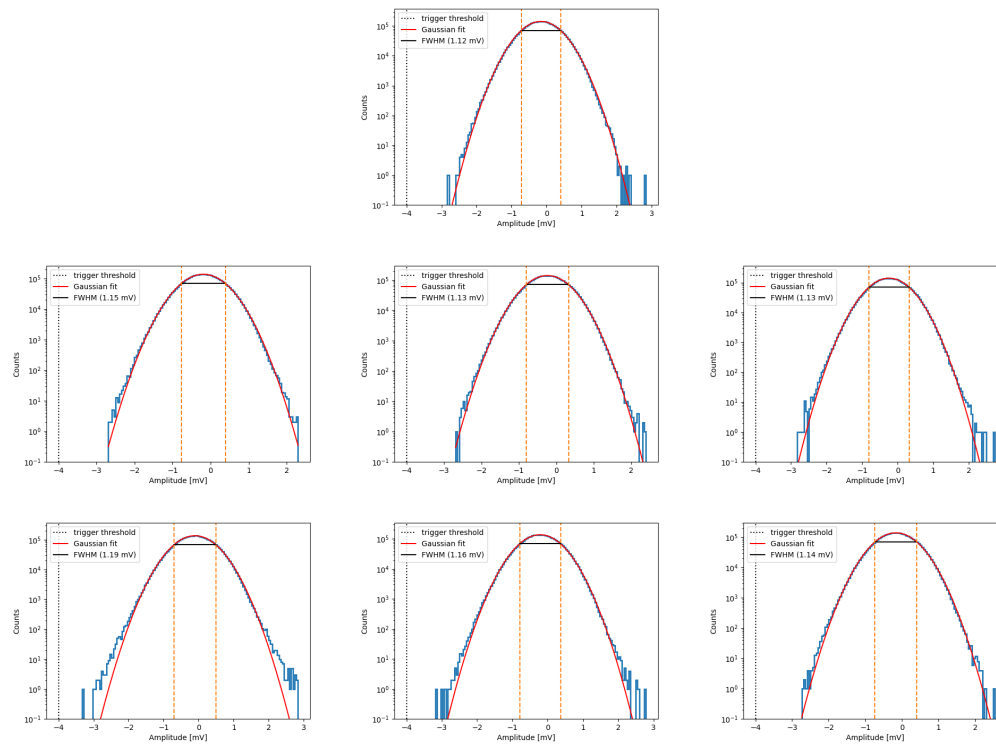


Figure A.1: The noise band on the signal without high voltage applied to the PMT for different μ Bases. Top row: the reference Base. Middle row from left to right: V1A, V2A and V3A. Bottom row: the respective B-variant. For details on the plots refer to chapter 5.2.

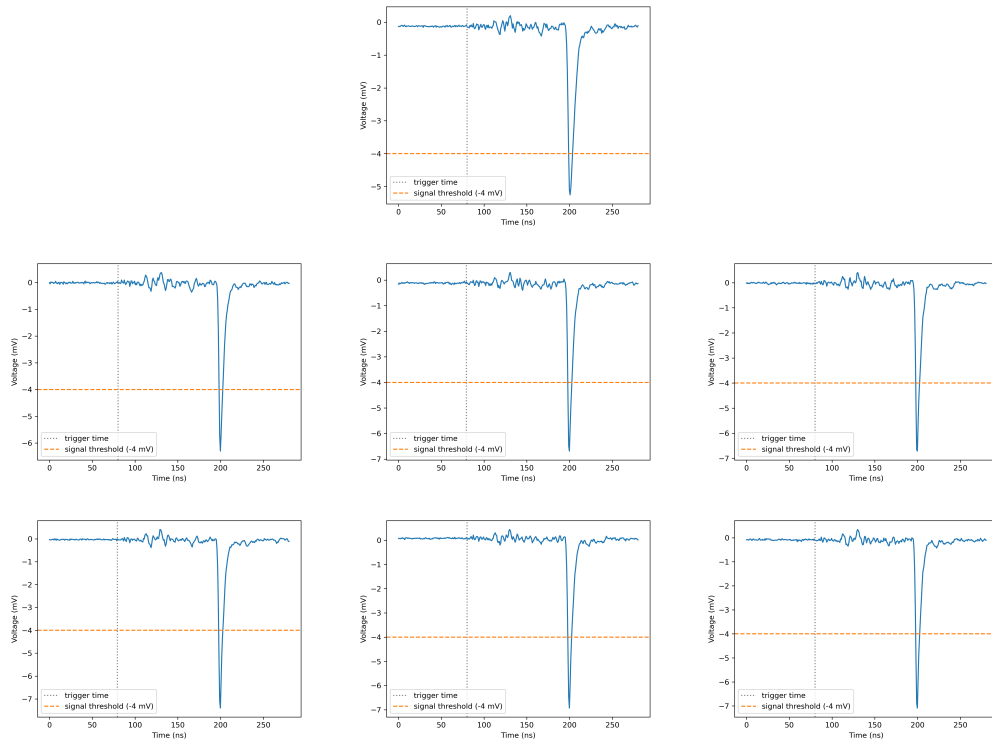


Figure A.2: Averaged single-photon waveform at $Dy_{10} = 85$ V for different μ Bases. Due to the stochastic nature of photon occupancy in the signal, only waveforms crossing a trigger threshold of -3.5 mV were considered for the average. Cross-talk between the trigger and signal channel inside the oscilloscope can be seen as jitters to the left and right of the peak. Top row: the reference Base. Middle row from left to right: V1A, V2A and V3A. Bottom row: the respective B-variant. For details on the plots refer to chapter 5.2.

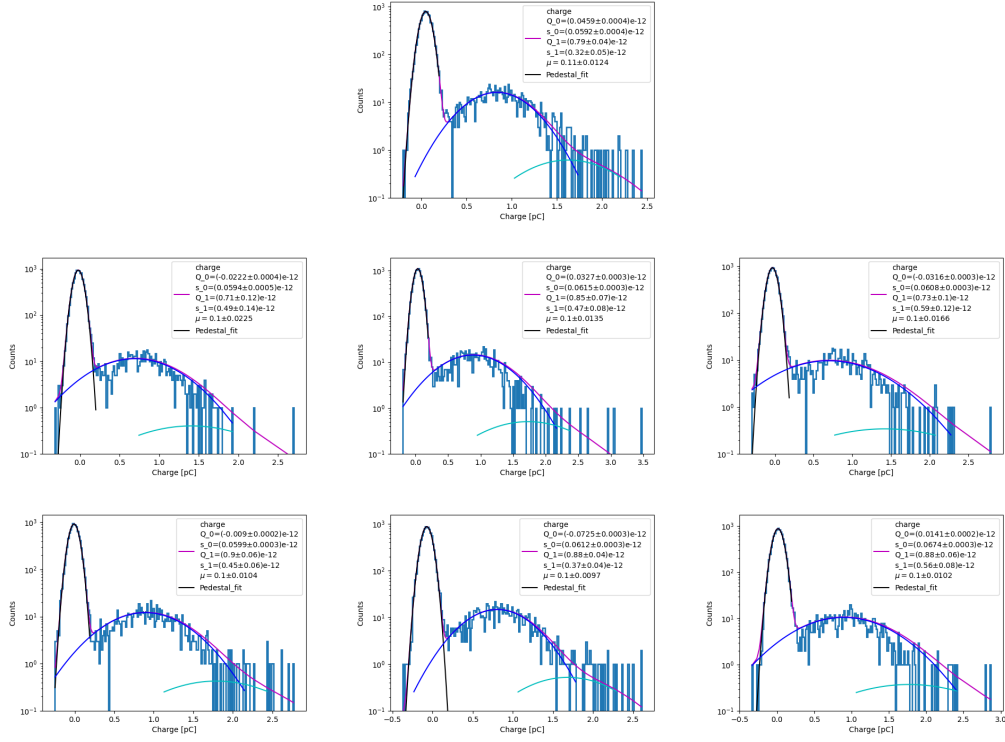


Figure A.3: Single photon charge spectrum for different μ Bases. Measured with the OMCU at Dy10 = 85V. The exact gain might differ between bases due to production effects. Top row: the reference Base. Middle row from left to right: V1A, V2A and V3A. Bottom row: the respective B-variant. For details on the plots refer to chapter 5.2.

A.2 Geant4 Muon Simulations

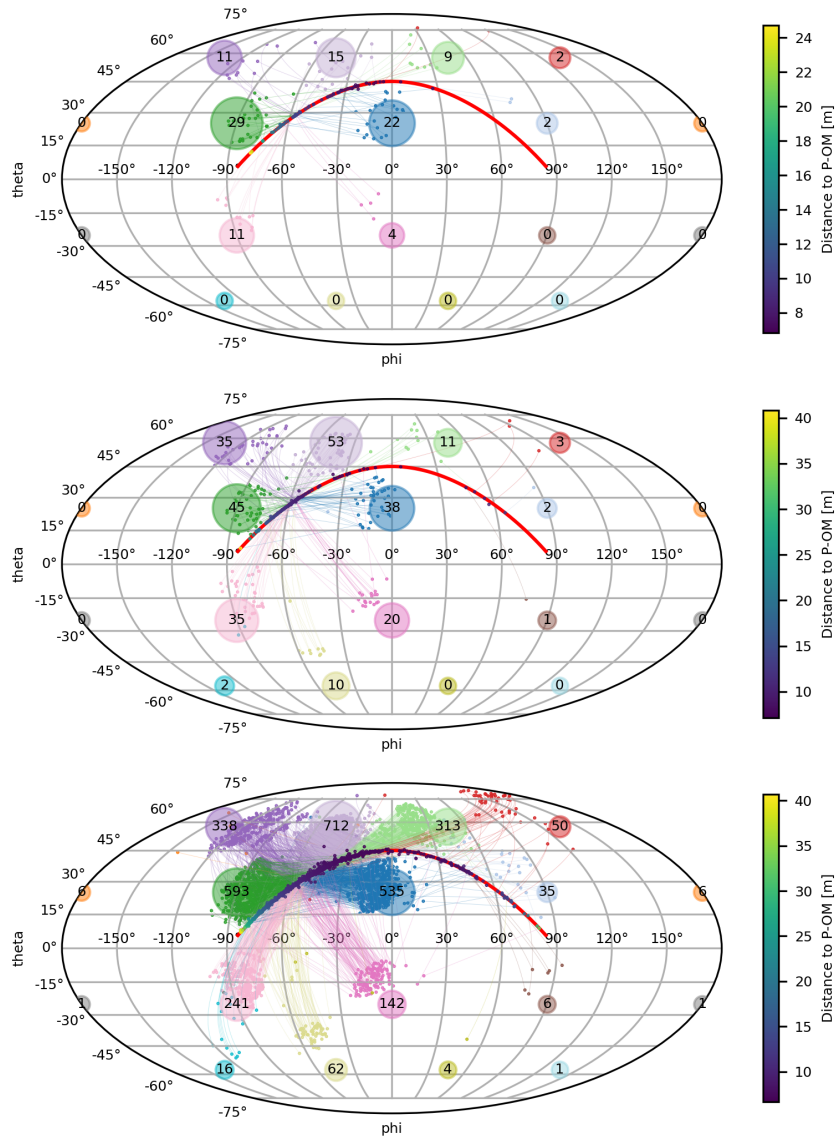


Figure A.4: Simulated signal in the P-OM accumulated from ten muon events. Muons are traveling from $(x, y, z) = (5, -50, 5)$ along the cable of the detector line in positive y . Multiple energies were simulated: 1 TeV (top), 10 TeV (middle) and 100 TeV (bottom). For more details on this plot refer to chapter 6.5.

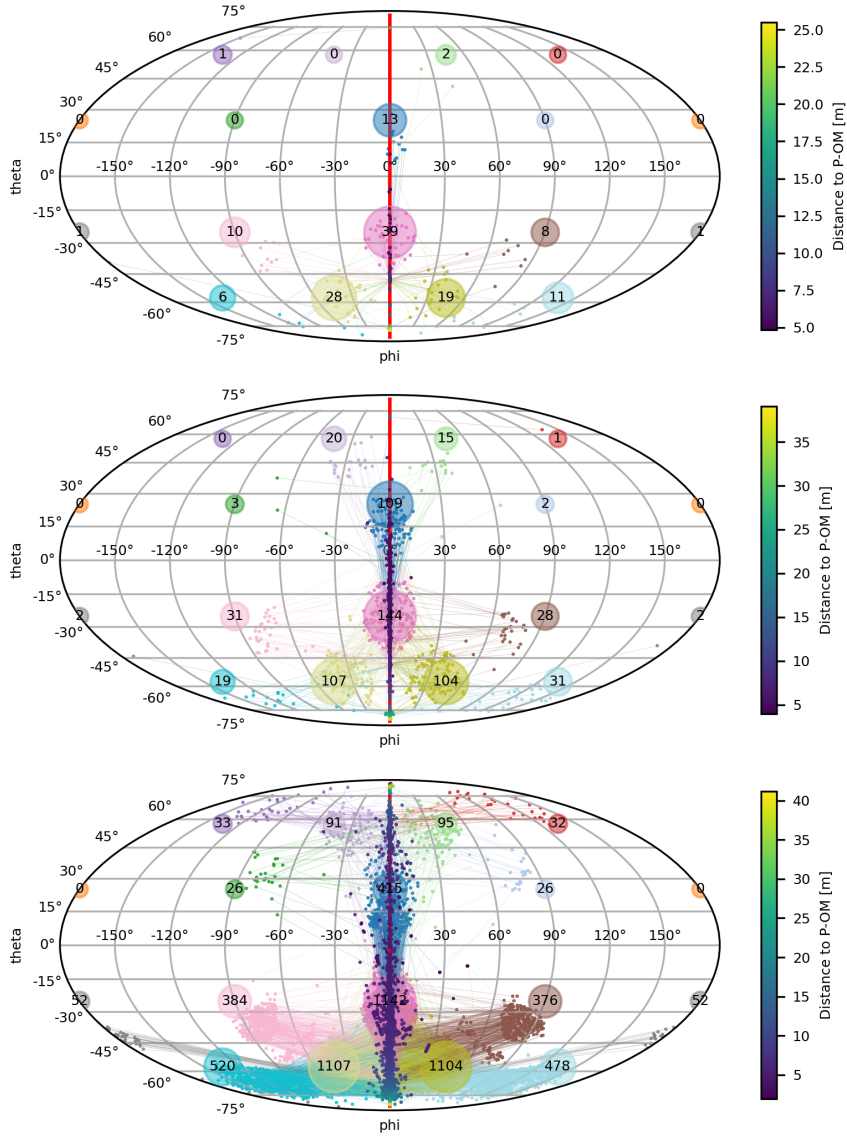


Figure A.5: Simulated signal in the P-OM accumulated from ten muon events. Muons are traveling from $(x, y, z) = (5, 0, -50)$ from the field of view of one hemisphere to the other in positive z . Multiple energies were simulated: 1 TeV (top), 10 TeV (middle) and 100 TeV (bottom). For more details on this plot refer to chapter 6.5.

Appendix B

Source Code

The OMCUs control software is hosted in a Github repository in the P-ONE space:

https://github.com/pone-software/munich_pmt_calibration_system/

It is hosted under a GPL-3.0 license. As the P-ONE space on Github is private, it can only be accessed by members of the P-ONE collaboration.

In the same Github space, the P-OM Geant4 framework is hosted with a GPL-3.0 license, as part of the larger Geant4 repository:

<https://github.com/pone-software/Geant4-Simulations>

The used GDML converter GUIMesh can be found in its forked and updated version publicly available at:

<https://github.com/nretza/GUIMesh>

with the original version hosted at:

<https://github.com/MPintoSpace/GUIMesh>

Bibliography

- [1] Albrecht Karle et al. »IceCube – the next generation neutrino telescope at the South Pole«. In: *Nuclear Physics B-Proceedings Supplements* 118 (2003), pp. 388–395.
- [2] Ulrich F Katz. »KM3NeT: Towards a km³ Mediterranean neutrino telescope«. In: *Nuclear Instruments and Methods in Physics Research Section A: Accelerators, Spectrometers, Detectors and Associated Equipment* 567.2 (2006), pp. 457–461.
- [3] VA Allakhverdyan et al. »Status of the Baikal-GVD Neutrino Telescope and Main Results«. In: *Bulletin of the Russian Academy of Sciences: Physics* (2023), pp. 1–4.
- [4] IceCube Collaboration et al. »Neutrino emission from the direction of the blazar TXS 0506+056 prior to the IceCube-170922A alert«. In: *Science* 361.6398 (2018), pp. 147–151.
- [5] IceCube Collaboration et al. »Evidence for neutrino emission from the nearby active galaxy NGC 1068«. In: *Science* 378.6619 (2022), pp. 538–543.
- [6] IceCube Collaboration et al. »Observation of high-energy neutrinos from the Galactic plane«. In: *Science* 380.6652 (2023), pp. 1338–1343.
- [7] Matteo Agostini et al. »The Pacific Ocean Neutrino Experiment«. In: *Nature Astronomy* 4.10 (2020), pp. 913–915.
- [8] Lisa Schumacher et al. »PLE ν M: A global and distributed monitoring system of high-energy astrophysical neutrinos«. In: *PoS ICRC2021* (2021), p. 1185.
- [9] Antony Hewish et al. »Observation of a rapidly pulsating radio source«. In: *A Source Book in Astronomy and Astrophysics, 1900–1975*. Harvard University Press, 1979, pp. 498–504.
- [10] Kazunori Akiyama et al. »First M87 event horizon telescope results. IV. Imaging the central supermassive black hole«. In: *The Astrophysical Journal Letters* 875.1 (2019), p. L4.
- [11] Grzegorz Madejski and Marek Sikora. »Gamma-ray observations of active galactic nuclei«. In: *Annual Review of Astronomy and Astrophysics* 54 (2016), pp. 725–760.

- [12] Andrii Neronov. »Introduction to multi-messenger astronomy«. In: *Journal of Physics: Conference Series* 1263.1 (June 2019).
- [13] Alessandro De Angelis and Mário Pimenta. *Introduction to particle and astroparticle physics: multimessenger astronomy and its particle physics foundations*. Springer, 2018.
- [14] Victor Franz Hess. »Über Beobachtungen der durchdringenden Strahlung bei sieben Freiballonfahrten«. In: *Z. Phys.* 13 (1912), p. 1084.
- [15] Thomas K Gaisser, Ralph Engel and Elisa Resconi. *Cosmic rays and particle physics*. Cambridge University Press, 2016.
- [16] Antoine Letessier-Selvon and Pierre Auger Collaboration. »Highlights from the Pierre Auger Observatory«. In: *Brazilian Journal of Physics* 44 (2014), pp. 560–570.
- [17] Alexander Aab et al. »The pierre auger observatory upgrade-preliminary design report«. In: *arXiv preprint arXiv:1604.03637* (2016).
- [18] Andrei Kounine. »The alpha magnetic spectrometer on the international space station«. In: *International Journal of Modern Physics E* 21.08 (2012), p. 1230005.
- [19] Pasquale Blasi. »The origin of galactic cosmic rays«. In: *The Astronomy and Astrophysics Review* 21 (2013), pp. 1–73.
- [20] Kenneth Greisen. »End to the cosmic-ray spectrum?«. In: *Physical Review Letters* 16.17 (1966), p. 748.
- [21] Georgi T Zatsepin and Vadim A Kuzmin. »Upper limit of the spectrum of cosmic rays«. In: *Soviet Journal of Experimental and Theoretical Physics Letters* 4 (1966), p. 78.
- [22] Marijke Haverkorn. »Magnetic fields in the Milky Way«. In: *Magnetic fields in diffuse media*. Springer, 2014, pp. 483–506.
- [23] Joss Bland-Hawthorn and Ortwin Gerhard. »The galaxy in context: structural, kinematic, and integrated properties«. In: *Annual Review of Astronomy and Astrophysics* 54 (2016), pp. 529–596.
- [24] Tonia M Venters et al. »Energetic particles of cosmic accelerators I: galactic accelerators«. In: *arXiv preprint arXiv:1903.04634* (2019).
- [25] D Harari, S Mollerach and E Roulet. »On the ultrahigh energy cosmic ray horizon«. In: *Journal of Cosmology and Astroparticle Physics* 2006.11 (Nov. 2006), p. 012.
- [26] J Ballet et al. »Fermi Large Area Telescope Fourth Source Catalog Data Release 4 (4FGL-DR4)«. In: *arXiv preprint arXiv:2307.12546* (2023).

- [27] David A Smith et al. »The Third Fermi Large Area Telescope Catalog of Gamma-ray Pulsars«. In: *arXiv preprint arXiv:2307.11132* (2023).
- [28] Bannanje Sripathi Acharya et al. »Science with the cherenkov telescope array«. In: *arXiv: 1709.07997* (2017).
- [29] Robert J. Gould and Gerald Schröder. »Opacity of the Universe to High-Energy Photons«. In: *Phys. Rev. Lett.* 16 (6 Feb. 1966), pp. 252–254.
- [30] Alessandra Buonanno and BS Sathyaprakash. »Sources of gravitational waves: theory and observations«. In: *arXiv preprint arXiv:1410.7832* (2014).
- [31] Benjamin P Abbott et al. »Observation of gravitational waves from a binary black hole merger«. In: *Physical review letters* 116.6 (2016), p. 061102.
- [32] Fet al Acernese et al. »Advanced Virgo: a second-generation interferometric gravitational wave detector«. In: *Classical and Quantum Gravity* 32.2 (2014), p. 024001.
- [33] »KAGRA: 2.5 generation interferometric gravitational wave detector«. In: *Nature Astronomy* 3.1 (2019), pp. 35–40.
- [34] Felix Henningsen. *Optical Characterization of the Deep Pacific Ocean: Development of an Optical Sensor Array for a Future Neutrino Telescope*. Master’s Thesis. July 2018.
- [35] Felix Henningsen. »The self-monitoring precision calibration light source for the IceCube Upgrade«. PhD Thesis. TUM, Oct. 2021.
- [36] Matthias Huber. »Multi-Messenger correlation study of Fermi-LAT blazars and high-energy neutrinos observed in IceCube«. PhD Thesis. TUM, July 2020.
- [37] Kai Krings. »Search for Galactic and Extra-Galactic Neutrino Emission with IceCube«. PhD Thesis. TUM, Mar. 2018.
- [38] Steven Weinberg. *Cosmology*. OUP Oxford, 2008.
- [39] DJ Fixsen. »The temperature of the cosmic microwave background«. In: *The Astrophysical Journal* 707.2 (2009), p. 916.
- [40] E Baracchini et al. »PTOLEMY: A proposal for thermal relic detection of massive neutrinos and directional detection of MeV dark matter«. In: *arXiv preprint arXiv:1808.01892* (2018).
- [41] Anatoli Fedynitch et al. »Calculation of conventional and prompt lepton fluxes at very high energy«. In: *EPJ Web of Conferences*. Vol. 99. EDP Sciences. 2015, p. 08001.
- [42] John N Bahcall. »Solar neutrinos«. In: *Solar Neutrinos*. CRC Press, 2018, pp. 23–26.

- [43] WC Haxton. »The solar neutrino problem«. In: *Annual Review of Astronomy and Astrophysics* 33.1 (1995), pp. 459–503.
- [44] Ziro Maki, Masami Nakagawa and Shoichi Sakata. »Remarks on the unified model of elementary particles«. In: *Progress of Theoretical Physics* 28.5 (1962), pp. 870–880.
- [45] Sebastian AR Ellis, Kevin J Kelly and Shirley Weishi Li. »Current and future neutrino oscillation constraints on leptonic unitarity«. In: *Journal of High Energy Physics* 2020.12 (2020), pp. 1–61.
- [46] S Fukuda et al. »The super-kamiokande detector«. In: *Nuclear Instruments and Methods in Physics Research Section A: Accelerators, Spectrometers, Detectors and Associated Equipment* 501.2-3 (2003), pp. 418–462.
- [47] F Suekane, KamLAND Collaboration et al. »KamLAND«. In: *Progress in Particle and Nuclear Physics* 57.1 (2006), pp. 106–126.
- [48] John F Beacom. »The diffuse supernova neutrino background«. In: *Annual Review of Nuclear and Particle Science* 60 (2010), pp. 439–462.
- [49] Tamar Kashti and Eli Waxman. »Astrophysical neutrinos: Flavor ratios depend on energy«. In: *Physical Review Letters* 95.18 (2005), p. 181101.
- [50] Christian Haack, Christopher Wiebusch, IceCube Collaboration et al. »A measurement of the diffuse astrophysical muon neutrino flux using eight years of IceCube data.« In: *35th International Cosmic Ray Conference*. Vol. 301. Sissa Medialab. 2018, p. 1005.
- [51] Roberto Aloisio et al. »Cosmogenic neutrinos and ultra-high energy cosmic ray models«. In: *Journal of Cosmology and Astroparticle Physics* 2015.10 (2015), p. 006.
- [52] Silvia Bravo. *Neutrinos and gamma rays, a partnership to explore the extreme universe*. URL: <https://icecube.wisc.edu/news/research/2016/10/neutrinos-and-gamma-rays-partnership-to-explore-extreme-universe/> (visited on 03/08/2023).
- [53] W David Arnett et al. »Supernova 1987A«. In: *Annual review of Astronomy and Astrophysics* 27.1 (1989), pp. 629–700.
- [54] GBM Fermi et al. »Multi-messenger observations of a binary neutron star merger«. In: *Astrophysical Journal Letters* 848.2 (2017), p. L12.
- [55] Mark G Aartsen et al. »The IceCube Neutrino Observatory: instrumentation and online systems«. In: *Journal of Instrumentation* 12.03 (2017), P03012.

- [56] Annarita Margiotta, KM3NeT Collaboration et al. »The KM3NeT deep-sea neutrino telescope«. In: *Nuclear Instruments and Methods in Physics Research Section A: Accelerators, Spectrometers, Detectors and Associated Equipment* 766 (2014), pp. 83–87.
- [57] Yury Malyshkin, Baikal-GVD collaboration et al. »Baikal-GVD neutrino telescope: Design reference 2022«. In: *Nuclear Instruments and Methods in Physics Research Section A: Accelerators, Spectrometers, Detectors and Associated Equipment* 1050 (2023), p. 168117.
- [58] Raj Gandhi et al. »Ultra-high-energy neutrino interactions«. In: *Astroparticle Physics* 5.2 (1996), pp. 81–110.
- [59] PA Cerenkov et al. »Visible emission of clean liquids by action of γ radiation«. In: *Dokl. Akad. Nauk SSSR* 2 (1934), pp. 451–454.
- [60] IE Tamm and IM Frank. »Coherent radiation of fast electrons in a medium«. In: *Dokl. Akad. Nauk SSSR*. Vol. 14. 3. 1937, pp. 107–112.
- [61] UF Katz. »Cherenkov light imaging in astroparticle physics«. In: *Nuclear Instruments and Methods in Physics Research Section A: Accelerators, Spectrometers, Detectors and Associated Equipment* 952 (2020), p. 161654.
- [62] Hamamatsu Photonics K. K. *R14374/R14689 Photomultiplier Datasheet*. Online PDF. URL: https://www.hamamatsu.com/content/dam/hamamatsu-photonics/sites/documents/99_SALES_LIBRARY/etd/R14374_R14689_TPMH1381E.pdf (visited on 20/06/2023).
- [63] Christian Spiering. »Neutrino detectors under water and ice«. In: *Particle Physics Reference Library: Volume 2: Detectors for Particles and Radiation* (2020), pp. 785–822.
- [64] IceCube Collaboration. *Detecting Neutrinos / IceCube Masterclass*. URL: <https://masterclass.icecube.wisc.edu/de/node/213> (visited on 06/08/2023).
- [65] L Pasquali and MH Reno. »Tau neutrino fluxes from atmospheric charm«. In: *Physical Review D* 59.9 (1999), p. 093003.
- [66] Nicolai Bailly et al. »Two-year optical site characterization for the Pacific Ocean Neutrino Experiment (P-ONE) in the Cascadia Basin«. In: *The European Physical Journal C* 81.12 (2021), p. 1071.
- [67] E Andres et al. »The AMANDA neutrino telescope: principle of operation and first results«. In: *Astroparticle Physics* 13.1 (2000), pp. 1–20.
- [68] Elisa Resconi, IceCube Collaboration et al. »Status and prospects of the IceCube neutrino telescope«. In: *Nuclear Instruments and Methods in Physics Research Section A: Accelerators, Spectrometers, Detectors and Associated Equipment* 602.1 (2009), pp. 7–13.

- [69] MG Aartsen et al. »Measurement of South Pole ice transparency with the IceCube LED calibration system«. In: *Nuclear Instruments and Methods in Physics Research Section A: Accelerators, Spectrometers, Detectors and Associated Equipment* 711 (2013), pp. 73–89.
- [70] Martin Rongen. »Calibration of the IceCube neutrino observatory«. In: *arXiv preprint arXiv:1911.02016* (2019).
- [71] Markus Ackermann et al. »Optical properties of deep glacial ice at the South Pole«. In: *Journal of Geophysical Research: Atmospheres* 111.D13 (2006).
- [72] Rasha Abbasi et al. »The design and performance of IceCube DeepCore«. In: *Astroparticle physics* 35.10 (2012), pp. 615–624.
- [73] Rasha Abbasi et al. »IceTop: The surface component of IceCube«. In: *Nuclear Instruments and Methods in Physics Research Section A: Accelerators, Spectrometers, Detectors and Associated Equipment* 700 (2013), pp. 188–220.
- [74] Aya Ishihara. »The IceCube Upgrade – Design and Science Goals«. In: *arXiv preprint arXiv:1908.09441* (2019).
- [75] Rasha Abbasi et al. »Design and performance of the multi-PMT optical module for IceCube Upgrade«. In: *PoS ICRC2021* (2021), p. 1070.
- [76] Petros A Rapidis, NESTOR collaboration et al. »The NESTOR underwater neutrino telescope project«. In: *Nuclear Instruments and Methods in Physics Research Section A: Accelerators, Spectrometers, Detectors and Associated Equipment* 602.1 (2009), pp. 54–57.
- [77] Emilio Migneco et al. »Status of NEMO«. In: *Nuclear Instruments and Methods in Physics Research Section A: Accelerators, Spectrometers, Detectors and Associated Equipment* 567.2 (2006), pp. 444–451.
- [78] Michel Ageron et al. »ANTARES: the first undersea neutrino telescope«. In: *Nuclear Instruments and Methods in Physics Research Section A: Accelerators, Spectrometers, Detectors and Associated Equipment* 656.1 (2011), pp. 11–38.
- [79] Sebastiano Aiello et al. »The KM3NeT multi-PMT optical module«. In: *Journal of Instrumentation* 17.07 (2022), P07038.
- [80] Annarita Margiotta. »The KM3NeT infrastructure: status and first results«. In: *arXiv preprint arXiv:2208.07370* (2022).
- [81] Km3Net Collaboration. *Astroparticle physics with ARCA*. URL: <https://www.km3net.org/research/physics/astronomy-with-arca/> (visited on 12/08/2023).
- [82] Km3Net Collaboration. *Particle physics with ORCA*. URL: <https://www.km3net.org/research/physics/particle-physics-with-orca/> (visited on 12/08/2023).

- [83] Elisa Resconi. »The Pacific Ocean Neutrino Experiment«. In: *Proceedings of 37th International Cosmic Ray Conference PoS(ICRC2021)*. Vol. 395. 2021, p. 024.
- [84] Christopher R Barnes et al. »Final installation and initial operation of the worlds first regional cabled ocean observatory (NEPTUNE Canada)«. In: *Lobseratoire NEPTUNE du Canada* 38.3 (2010).
- [85] M Boehmer et al. »STRAW (STRings for Absorption length in Water): pathfinder for a neutrino telescope in the deep Pacific Ocean«. In: *Journal of Instrumentation* 14.02 (2019), P02013.
- [86] Immacolata Carmen Rea et al. »P-ONE second pathfinder mission: STRAW-b«. In: *Proceedings of 37th International Cosmic Ray Conference PoS(ICRC2021)*. Vol. 395. 2021, p. 1092.
- [87] H Paul Johnson, Susan L Hautala and Tor A Bjorklund. »The thermal environment of Cascadia Basin«. In: *Geochemistry, Geophysics, Geosystems* 13.7 (2012).
- [88] Christian Haack and Lisa Schumacher. »Machine-learning aided detector optimization of the Pacific Ocean Neutrino Experiment«. In: *Proceedings of 38th International Cosmic Ray Conference PoS(ICRC2023)*. Vol. 444. 2023, p. 1059.
- [89] Christian Spannfellner. »Design of the Pacific Ocean Neutrino Experiment's First Detector Line«. In: *Proceedings of 38th International Cosmic Ray Conference PoS(ICRC2023)*. Vol. 444. 2023, p. 1219.
- [90] Michael Bohmer. »Sub-ns timing for the Pacific Ocean Neutrino Experiment by optical fiber using Gigabit Ethernet«. In: *Proceedings of 38th International Cosmic Ray Conference PoS(ICRC2023)*. Vol. 444. 2023, p. 1216.
- [91] Christopher Fink. *Pacific Ocean Neutrino Experiment: Optical Case Studies for the Multi-PMT Module*. Master's Thesis. Feb. 2022.
- [92] Jakub Stacho et al. »Development of Calibration Light Sources for the Pacific Ocean Neutrino Experiment«. In: *Proceedings of 38th International Cosmic Ray Conference PoS(ICRC2023)*. Vol. 444. 2023, p. 1113.
- [93] Dilraj Ghuman, Felix Henningsen and Matthias Danninger. »The Acoustic Calibration System for the Pacific Ocean Neutrino Experiment«. In: *Proceedings of 38th International Cosmic Ray Conference PoS(ICRC2023)*. Vol. 444. 2023, p. 1112.
- [94] Nikhita Khera and Felix Henningsen. »POCAM in the IceCube Upgrade«. In: *arXiv preprint arXiv:2108.05298* (2021).

- [95] Anthony G Wright. *The photomultiplier handbook*. Oxford University Press, 2017.
- [96] Hamamatsu Photonics K. K. *Photomultiplier Tubes - Basics and Applications*. Online PDF. fourth edition. URL: https://www.hamamatsu.com/content/dam/hamamatsu-photonics/sites/documents/99_SALES_LIBRARY/etd/PMT_handbook_v4E.pdf (visited on 10/07/2023).
- [97] Laura Winter. *The Pacific Ocean Neutrino Experiment: Photosensor Research and Qualification Setup Development*. Master's Thesis. Feb. 2022.
- [98] Lasse Halve and Johannes Werthebach. »Design of an Efficient, High-Throughput Photomultiplier Tube Testing Facility for the IceCube Upgrade«. In: *arXiv preprint arXiv:2107.09954* (2021).
- [99] Store Arduino Arduino. »Arduino«. In: *Arduino LLC 372* (2015).
- [100] Mike Folk et al. »An overview of the HDF5 technology suite and its applications«. In: *Proceedings of the EDBT/ICDT 2011 workshop on array databases*. 2011, pp. 36–47.
- [101] S. Agostinelli et al. »Geant4 a simulation toolkit«. In: *Nuclear Instruments and Methods in Physics Research Section A: Accelerators, Spectrometers, Detectors and Associated Equipment* 506.3 (2003), pp. 250–303.
- [102] J. Allison et al. »Recent developments in Geant4«. In: *Nuclear Instruments and Methods in Physics Research Section A: Accelerators, Spectrometers, Detectors and Associated Equipment* 835 (2016), pp. 186–225.
- [103] Geant Collaboration. *Geant4 Material Database*. URL: <https://geant4-userdoc.web.cern.ch/UsersGuides/ForApplicationDeveloper/html/Appendix/materialNames.html> (visited on 20/06/2023).
- [104] Geant Collaboration. *Guide for Physics Lists*. URL: <https://geant4-userdoc.web.cern.ch/UsersGuides/PhysicsListGuide/html/index.html> (visited on 20/06/2023).
- [105] R. Chytrcek et al. »Geometry Description Markup Language for Physics Simulation and Analysis Applications«. In: *IEEE Transactions on Nuclear Science* 53.5 (2006), pp. 2892–2896.
- [106] Carl Vuosalo et al. »A tool to convert CAD models for importation into Geant4«. In: *Journal of Physics: Conference Series*. Vol. 898. 4. IOP Publishing. 2017, p. 042024.
- [107] M. Pinto and P. Gonçalves. »GUIMesh: A tool to import STEP geometries into Geant4 via GDML«. In: *Computer Physics Communications* 239 (2019), pp. 150–156.

- [108] Pierre Pourrouquet et al. »FASTRAD 3.2: Radiation shielding tool with a new Monte Carlo module«. In: *2011 IEEE Radiation Effects Data Workshop*. IEEE. 2011, pp. 1–5.
- [109] Ali Behcet Alpat et al. »MRADSIM-Converter: A new software for STEP to GDML conversion«. In: *Computer Physics Communications* 286 (2023), p. 108688.
- [110] Juergen Riegel, Werner Mayer and Yorik van Havre. *FreeCAD*. 2016.
- [111] EM Stanley. »The Refractive Index of Pure Water and Seawater as a Function of High Pressure and Moderate Temperature, Part II – Pure Water for a Wavelength of 6328 Angstroms«. In: *Deep-Sea Res* 14 (1970), pp. 427–439.
- [112] Nautilus Marine Service GmbH. *VITROVEX instrumentation housings*. Online PDF. URL: https://www.vitrovex.com/wp-content/uploads/2020/09/DB_instrumenthousing_092020.pdf (visited on 20/06/2023).
- [113] Inc SCHOTT North America. *DURAN: Tubing, Rods and Capillaries made of Borosilicate Glass*. Online PDF. URL: <https://media.schott.com/api/public/content/4b6b4e5d10744d29ac632bbd63dee5d8?v=dc5a91ee> (visited on 20/06/2023).
- [114] Wacker Chemie AG. *WACKER SilGel 612 A/B Datasheet*. Online PDF. URL: <https://www.wacker.com/h/de-de/medias/WACKER-SilGel-612-AB-en-2022.06.28.pdf> (visited on 20/06/2023).
- [115] Geant Collaboration. *Physics Reference Manual*. URL: <https://geant4-userdoc.web.cern.ch/UsersGuides/PhysicsReferenceManual/html/index.html> (visited on 20/06/2023).
- [116] Geant Collaboration. *Book For Application Developers*. URL: <https://geant4-userdoc.web.cern.ch/UsersGuides/ForApplicationDeveloper/html/index.html> (visited on 20/06/2023).
- [117] Geant Collaboration. *Users Guide for Toolkit Developers*. URL: <https://geant4-userdoc.web.cern.ch/UsersGuides/ForToolkitDeveloper/html/index.html> (visited on 20/06/2023).
- [118] Wacker Chemie AG. *WACKER ELASTOSIL RT 601 A/B Datasheet*. Online PDF. URL: <https://www.wacker.com/h/de-de/medias/ELASTOSIL-RT-601-AB-en-2022.06.28.pdf> (visited on 20/08/2023).
- [119] Lea Ginzkey. *Optical Module Design and Time Synchronization for the Pacific Ocean Neutrino Experiment*. Bachelor’s Thesis. June 2023.